To the Graduate Council:

I am submitting herewith a dissertation written by Alexander Brassington entitled "Quantum Magnetism in the Shastry Sutherland Lattice Family $R_2Be_2SiO_7$." I have examined the final paper copy of this dissertation for form and content and recommend that it be accepted in partial fulfillment of the requirements for the degree of Doctor of Philosophy, with a major in Physics.

Haidong Zhou, Major Professor

We have read this dissertation
and recommend its acceptance:

Jian Liu

Dustin Gilbert

Ruixing Zhang

Accepted for the Council:

Dixie L. Thompson

Vice Provost and Dean of the Graduate School

To the Graduate Council:
I am submitting herewith a dissertation written by Alexander Brassington entitled "Quantum Magnetism in the Shastry Sutherland Lattice Family $R_2Be_2SiO_7$." I have examined the final electronic copy of this dissertation for form and content and recommend that it be accepted in partial fulfillment of the requirements for the degree of Doctor of Philosophy, with a major in Physics.

Haidong Zhou, Major Professor

We have read this dissertation
and recommend its acceptance:

Jian Liu

Dustin Gilbert

Ruixing Zhang

Accepted for the Council:

Dixie L. Thompson

Vice Provost and Dean of the Graduate School

(Original signatures are on file with official student records.)

Quantum Magnetism in the Shastry Sutherland Lattice Family $\mathbf{R_2Be_2SiO_7}$

A Dissertation Presented for the

Doctor of Philosophy

Degree

The University of Tennessee, Knoxville

Alexander Brassington

August 2025

Acknowledgements

First and foremost I would like to thank my supervisor Haidong Zhou for his guidance, support, and patience throughout my project. My thanks also go out to Qing Huang for help and supervision with crystal growth. Chengkun Xing and all my fellow PhD students in the quantum magnetism group for providng interesting conversations and making my time at the University of Tennessee enjoyable.

I would like to thank all the instruments scientists at ORNL, Gabriele Sala, Stuart Calder, Kyle Ma, Alexander Kolesnikov, Keith Taddei, Yan Wu, Danielle Yahne, Joe Paddison, Matthias Frontzek, and Benjamin Frandsen for help throughout the experiments, their interesting discussion about this work, and their patience with analysis questions. I would also like to thank Eun Sang Choi of the NHMFL in Florida for his assistance during experiments and with preparing samples. My particular and heartfelt thanks to Adam Aczel for his guidance and detailed discussions on this work.

Dedications

Parts of this dissertation are quoted from work during my Ph.D. program published in the last few years. The related chapter and publication information is listed below:

Chapter 1: Introduction:

Synthesis and magnetic properties of the Shastry-Sutherland family $R_2Be_2SiO_7$ (R = Nd, Sm, Gd-Yb)

A. Brassington, Q. Huang, A. A. Aczel, and H. D. Zhou

PHYSICAL REVIEW MATERIALS 8, 014005 (2024)

Chapter 3: Magnetic Properties of $Er_2Be_2SiO_7$:

Magnetic properties of the quasi-XY Shastry-Sutherland magnet $Er_2Be_2SiO_7$

A. Brassington, Q. Ma, G. Sala, A. I. Kolesnikov, K. M. Taddei, Y. Wu, E. S.Choi, H. Wang, W. Xie, J. Ma, H. D. Zhou, and A. A. Aczel

PHYSICAL REVIEW MATERIALS 8, 094001 (2024)

Chapter 5: Magnetic Properties of $Yb_2Be_2SiO_7$

Novel entangled dimer state in the Shastry-Sutherland magnet $Yb_2Be_2SiO_7$

A. Brassington, Q. Ma, G. Duan, S. Calder, A.I. Kolesnikov, K.M. Taddei, G. Sala, H. Wang, W. Xie, B.A. Frandsen, N. Li, X.F. Sun, C. Liu, R. Yu, H.D. Zhou, and A.A. Aczel

Submitted to Nature Communications

Abstract

Geometrically frustrated magnetism arises when competing exchange interactions are incompatible with the geometrical arrangement of magnetic ions in the lattice. This leads to a large ground state degeneracy and the system typically has difficulty establishing a unique ground state often resulting in unusual magnetic ground states characterized by quantum entanglement and complex field dependent phase diagrams. The rare earth compound family $R_2Be_2SiO_7$ garnered our attention when we realized that the R^{3+} ions formed a structure equivalent to the geometrically frustrated Shastry-Sutherland lattice. The competing interactions and unique geometry of this lattice produces interesting magnetic phases both in zero field, in the form of unique ground states lacking long range order, and in field, where an out of plane field induces magnetization plateau in several members.

An investigation into three members of the $R_2Be_2SiO_7$ family, $Er_2Be_2SiO_7$, $Dy_2Be_2SiO_7$, and $Yb_2Be_2SiO_7$ is presented in this thesis. Both $Er_2Be_2SiO_7$ and $Dy_2Be_2SiO_7$ compounds order into non-collinear antiferromagnetic states at 0.85 K and 1.1 K respectively. While $Yb_2Be_2SiO_7$ shows no signs of long range order and instead appears to realize a unique entangled dimer ground state. For $Er_2Be_2SiO_7$ field applied perpendicular to the plane produces two successive magnetic transitions but nor magnetization plateau. The behavior of $Er_2Be_2SiO_7$ is broadly consistent with classical anisotropic moments. In $Dy_2Be_2SiO_7$ a field applied perpendicular to the plane produces several magnetization plateau at: 1/7,4/9, and 2/3 fractions of

the saturation magnetization. Both $Er_2Be_2SiO_7$ and $Dy_2Be_2SiO_7$ have different zero-field spin structures with the same magnetic propagation vector of (0,0,1/2) and with moments primarily oriented in the ab-plane. The spin structure of the plateau phases in $Dy_2Be_2SiO_7$ remains to be determined.

For all three compounds inelastic neutron scattering experiments were done to gain insight into the CEF spectrum of the compound. The ground state doublet is found to be well isolated in $Dy_2Be_2SiO_7$ and $Yb_2Be_2SiO_7$ with the first excited level at 7.9 meV and 11 meV respectively. For $Er_2Be_2SiO_7$ the first excited level is at only 1.7 meV indicating an $S_{eff} = 1/2$ model is not appropriate. In $Yb_2Be_2SiO_7$ inelastic measurements with cold neutrons reveal several excitations related to gaps in the spin excitation spectrum at energy transfers of 0.11 meV and 0.19 meV. Subsequent analysis determines that these gaps are due to excitations from the novel entangled dimer unit ground state: $(\uparrow\uparrow - \downarrow\downarrow)/\sqrt{2}$.

Table of Contents

Chapter 1

Introduction

The first discovery of magnetism and magnetic materials is attributed to the Greeks who in ∼600 BC recorded the properties of magnetite (Fe_2O_3). In the 21^{st} century using the framework of quantum mechanics we identify the magnetism in magnetite as ferromagnetism, a phenomenon in which unpaired electrons in the material co-operatively align in one directions resulting in a macroscopic magnetic moment. The next great leap in our understanding of magnetism coincides with the experimental detection of anti-ferromagnetism via neutron diffraction [1], where magnetic moments in a crystal form a bipartite lattice whose net magnetization approaches zero. In modern research on magnetism the large variety of systems of interest and reported types of magnetic interactions produce a similarly large array of phenomenon.

One such phenomenon of interest is magnetic frustration where in the spins are unable to orient themselves in a way that satisfies competing magnetic interactions. This frustration often results in the suppression of more typical long range magnetic order and allows for the formation of several novel phenomenon. A common way to induce magnetic frustration is geometric frustration where the spatial arrangement of spins produces competing interactions [2, 3, 4]. The simplest example of geometrical frustration can be seen in a triangular lattice with Ising spins. Spins are coupled

antiferromagnetically along one axis and there is no arrangement which can satisfy the interactions among the three spins.

Beyond the simple case of a triangular lattices many other lattices can result in geometric frustration such as triangular, kagome, and pyrochlore. One such lattice capable of inducing geometrical frustration is the Shastry-Sutherland lattice (SSL). The SSL consists of planes of orthogonal dimers such that each magnetic ion has one nearest neighbor and four next-nearest neighbors. The SSL model has attracted significant interest as simple model which is exactly solvable [5]. For certain parameters the SSL has long been predicted to host an entangled ground state consisting of dimer units. This prediction would later be confirmed by the synthesis and investigation of the first SSL compound $SrCu_2(BO_3)_2$, wherein the Cu ions arrange themselves in a SSL.

We have synthesized a new family of rare earth based Shastry-Sutherland magnets with the formula $R_2Be_2SiO_7$ (R = Nd, Sm, and Gd-Yb) [6]. A brief analysis of the atomic structure of the entire series is presented in the introduction, all members are iso-structural. This thesis is organized as follows. A brief introduction to geometrically frustration, the SSL,and structural characterization of the $R_2Be_2SiO_7$ system is given. An overview of the experimental techniques utilized is given in chapter 2. While the magnetic properties of $Er_2Be_2SiO_7$, $Dy_2Be_2SiO_7$, and $Yb_2Be_2SiO_7$ are presented in detail in chapters 3,4, and 5 respectively. The main results on the above three $R_2Be_2SiO_7$ (R = Er, Dy, Yb) compounds are summarized in chapter 6 alongside suggestions for future work.

1.1 Introduction to Frustrated Magnetism

In physics, frustration refers to the presence of competing forces that can not be simultaneously satisfied. In frustrated magnetism this refers to magnetic moments or spins and the exchange interaction forces that influence their orientation. Although frustration in magnetic systems can arise for multiple reasons, e.g site disorder, it

mostly common refers to geometric frustration where the arrangement of ions in a periodic crystal induce exchange interactions with contributions to the energy that cannot be simultaneously minimized by any arrangement of the magnetic moments. A simple example of this frustration can be seen by considering Ising moments restricted to the vertical axis with antiferromagnetic coupling between spins arranged in a triangular lattice, Fig 1.1. Although two of the three spins can be aligned antiparallel with each other satisfying the coupling constraint there is no orientation of the third spin that can simultaneously satisfy the coupling interaction with the other two.

Typically geometrically frustrated lattices are based either on corner or edge sharing triangles or tetrahedra. Examples of frustrated lattices include the 2D triangular [7], 2D kagome [8], and 3D pyrochlore [9, 3] lattices which are shown in Fig 1.2. The 2D triangular and kagome lattices both contain frustrating triangles while the 3D pyrochlore lattice is an example of frustrated Tetrahedra. Geometrical frustration in magnetic crystals has attracted intense interest as a pathway to avoid conventional Neel order and stabilize more exotic phases including resonating valence bond crystals [10, 11, 12, 13], spin ices [14, 15, 16, 17], and quantum spin liquid phases [18, 19, 20, 21, 22, 23, 24, 25, 26].

1.2 The Shastry-Sutherland Lattice

The Shastry Sutherland lattice (SSL) can be described as a square lattice of orthogonal dimers where each ion has a single nearest or intra-dimer neighbor and four next-nearest or inter-dimer neighbors as depecited in Fig 1.3[5]. The Hamiltonian for the system including the Zeeman interaction with a magnetic field $\vec{B}$ can be written as [27]:

$$\mathcal{H} = \sum_{nn} S_i J_1 S_j + \sum_{nnn} S_i J_2 S_j - \vec{B} \sum_i S_i \tag{1.1}$$

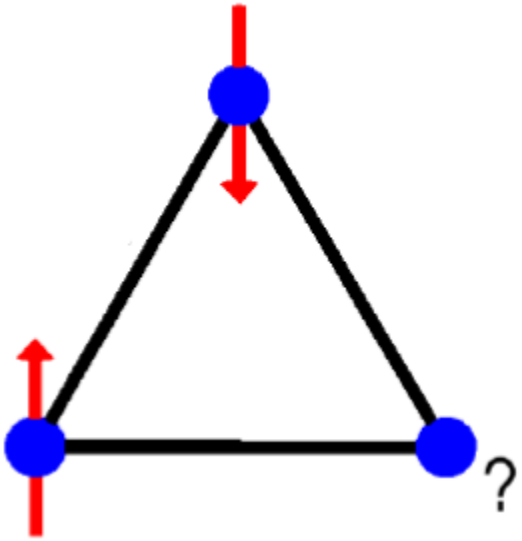

Figure 1.1: The simplest example of geometric frustration can be seen by considering Ising spins arranged in a triangular lattice.

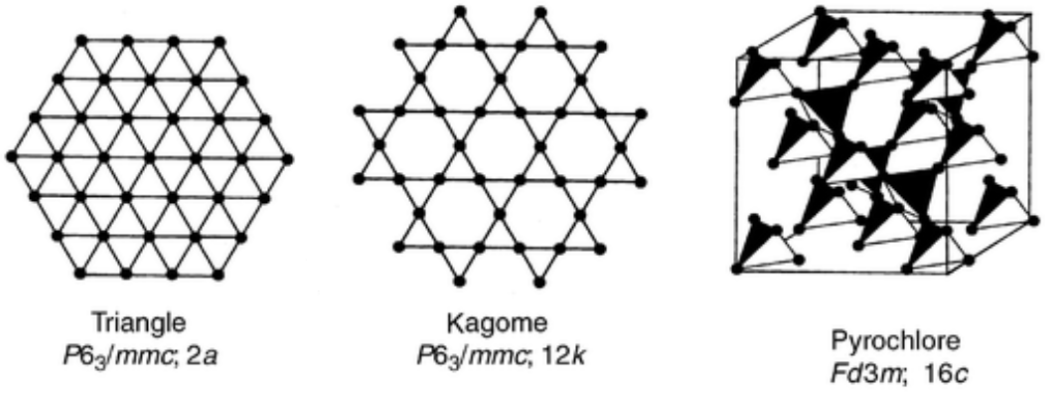

Figure 1.2: Common Frustrated lattices. The triangular and Kagome lattices are example of frustration in 2D while the pyrochlore lattice is an example of frustration in 3D.

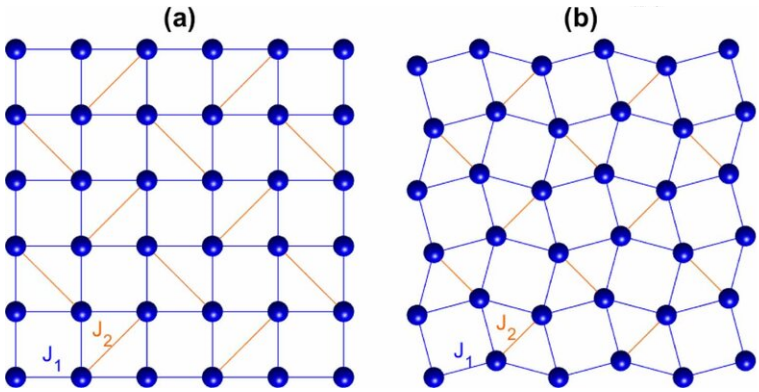

Figure 1.3: (a) The theoretical lattice first considered by Shastry and Sutherland in 1981. It can be described as a square lattice with an additional diagonal bond every other square. (b) The topologically equivalent experimental realization of the SSL in RB_4.

The lattice has been extensively studied for Heisenberg [27, 28, 29], Ising [30, 31, 32], and XXZ [33, 34] cases but limited work has been done on the more general XYZ case. For the maximal quantum case of $S_{eff} = 1/2$ the Heisenberg SSL is known to host a ground state consisting of products of dimer singlets for a sufficiently large value of J_1/J_2 where J_1 and J_2 are the intra and inter dimer coupling strengths respectively [5].

In the case of classical spins ($S \to \infty$) typical Neel Order is favored for the ground state for all values of J_1/J_2 in both Heisenberg [27, 29]and Ising models [32]. Although the predicted ground state is somewhat typical, experimental realizations of classical spins on an SSL also display striking series of magnetization plateau at rational fractions of the saturation magnetization as seen in the RB_4 series.

1.2.1 $SrCu_2(BO_3)_2$

Experimental realizations of the Shastry-Sutherland lattice are rare and of the few known compounds that do form a SSL $SrCu_2(BO_3)_2$ is the most notable [35, 36]. In $SrCu_2(BO_3)_2$ the Cu ions form SSL layers in the ab-plane and layers are AAA-type stacked along the c-axis [37]. The inter-planar bond distance is greater than both intra and inter dimer bond distances and although inter-plane coupling is considered in some models layers are most typically considered isolated resulting in a 2D system like that originally considered by Shastry and Sutherland [5]. In $SrCu_2(BO_3)_2$ the transition metal and spin 1/2 Cu ions have simple Heisenberg anisotropy and the Hamiltonian of the system is of the same form as equation 1.1.

At low temperatures a gap in the excitation spectrum is observed at ~ 3 meV corresponding to an excitation from the singlet dimer state, $\phi = \uparrow\downarrow - \downarrow\uparrow$, to one of the degenerate triplet states [38, 39, 40]. The spectra peak associated with this excitation is nearly dispersion-less indicating that triplet excitations carry very little momentum and their hopping ratio is so small that the excitations can nearly be considered completely bound to the site. Intriguingly it has been shown that $\alpha =$

J_1/J_2 is close to a critical point and is very sensitive to the application of pressure [41, 42, 37, 43]. Under applied pressure at low temperatures the magnetic ground state of the system transitions from a product of dimer singlets to an entangled plaquette phase and finally to an ordered antiferromagnetic state, with possibly other intermediate phases.

In $SrCu_2(BO_3)_2$ several plateaus are observed in the magnetization at rational fractions of the saturation magnetization. These plateaus form the improbable sequence 1/8, 2/15, 1/6, 1/4, 1/3, 2/5, and 1/2. The plateaus are attributed to wigner crystals either of individual triplet excitations embedded in a singlet space or as crystals of bound states each comprising multiple dimer units [41, 39, 44, 45].

1.2.2 RB_4 and other compounds

Beyond $SrCu_2(BO_3)_2$, most SSL compounds contain magnetic rare-earth ions. The RB_4 family represents the only known binary SSL compounds and have been extensively studied [46, 47, 48, 49, 50]. Though all RB_4 compounds order antiferromagnetically, like $SrCu_2(BO_3)_2$ several members of this family have complex magnetic phase diagrams and magnetization plateau at fractional values of the saturation magnetization. A 1/2 magnetization plateau is observed in ErB_4 [46], DyB_4 [50], TbB_4 [51, 52], and TmB_4 [53, 54]. While TbB_4 and TmB_4 also displaying further fractional magnetization plateau at 1/3 and 1/8 respectively. The field induce magnetic phases observed in the RB_4 series range from relatively simple ferri-magnetic structures to phases with expanded unit cells containing stripe structures [52, 55].

For ternary compounds, a large metallic family with the general formula R2T2X and structure type U3Si2 have been identified and synthesized. R2T2X compounds with T (X) = Si (Al, Sc, Mg, Li), Ge (Mg, In, Al, Sn, Cd), Ni (Sn, Mg), Cu (In, Mg, Cd), Pd (In, Pb, Cd, Mg), and Pt (Rh, Pb) have been reported and can be found in the international crystal structure database. Only a small subset of the listed R2T2X compounds have had their magnetic properties investigated, with bulk

characterization evidence for both antiferromagnetic and ferromagnetic ground states available in select cases [56, 57, 58, 59, 60, 61, 62, 63, 64]. The Yb-based systems have the most complex electronic and magnetic properties, with intermediate valence states identified in Yb2Si2Al [62] and Yb2Pd2In [65]and quasi-one-dimensional quantum magnetism arising from weakly coupled spin chains found in Yb2Pt2Pb [64]. There are two known quaternary SSL families based on insulating oxides or sulfides with general formulas BaR_2MX_5 (M = Pd, Zn; X = O, S) [66, 67, 68, 69, 70, 71, 72]and the melilite type $R_2Be_2GeO_7$ [73].

1.3 $R_2Be_2SiO_7$

All members of the $R_2Be_2SiO_7$ family are isostructural and crystallize into the tetragonal space group P-421m (113) with the melilite structure [6]. The R and Be ions occupy two different 4e Wyckoff sites that each generate a SSL topology. The Si ions occupy a 2a Wyckoff site and they are found in the same plane as the Be ions, while the O ligands occupy three different Wyckoff sites (2c, 4e, and 8 f). The oxygen coordination of the R, Si, and Be ions are 8, 4, and 4, respectively. The distorted RO8 polyhedron generates a low-point symmetry of Cs (or m), which needs to be taken into account when considering crystal-field splitting of the R ground-state multiplet. In this structure, the R and BeO4/SiO4 planes are alternatively stacked along the [001]-axis as shown in Fig 1.4. Each BeO4/SiO4 plane is made up of a series of edge-sharing tetrahedra. While this atomic arrangement is reminiscent of the ternary compounds with the U_3Si_2 structure such as Yb_2Pt_2Pb, the addition of the O ions between the R and Be layers ensures that the $R_2Be_2SiO_7$ family is insulating.

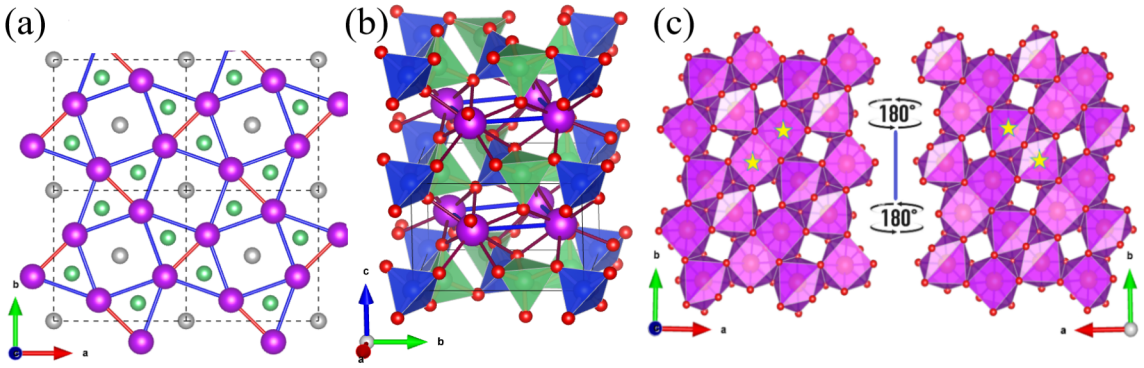

Figure 1.4: (a) Schematic diagram of the R^{3+} ions in purple forming a SSL lattice in the *ab*-plane. Intradimer bonds J_1 are shown in red and interdimer bonds J_2 in blue . The relative positions of the Be and Si ions are also shown in green and gray respectively. (b) Structure of $R_2Be_2SiO_7$ viewed slightly off the [100] axis. The SSL layers formed by the RO_8 polyhedra are separated by layers of BeO_4 and SiO_4 tetrahedra. (c) The monoclinic point symmetry (C_s) of the R ions is best illustrated by viewing the crystal structure along the [001] and [00-1] directions. A single NN pair of R ions is marked with stars for reference. A single plane is shown from both the [001] and [00-1] directions to highlight the two sub-lattices.

Detailed crystal structure refinement results and select distances for select compounds are provided in Table 1.1. Representative XRD patterns for $R_2Be_2SiO_7$ (R = Sm, Yb) with the refinement results superimposed on the data are shown in Fig 1.5 and they agree well with the calculated pattern from a previous single crystal study [74]. The XRD refinement results indicate no significant signs of Be2+/Si4+ site mixing, which is in good agreement with previous work on $R_2Be_2GeO_7$ [73]. Fig 1.6 shows the lattice parameters a (left axis) and c (right axis) versus ionic radius (IR) for all compounds synthesized in the $R_2Be_2SiO_7$ series. The lattice constants increase approximately linearly with increasing R ionic radius. $Yb_2Be_2SiO_7$ has the smallest unit cell with a = 7.223 $\mathring{A}$ and c = 4.719 $\mathring{A}$ while $Nd_2Be_2SiO_7$ has the largest unit cell with a = 7.461 $\mathring{A}$ and c = 4.862 $\mathring{A}$.

The ligand environment around the R ions are irregularly- shaped polyhedra consisting of eight cooridnated oxygen ions, as shown in Fig 1.4 (c). Opposite faces of the polyhedra, located above and below the SSL planes, have distorted square and diamond geometries respectively. Two distinct sub-lattices with the square and diamond faces are visible. The R ions have a monoclinic point group symmetry of C_s, which means that their only symmetry element is a mirror plane that seperates NN. The R ions in the two sublattices have different directions for their mirror plane normals corresponding to the crystallographic [110] and [1-10] axes.

Although $Nd_2Be_2SiO_7$ and $Ho_2Be_2SiO_7$ were previously investigated in the context of laser materials [74], prior to this work no investigations of the magnetic or electronic properties of these $R_2Be_2SiO_7$ compounds has been reported. The basic magnetic properties of members of the related compound family $R_2Be_2GeO_7$ [73] have been reported although difficulties in growing single crystals make further investigation difficult.

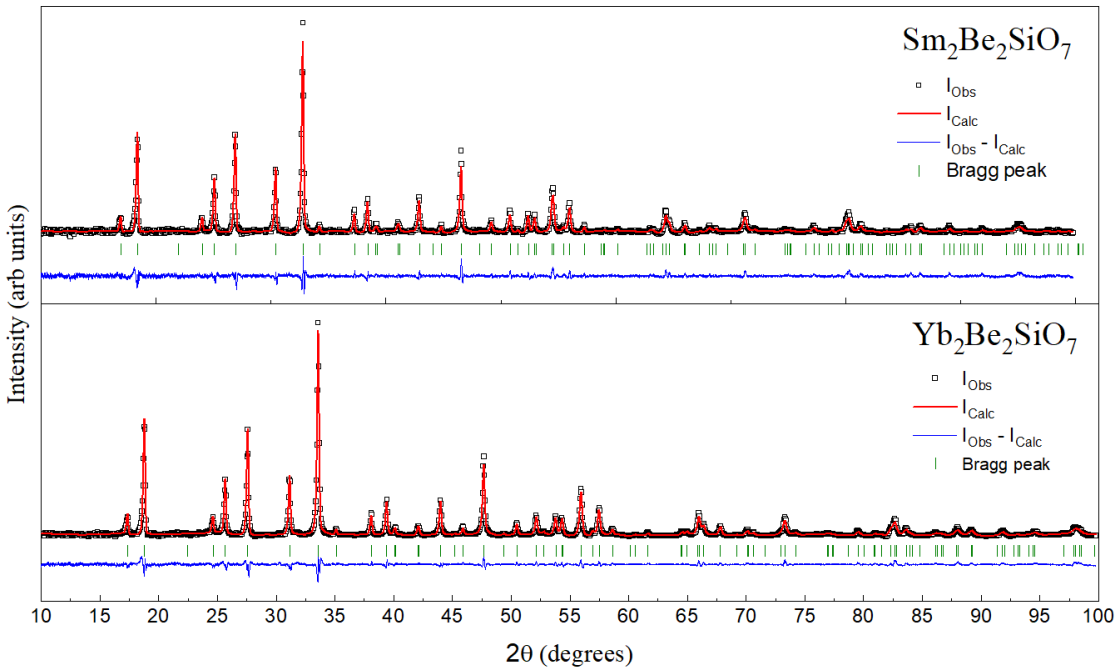

Figure 1.5: The polycrystalline XRD pattern is shown for two representative members of the $R_2Be_2SiO_7$ family. The refined structure details are presented in Table 1.1.

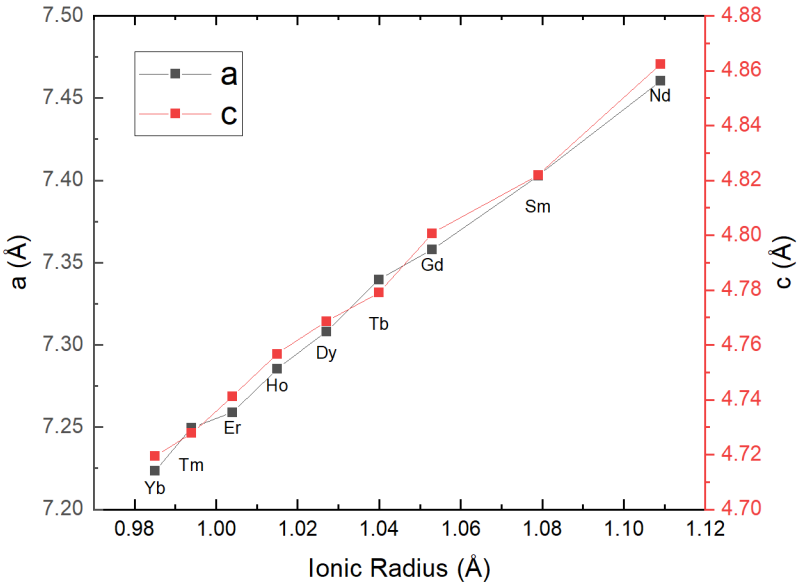

Figure 1.6: The lattice parameters a (left axis) and c (right axis) vs rare-earth ionic radius (IR) from Shannon [58]. Both lattice constants increase approximately linearly with increasing ionic radius.

Table 1.1: Summary of room-temperature XRD Rietveld refinements for $R_2Be_2SiO_7$ (R = Nd, Sm, Gd-Yb)

	Sm	**Dy**	**Ho**	**Er**	**Yb**
R^{3+} **IR (Å)**	1.079	1.027	1.015	1.004	0.985
a (Å)	7.40287(4)	7.30825(8)	7.28535(8)	7.25903(5)	7.22334(5)
c (Å)	4.82202(3)	4.76866(6)	4.75659(5)	4.74094(4)	4.71925(3)
NN bond (Å)	3.3617(7)	3.3046(10)	3.2840(9)	3.2610(8)	3.2379(6)
NNN bond (Å)	3.9312(7)	3.8844(10)	3.8749(9)	3.8635(8)	3.8462(6)
R	(x,y,z)	(x,y,z)	(x,y,z)	(x,y,z)	(x,y,z)
x	0.83945(7)	0.84013(10)	0.84063(9)	0.84117(8)	0.84152(6)
y	0.33945(7)	0.33013(10)	0.34063(9)	0.34117(8)	0.34152(6)
z	0.5002(6)	0.5028(9)	0.5048(7)	0.5037(7)	0.5039(5)
Si	(0,0,0)	(0,0,0)	(0,0,0)	(0,0,0)	(0,0,0)
Be	(x,y,z)	(x,y,z)	(x,y,z)	(x,y,z)	(x,y,z)
x	0.6481(18)	0.656(3)	0.643(2)	0.638(2)	0.637(2)
y	0.1381(18)	0.156(3)	0.143(2)	0.138(2)	0.137(2)
z	0.943(3)	0.921(3)	0.947(4)	0.949(4)	0.949(3)
$\mathbf{O_1}$	(x,y,z)	(x,y,z)	(x,y,z)	(x,y,z)	(x,y,z)
x	0.9258(8)	0.9208(10)	0.9215(9)	0.9241(9)	0.9210(7)
y	0.8364(8)	0.8395(12)	0.8375(10)	0.8364(9)	0.8376(7)
z	0.1955(9)	0.2084(12)	0.1973(11)	0.2123(11)	0.2053(8)
$\mathbf{O_2}$	(x,y,z)	(x,y,z)	(x,y,z)	(x,y,z)	(x,y,z)
x	0.6404(9)	0.6438(13)	0.6388(10)	0.6412(10)	0.6431(8)
y	0.1404(9)	0.1438(13)	0.1388(10)	0.1412(10)	0.1431(8)
z	0.2975(11)	0.2917(15)	0.2923(14)	0.2941(13)	0.2910(10)
$\mathbf{O_3}$	$(0,\frac{1}{2},z)$	$(0,\frac{1}{2},z)$	$(0,\frac{1}{2},z)$	$(0,\frac{1}{2},z)$	$(0,\frac{1}{2},z)$
z	0.159(2)	0.170(3)	0.174(3)	0.156(3)	0.163(2)
$\mathbf{R}_P$	1.28	1.42	1.69	1.77	1.75
$\mathbf{R}_{wp}$	1.81	2.15	2.76	2.85	2.72
χ^2	2.19	3.02	3.83	4.19	3.79

Magnetization and susceptibility measurements on polycrystalline sample indicate that, except for R = Tb which appears to order antiferromagnetically at ∼2.6 K, all compounds show no sign of long range order above 2 K. The main focus of this thesis is on the compounds $R_2Be_2SiO_7$ where R = Er, Dy, and Yb. Both $Er_2Be_2SiO_7$ and $Dy_2Be_2SiO_7$ order antiferromagneticly at $\sim$ 0.85 K and $\sim$ 1.1 K respectively. While two field induced transitions are observed in $Er_2Be_2SiO_7$ no magnetization plateau are observed. On the other hand, for fields applied along the [001]-axis $Dy_2Be_2SiO_7$ shows magnetization plateau at 1/7, 4/9, and 2/3 fractions of the saturation magnetization. $Yb_2Be_2SiO_7$ shows no signs of long range order above 0.05 K and a combination of neutron scattering and diffraction data suggest that its magnetic ground state consists of dimers as in $SrCu_2(BO_3)_2$. The properties of $Er_2Be_2SiO_7$, $Dy_2Be_2SiO_7$, and $Yb_2Be_2SiO_7$ are discussed in detail in chapters 3, 4, and 5 respectively.

Chapter 2

Experimental Methods

2.1 Sample Synthesis and Structural Characterization

2.1.1 Polycrystalline Preparation via Solid State Reaction

Polycrystalline samples were prepared using a KSL 1700-X high temperature muffle furnace with alumina fiber bricks and $MoSi_2$ heating elements, made by MTI Corp. Stoichiometric amounts of the appropriate rare-earth oxide, R_2O_3, (Strem Chemicals, 99.999%), SiO2 (Alfa Aesar, 99.8%), and BeO (Alfa Aesar, 99%) were ground and packed into a long cylindrical rod using a hydraulic press at a pressure of 40 psi. The general formula for the reaction is [6]:

$$R_2O_3 + [2]BeO + SiO_2 = R_2Be_2SiO_7$$

The pressed cylindrical rods were then pre-reacted in air at $1000°C$ for twenty hours. Then the rods were reground and reacted twice for twenty hours at $1300°C$ for R = Nd, Sm, Gd, Tm and at $1400°C$ for R = Dy, Ho, Er, Tm, Yb. Reactions involving R = Tb, Tm were conducted under an Argon environment using a high temperature tube furnace, STF54233C, manufactured by Lindberg/Blue M; All other reactions

were conducted in an air environment. Prior to weighing and use, all rare-earth oxides were preheated in air at $1000°C$ for at least ten hours to remove moisture.

2.1.2 Single Crystal Growth via Floating Zone Method

The floating zone method was used for the $R_2Be_2SiO_7$ crystal growth. A halogen lamp optical furnace, SC1MDH-11020 manufactured by Canon Machinery Incorporated, was used. This crucible free technique allows for the synthesis of high quality single crystals free of contaminants from a container [75, 76, 77]. The experimental design of this technique is illustrated in Fig. 2.1. The light from two halogen lamps is focused by two elliptical mirrors onto a small zone, Z, between an upper feed rod and a lower seed rod. This small zone contains molten liquid material which slowly crystallizes as the rods are moved downwards. For the first growth both the feed and seed rod are composed of packed polycrystalline material. For subsequent growths a crystalline piece is utilized as a seed rod. As the two rods are lowered they are both rotated in opposite directions, in this case at a rate of 15 RPM.

In the initial floating zone growth with polycrystalline material both rods are lowered at a fast rate of 40 mm per hour. In subsequent growths the rods are lowered at a slower rate of 5 mm per hour. For the growth of $R_2Be_2SiO_7$ crystals, similar to preparation of polycrystalline material, for R = Tb, Tm an argon environment with a pressure of 4 bar is used. For all other rare-earth elements an air environment at approximately room pressure is used.

2.1.3 Polycrystalline X-Ray Diffraction

X-ray powder diffraction (XRD) measurements were performed on all the reported compounds, $R_2Be_2SiO_7$, to check their face purity and obtain lattice information including lattice parameters and atomic positions.The measurements were performed using a HUBER imaging-plate Guinier camera 670 with Cu Kα radiation ($\lambda = 1.5418$ $\mathring{A}$) at room temperature between $4° \leq 2\theta \leq 100°$.

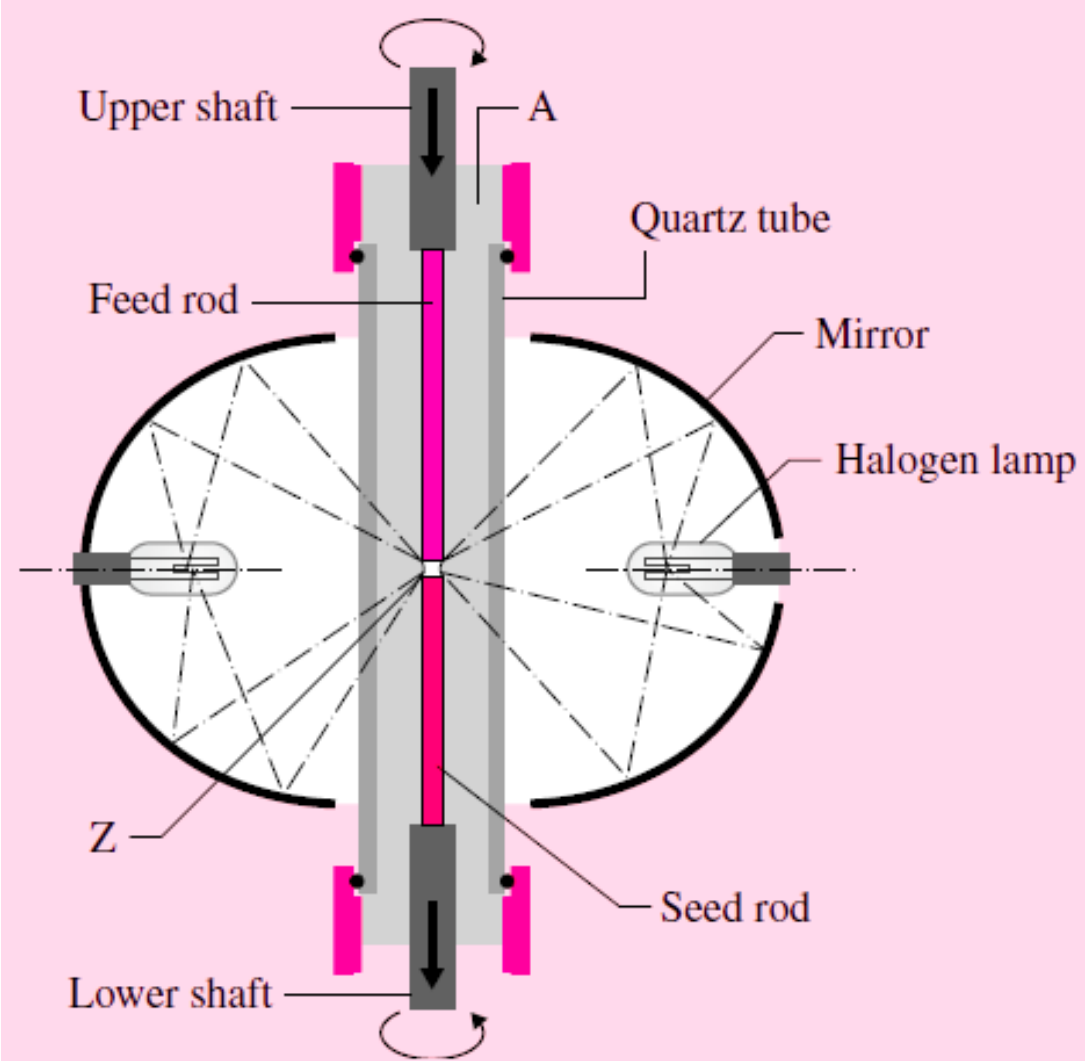

Figure 2.1: Experimental setup of the floating zone melt method. The light from two halogen lamps are focused on a small zone, Z, between a feed and seed rod. The sample material in this zone melts forming a liquid zone stabilized by surface tension. Both feed and seed rods are slowly lowered and as material exits the liquid zone it forms crystals.

The resulting XRD difractogram was analyzed via Rietveld refinement with the program FullProf [78] using the structure of $Y_2Be_2SiO_7$ [79] as a starting template. For powder XRD refinement a least squares method with a pseudo-Voigt axial divergence asymmetry peak function is used [80, 81]. The background is modeled via a linear interpolation between approximately sixty background points. No signatures of impurity phases were detected in the XRD difractogram.

2.1.4 Single Crystal X-Ray Diffraction

Single crystal X-ray Diffraction (SC-XRD) measurements were conducted on the samples produced via floating zone growth using a Bruker D8 Eco Quest X-ray Diffractometer with Mo radiation ($\lambda = 0.71073$ Å) at 300 K and the refinement was done using the Bruker SHELXTL Software Package. The crystal structure refinement was performed using the least squared method on the full matrix representation of the structure factors, $|F_{hkl}|^2$.

2.1.5 Laue Back-Diffraction

Prior to being utilized in a bulk measurement or for neutron spectroscopy all single crystals must be oriented along a high symmetry axis, e.g: [001],[100],[110]. To do this the Laue back diffraction method is used. A broad spectrum or white beam of X-rays is passed through a charge-coupled device plate (CCD plate) and incident on the crystal sample. The broad spectrum allows for scattering off several lattice planes simultaneously. Some of this scattering is back-scattering, towards the incident X-ray source, and is absorbed onto the CCD plate accumulating as a spot. Since the distance between the CCD plate and the sample are fixed the location of the spot depends only on the reflected wavelength and corresponds to a specific bravais plane. Analyzing the position of several of the spots corresponding to different bravais planes allows for the determination of the relative orientation of the crystal lattice [82].

The crystal sample can be rotated along two axes and its orientation is adjusted until the desired high symmetry direction is parallel/anti-parallel to the axis of the incident x-ray beam. The software OrientExpress [83]is used to simulate the laue pattern based on the space group and lattice information. The same software allows for the comparison of the simulated pattern to the collected pattern and thus for robust determination of the crystal orientation. Once the desired crystal axis is found the sample is glued to an aluminum plate and a plane perpendicular to this axis is cut using a low speed diamond cutting wheel to preserve the orientation.

2.2 Bulk Measurements

2.2.1 DC- Magnetic Susceptibility and Magnetization

Temperature dependent magnetization or susceptibility measurements, χ_{DC}, were performed on single crystal samples using a magnetic property measurement system (MPMS) with a super conducting interference device (SQUID) magnetometer [84, 85]. The susceptibility measurements were conducted with a field of 0.1 T over a temperature range from 1.8 K to 300 K. The temperature range is extended down to 0.4 K using a He3 insert, also by Quantum design.

Field dependent isothermal magnetization measurements, M(H), were also conducted using the MPMS system. Isothermal magnetization measurement were performed at temperatures between 1.8 K to 300 K. Isothermal magnetization measurements up to 7 T were also conducted at 0.4 K using a He3 insert. Additional isothermal magnetization measurements were performed using a physical property measurement system (PPMS) from Quantum Design. These measurements were performed on polycrystalline samples up to a maximum field of 14 T.

For all single crystal measurements a non-magnetic quartz rod is used while a straw rod is used for polycrystalline samples. Samples are adhered to the holder using a thin layer of Ge varnish. During the measurement the sample is moved

through a series of coils inducing a current via induction. This current is converted to a voltage with increased precision, compared to a typical coil magnetometer, using a superconducting quantum interference device (SQUID).

2.2.2 AC- Magnetic Susceptibility

AC susceptibility measurements, $\chi = dM/dH$ were performed at the National High Magnetic Field Laboratory (NHMFL) in Tallahassee, FL. As this method directly measures the derivative of Magnetization it is very sensitive to small chnages in Magnetization and magnetic phase transitions [86].

Measurements were performed on SCM2 and SCM1 which are He3 and dilution refrigerator cryostats with base temperatures of 0.3 K and 0.025 K, respectively. In AC susceptibility measurements a small time dependent AC-field is applied to the sample along with an optional DC field. At the NHMFL a 18 T superconducting magnet is used to apply the DC Field. A voltage controlled current source, Standford Research CS580, was used to apply the AC current with frequencies ranging from 49 Hz to 2147 Hz. The sample signal was measured via the mutual inductance technique and the resulting signal converted by lock-in amplifiers, Standford Research SR830.

2.2.3 Specific Heat Capacity

Heat capacity measurements were performed between 2 K and 300 K using a PPMS by Quantum Design. The temperature range of the measurement was extended using a He3-He4 dilution refrigerator insert with a range of 0.05 K to 4 K. For $Er_2Be_2SiO_7$ and $Yb_2Be_2SiO_7$ heat capacity measurements in fields as high as 3 T were performed using at dilution refrigerator temperatures.

For all heat capacity measurements one surface of a single crystal sample is polished and adhered to the measurement platform using a small amount of Apiezon N-grease. Before every sample measurement an addenda or background measurement is conducted over the same temperature range to model the heat capacity contribution

from the puck and addenda. The relaxation method is used to measure heat capacity. In this method a constant heat load is applied to a sample in thermal equilibrium until a certain temperature rise is achieved. The temperature of the sample is then measured as the sample cools and the resulting temperature vs time curve is fit to either a single or double exponential function, referred to as one and two tau fitting, respectively [87].

2.3 Neutron Diffraction

2.3.1 Polycrystalline Sample with HB-2A (POWDER HFIR)

Neutron powder diffraction was performed using the high-resolution HB-2A powder diffractometer at the High Flux Isotope Reactor (HFIR) of Oak Ridge National Laboratory (ORNL). Approximately 4 g of powder sample was sealed inside an aluminum can with 1 atm of helium exchange gas. Diffraction patterns were measured at He-3 temperatures as low as 0.25 K and up to 10 K. A vertically focused Ge monochromator is used to select a wavelength of 2.41 Å while a collimation of open-open-12' is used. Hb2A is ideally suited for magnetic structure determination over a 150 degree range with support for low temperature environments, application of magnetic field, and pressure [88, 89]. Refinement of the resulting diffraction pattern was done using Fulprof. The symmetry allowed magnetic structures were analyzed using SARAh [90].

2.3.2 Half-Polarized Powder Neutron Diffraction with HB2A (POWDER HFIR)

A half-polarized neutron powder diffraction (pNPD) experiment was performed using the same HB-2A collimation settings and a V-cavity to generate the polarized beam. Approximately 10 g of polycrystalline sample were pressed into pellets. For $Dy_2Be_2SiO_7$, with highly neutron absorbing Dy, the sample was diluted by 95% by

volume with Si powder. The sample was loaded in a larger Al can than the one used for the unpolarized measurements. The polarization state was controlled using a Mezei flipper to produce spin up and spin down polarized neutrons. Spin-up and spin-down diffraction patterns, with intensities denoted by I_+ and I respectively, were collected in vertical magnetic fields of 1 and 1.5 T at temperatures between 5 and 20 K using a wavelength of 2.41 Å. The diffraction patterns are collected at temperatures where the sample is in the paramagnetic state and provides information on the local site susceptibility tensor which is heavily influenced by the strong spin orbit coupling common in rare-earth magnetic ions [91]. The resulting I_+ and I diffraction patterns where analyzed with the software package Cryspy [92].

2.3.3 Single Crystal Sample with HB-3A (DEMAND HFIR)

Single crystal neutron diffraction experiments were performed on the DEMAND (HB-3A) beamline at HFIR with an incident wavelength of 1.542 Åand a Si-220 monochromator. A single crystal sample with a mass of approximately 30 mg was measured in two-axis mode in a vertical-field cryomagnet down to temperatures of 0.25 K using a He-3 insert. A magnetic field of up to 2 T was applied along the [001]-axis. Analysis of the resulting single crystal diffraction data was completed using Fulprof.

2.3.4 Single Crystal Sample with HB-2C (WAND^2 HFIR)

A single crystal neutron diffraction experiment was performed on the DEMAND (HB-2C) beamline at HFIR with an incident wavelength of 1.488 Å. A single crystal sample with a mass 20 mg was measured in a vertical-field cryomagnet down to temperatures of 280 mK using a He-3 insert. The sample was contained in a robust custom aluminum mount to prevent induced torque from the magnetic field moving the sample. The sample was oriented so that the [HK0] scattering plane was aligned horizontally to the scattering plane and a vertical magnetic field was applied along the

[001]-axis. Data reduction of the collected scattering event data was conducted using MANTID. Peak intensities produces as part of the data reduction process were used to determine the magnetic spin structure at select fields. The software BasIreps was used for symmetry analysis of the allowed magnetic structures given the space group and propagation vector. Least squared refinement of the allowed magnetic structures was done using the software package FULPROF .

2.3.5 Polycrystalline Sample with BL-21B (NOMAD SNS)

Time-of-flight neutron powder diffraction data were collected at 100 K on NOMAD at the Spallation Neutron Source (SNS) of ORNL using ∼4 g of powder. Similar measurements were carried out on ∼4.5 g of crushed single crystals and ∼2.3 g of polycrystalline $Er_2Be_2SiO_7$. The resulting measured structure factor, S(Q), was reduced with the software package ADDIE[93] with a maximum Q range of 30 Å. The software Pdfgui was used to produce the reduced pair distribution function, G(r), as a function of distance, r(Å). This provides an accurate profile of interatomic distances in the crystal allowing for the detection of off-stoichiometry or structural defects via the distorted bond distances they produce [94, 95]. The reduced pair distribution function is compared to previous crystal structure models created using X-ray or neutron diffraction.

2.4 Neutron Spectroscopy

2.4.1 Polycrystalline Sample with BL-17 (SEQUOIA SNS)

Inelastic neutron scattering on polycrystalline sample was performed on the direct geometry time-of-flight chopper spectrometer (SEQUOIA) at the Spallation Neutron Source (SNS) at ORNL [96]. Data were collected at 5 and 25 K with incident energies, E_i, of 25 and 80 meV. For these measurements, the fine Fermi chopper was spun at 240 or 480 Hz and the T_0 chopper setting was 60 or 90 Hz. Spectra were collected

with the same instrument settings on a similar mass of the non-magnetic reference sample $Lu_2Be_2SiO_7$ to facilitate a background subtraction of the phonon spectra. The background subtracted spectrum was analyzed with the software DAVE to identify crystal electric field energy levels and other magnetic scattering phenomenon.

2.4.2 Polycrystalline Sample with BL-18 (ARCS SNS)

Inelastic neutron scattering on polycrystalline sample was performed on the Wide Angular-Range Chopper Spectrometer (ARCS) at the Spallation Neutron Source (SNS) at ORNL. To minimize neutron absorption by the highly neutron absorbing Dy nuclei the sample was sealed in a flat square can with the smallest dimension being ∼0.5 mm and aligned along the path of the neutrons. Data were collected at 10 K with incident energies, E_i, of 25, 60 and 200 meV. For these measurements, the fine Fermi chopper was spun at 240 or 480 Hz and the T_0 chopper setting was 60 or 90 Hz. The spectrum was analyzed with the software DAVE to identify crystal electric field energy levels and other magnetic scattering phenomenon [97].

2.4.3 Polycrystalline Sample with BL-5 (CNCS SNS)

Lower incident energy inelastic neutron scattering data were measured with the direct-geometry time-of-flight instrument CNCS at the SNS using a polycrystalline sample. The CNCS data were collected using incident energies of E_i =1.55 meV and 2.44 meV in the "high flux" chopper setting mode, which produced energy resolutions of 0.04 meV and 0.06 meV (full-width half-maximum) at the elastic line respectively [98, 99]. Data were collected at temperatures between 0.25 K and 100 K with a He3 insert.

Chapter 3

Magnetic Properties of $Er_2Be_2SiO_7$

This chapter is dedicated to the investigation of the magnetic properties of the Shastry-Sutherland lattice magnet $Er_2Be_2SiO_7$. The strong spin-orbit coupling of the Er^{3+} ions in this compound produces highly anisotropic magnetic moments. The presence of a low lying crystal electric field level indicates that an effective spin-half model, J_{eff} =1/2, is not appropriate. At very low temperatures the observed magnetic properties are consistent with classical anisotropic moments.

The investigation of $Er_2Be_2SiO_7$ begins with the first reported synthesis of polycrystalline sample as previously described in the experimental methods section of this text. The phase purity of the resulting polycrystalline sample is confirmed via XRD. The resulting X-ray difractogram is refined with the software FULPROF where the previously reported structure of $Y_2Be_2SiO_7$ is used as a starting template. Single crystal samples were grown via the floating zone melt method and oriented using the laue back-diffraction. Single crystal XRD measurements confirm the previously refined structural model [100].

The properties of the resulting single crystals were checked with ac-magnetic susceptibility, magnetization, and heat capacity measurements. A magnetic phase transition consistent with antiferromagnetic order is observed at T_N = 0.84 K. Inelastic neutron diffraction reveals the presence of a [0,0,1/2] propagation vector

alongside spin structure of the moments in zero field. The application of magnetic field along the [001]-axis induces two magnetic transitions.

Neutron scattering experiments were conducted on polycrystalline sample to investigate the crystal electric field Hamiltonian of this compound. All seven crystal electric field energy levels expected from the Kramer's ion Er^{3+} are observed. Several possible solutions to the crystal electric field Hamiltonian are suggested using the software CrysfieldExplorer [101]. However, the determination of a robust solution set is challenging given the low symmetry of the system and remains an area of active investigation.

3.1 Bulk Characterization

The fractional atomic positions and lattice parameters determined via single crystal XRD as described in Section 2.1.4 and are given in Table 3.1. The single crystal results agree well with previous XRD results on polycrystalline sample.

Single crystal samples grown via the previously described floating zone melt method were oriented then using the laue back-diffraction method as detailed in section 2.1.5. A laue photograph along the [001] crystallographic direction is shown in Fig 3.1. While orienting the crystal samples some domains with multiple nearly overlapping points are observed. This is due to multiple crystal grains with slightly differing orientations. Large single domain grains were carefully isolated and cut from the boule. The as grown boule and a cut single crystal piece of $Er_2Be_2SiO_7$ is shown in Fig 3.2.

3.1.1 Heat Capacity

Fig 3.3 shows the heat capacity as a function of sample temperature with varying magnetic fields applied along the [001], [100], and [110] axes. In zero field all three directions show a lambda anomaly indicative of antiferromagnetic order at ∼0.84 K.

Table 3.1: Atomic coordinates and isotropic displacement parameters U_{eq} (Å^2). All sites are fully occupied.

Space Group: Tetraganol, P-42$_1$m, No. 113 **Unit Cell:** $a = b = 7.2572(4)$ Å and $c = 4.7396(3)$ Å					
Atom	Wyck.	x	y	z	U_{eq}
Er	4e	0.15907(3)	0.65907(3)	0.50719(8)	0.0041(19)
Si	2a	0	0	0	0.0036(5)
Be	4e	0.6352(14)	0.1352(14)	0.960(3)	0.0060(18)
O_1	2c	0	1/2	0.180(2)	0.0069(17)
O_2	4e	0.6411(7)	0.1411(7)	0.2934(5)	0.0041(11)
O_3	8f	0.0816(8)	0.1634(7)	0.2017(10)	0.0050(8)

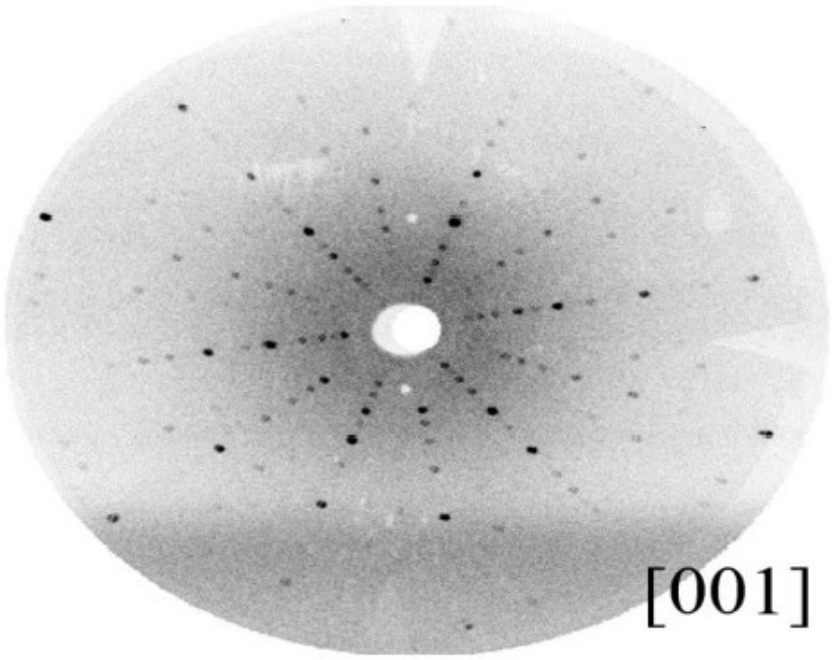

Figure 3.1: The Laue pattern generated with the incident x-ray beam along the crystallographic [001]-axis.

Figure 3.2: An as-grown crystal boule of $Er_2Be_2SiO_7$ and a small oriented crystal grain.

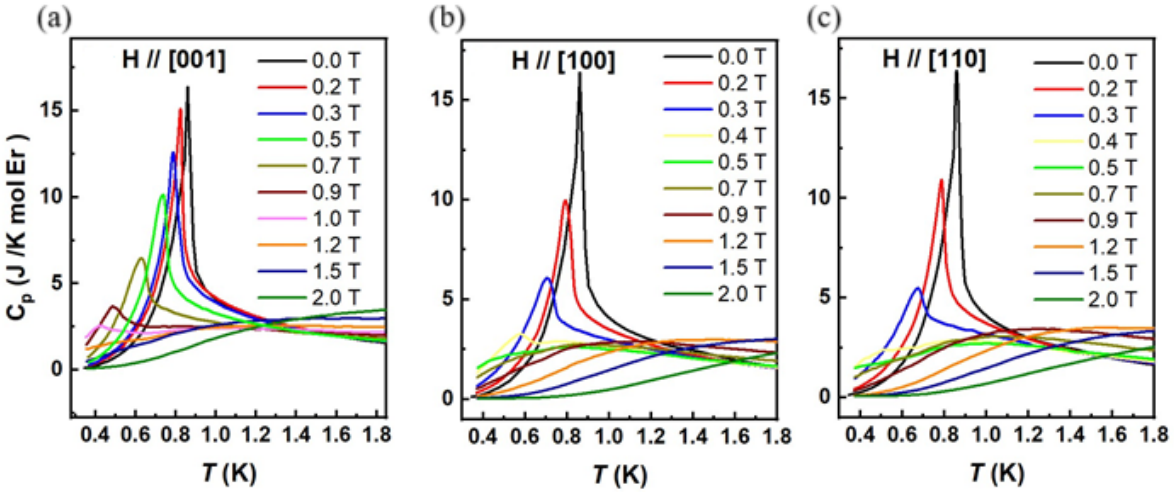

Figure 3.3: Heat capacity data C_p vs T with field along [001], [100], and [110] crystal directions. In each case, the zero-field λ anomaly indicative of magnetic order is suppressed with increasing field and replaced by a broad hump in the higher field range. The onset of the polarized phase occurs at a much higher field for $H \parallel [001]$ due to the significant magnetic anisotropy of this system.

In each case the zero-field peak is suppressed and shifted towards lower temperatures with increasing magnetic field. The rate of this suppression and the field required to completely suppress the peak varies with direction to due to the significant magnetic anisotropy of the system. The peak is more readily suppressed for fields along the [110] and [100] directions and is absent in fields greater than 0.4 T. A much larger field of 1.2 T is required along the [001]-axis. A broad field dependent hump which is more obvious at higher fields is also visible along all three directions. This hump is due to the occupation of a very low lying crystal electric field level at ∼1.75 meV and appears to be field dependent.

3.1.2 DC-Magnetic Susceptibility

Fig 3.4 shows the T-dependence of both the magnetic susceptibility χ (plotted as M/H) and its inverse $1/\chi$ along three high-symmetry crystallographic directions. $1/\chi$ does not have a linear T-dependence throughout the entire range measured due to the decreased population of excited Er^{3+} crystal field levels with decreasing temperature. The $1/\chi$ data was first fit to a Curie-Weiss law in the high-temperature range 150-300 K and we found that the Er^{3+} effective moment agrees well with expectations for a free ion system, with a small variation for the different datasets. The values were 9.3597(4) μ_B for $H \parallel [001]$, 9.4618(2) μ_B for $H \parallel [110]$, and 9.6158(2) μ_B for $H \parallel [100]$. Using the same fit range the Curie-Weiss (θ_{cw}) temperatures obtained for each direction are 16.30(6) K for $H \parallel [001]$, -25.76(4) K for $H \parallel [110]$, and -41.64(3) K for $H \parallel [100]$. We proceeded to perform another fit to the same Curie-Weiss function in the low-temperature range 2-6 K. The Curie-Weiss temperatures θ_{cw} are negative for all three datasets, with values of -4.29(4) K for $H \parallel [001]$, -2.15(3) K for $H \parallel [110]$, and -1.77(3) K for $H \parallel [100]$. The effective moments obtained using the low temperature fit range are 9.649(5) K for $H \parallel [001]$, 7.630(3) K for $H \parallel [110]$, and 7.276(3) K for $H \parallel [100]$.

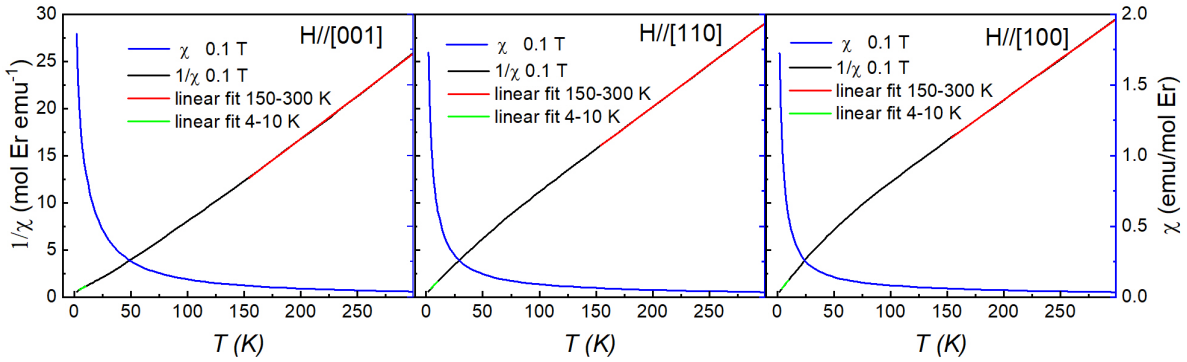

Figure 3.4: $1/\chi$ (left) and χ (right) vs T for $H \parallel [001]$, $H \parallel [110]$, and $H \parallel [100]$ collected at 0.1 T. Linear fits are performed between 150-300 K and 2-6 K. The obtained θ_{cw} and μ_{eff} values are noted in the text.

The sign of θ_{CW} indicates that $Er_2Be_2SiO_7$ has dominant antiferromagnetic exchange interactions, which is likely due to an antiferromagnetic intradimer coupling. Additional temperature dependent magnetic susceptibility measurements were conducted using a Quantum Design MPMS3 with an He3 insert. The susceptibility vs temperature and its derivative for the high symmetry crystal directions [001], [100], and [110] are shown in Fig 3.5. The average T_N extracted from the derivative of susceptibility for the three directions is ∼0.844 K. in good agreement with heat capacity data.

3.1.3 DC-Magnetization

DC magnetization M vs field H and its derivative is shown at selected temperatures for these three high-symmetry directions in Fig 3.6. Although magnetization plateaus are often observed in SSL systems, there is no evidence for them in this data. The in-plane field dependence of both M and dM/dH appears to be quite simple, with only one abrupt slope change in the 0.4 K magnetization data around 0.3-0.4 T corresponding to a large peak in dM/dH. This behavior is indicative of a single metamagnetic transition from the zero-field ground state established above to the field-polarized phase. The real part of the AC susceptibility shows similar behavior. The $H \parallel [001]$ data on the other hand clearly shows two meta-magnetic transitions at ~ 0.34 T and ~ 1.05 T. The transitions above ~ 1.05 T results in a fully polarized phase.

3.1.4 AC-magnetic susceptibility

The real part of the ac-susceptibility data is shown in Fig 3.7. The data was collected at the National High Magnetic Field Laboratory (NHMFL) in Florida using the SCM2, He3 cryostat, and SCM1, dilution refrigerator cryostat. In agreement with magnetization data collected at 0.4 K, the in-plane ac-susceptibility data shows only a single field dependent transition before saturation.

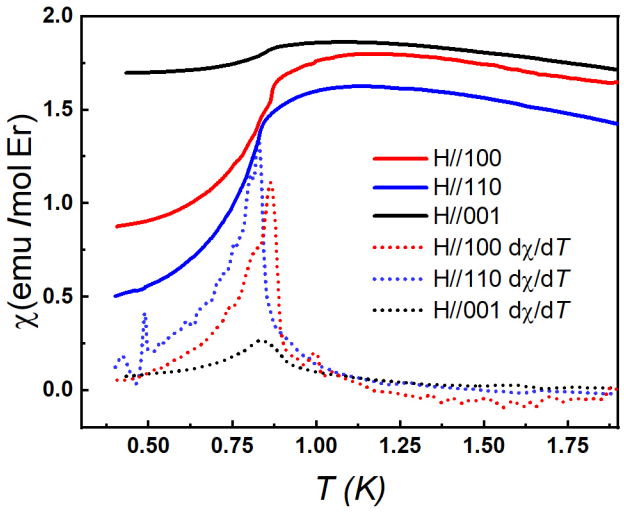

Figure 3.5: The DC susceptibility (χ) and its derivative ($\mathrm{d}\chi/dT$) vs T measured at 0.1 T along three high-symmetry crystallographic directions.

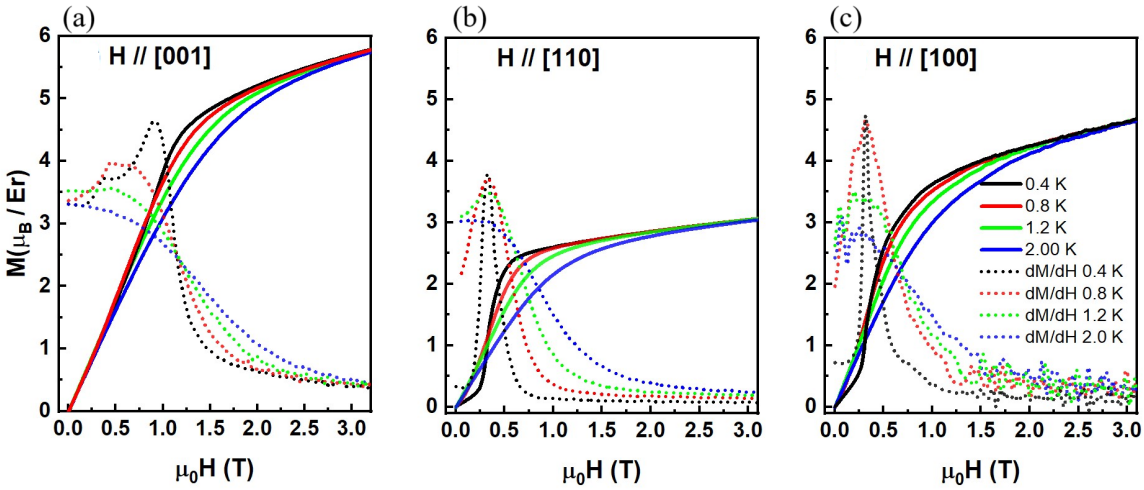

Figure 3.6: DC magnetization and dM/dH vs H for applied magnetic fields along the [001], [110], and [100] directions at select temperatures. While only a single peak in dM/dH indicative of one metamagnetic phase transition is visible in the low-T in-plane field data, there are at least two dM/dH peaks for $H \parallel [001]$.

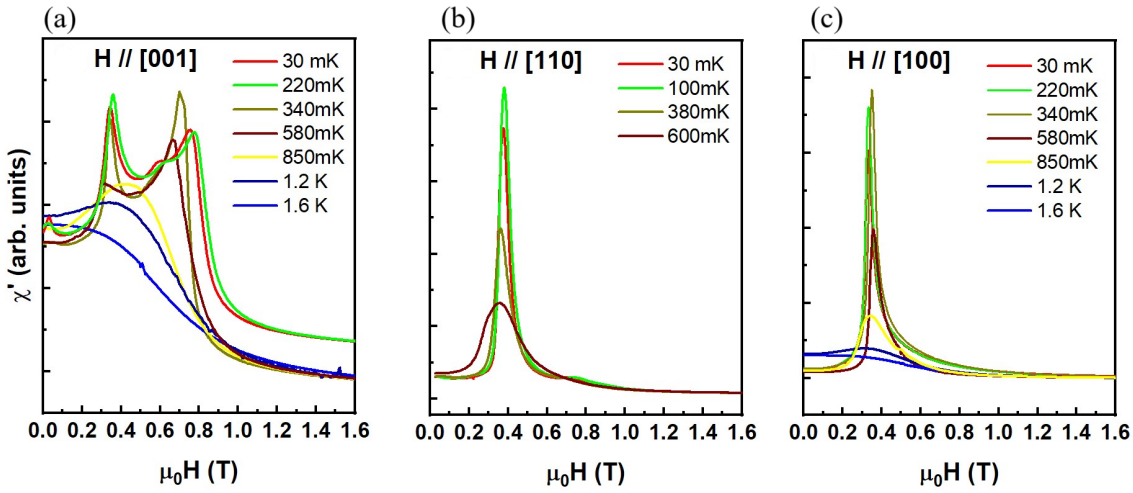

Figure 3.7: The real component of the AC susceptibility χ' vs H. While the results generally agree with the DC magnetization, there is an extra peak in the lowest-T $H \parallel [001]$ χ' data which suggests that the H-T phase diagram becomes more complex below 0.4 K. The appearance of peaks in the χ' data at slightly lower fields, compared to the magnetization results, is likely due to a slight sample misalignment.

On the other hand, the [001] data shows two transitions above 0.34 K in agreement with magnetization data. At temperatures below 0.34 K a possible third metamagnetic transition appears at roughly 0.6 T.

3.2 Zero-Field Spin Structure via Neutron Diffraction

Neutron diffraction data was collected on polycrystalline sample at the HB-2A beamline at ORNL, as described in section 2.3.1. Approximately 4 g of sample was sealed in an aluminum can and diffraction patterns were collected at 0.28 and 4 K using a wavelength of 2.41 Å. Data collected at 4 K above T_N is refined with only the nuclear phase and an aluminum background phase. The resulting fit pattern is compared to the measured pattern in Fig 3.8(a) and agrees with previous powder-XRD and single crystal XRD refinements. No evidence of structural distortions was detected.

The diffraction pattern at 0.28 K is shown in Fig 3.8(b) and clearly shows additional peaks, not present at 4 K above T_N, associated with an ordered magnetic phase. The position of these peaks was indexed using K-search, a Fulprof application. We find that these additional peaks are well indexed by a (0,0,1/2) propagation vector and that there are five symmetry allowed irreducible representations in Kovalev's notation. The Γ_1 - Γ_4 IRs correspond to spin states with AFM dimers, while the Γ_5 IR has ferromagnetic (FM) dimers.

The Γ_1 and Γ_3 magnetic structures have their moments confined to the local directions perpendicular to the dimer bonds in the *ab*-plane, with Γ_1 and Γ_3 consisting of two different square plaquette spin configurations. The Γ_2 and Γ_4 magnetic structures can have in-plane moments parallel to the dimer bonds, out-of-plane moments, or some combination of both.

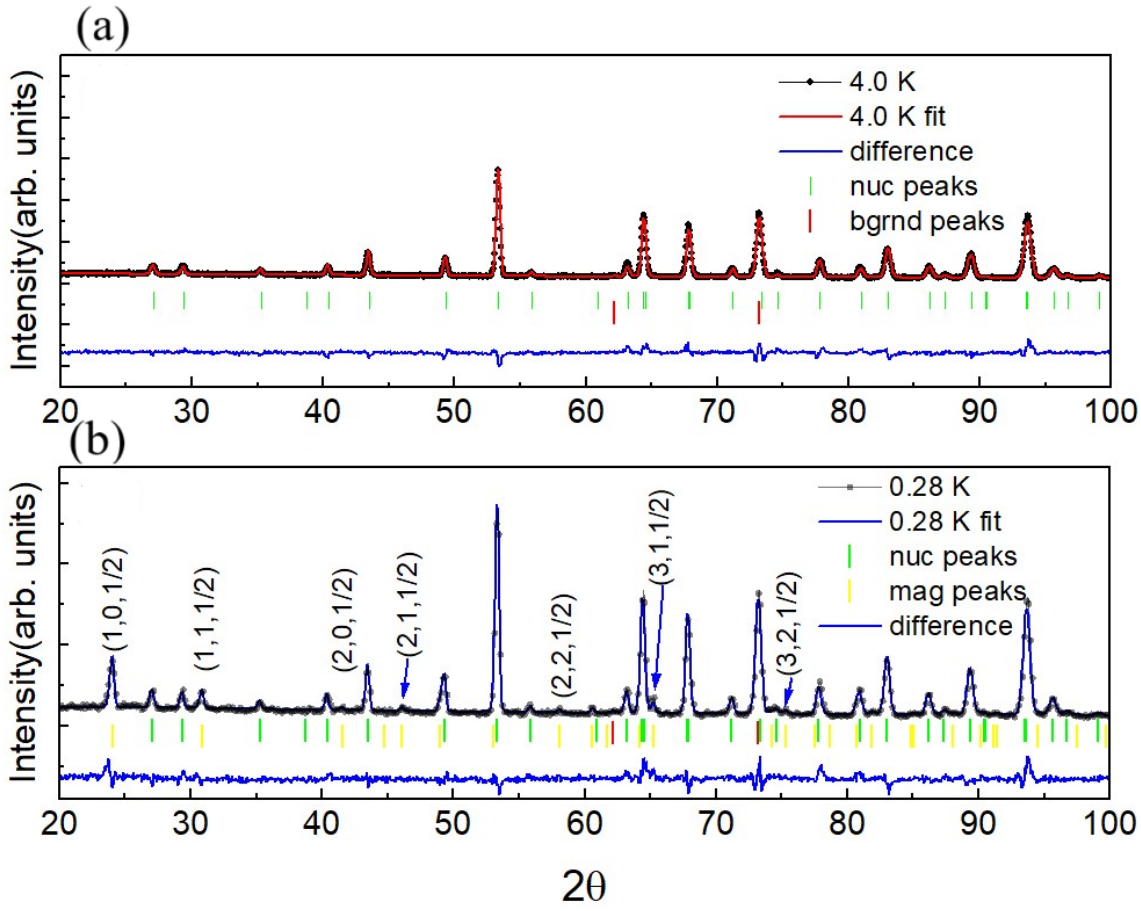

Figure 3.8: (a) The neutron powder diffraction pattern collected at 4 K (above T_N). The best Rietveld refinement result is superimposed on the data. The nuclear Bragg peaks from the sample and the background are indicated by green and red ticks respectively and the difference curve is shown below the Bragg peaks. (b) The neutron powder diffraction pattern collected at 0.28 K (below T_N). The best Rietveld refinement result, which now includes a magnetic phase, is again superimposed on the data. The magnetic Bragg peaks are denoted by the yellow ticks.

There are two main differences between them. First, the Γ_4 in-plane moments form a magnetic state with a definite handedness, but this is not true for Γ_2. Secondly, in a given SSL plane the c-axis moments are parallel for the Γ_2 structure, while they are anti-parallel for the two dimer sublattices of the Γ_4 configuration. Schematics for the in-plane moment configurations of the Γ_1 to Γ_4 magnetic structures are shown in Fig 3.9(a). Γ_1 one yields the structure with the best fit and is shown in Fig 3.9(b).

3.3 The Crystal Electric Field Hamiltonian and Single Ion Anisotropy

To investigate quantitative details of the magnetic anisotropy induced by crystal fields, inelastic neutron scattering (INS) measurements on a polycrystalline sample of $Er_2Be_2SiO_7$ were conducted using the time-of-flight chopper spectrometer SEQUOIA. Datasets were collected with incident energies of 25 meV and 80 meV at temperatures of 5 and 25 K to measure the crystal field levels associated with the $J = 15/2$ ground state multiplet of Er^{3+} and the virtual transitions created by thermally-populating the lowest-lying crystal field level. Er^{3+} is a Kramers ion, so the crystal field ground state must be at least two-fold degenerate. Each Er ion is surrounded by eight oxygen ions that generate a monoclinic C_s environment. The low-symmetry of this point group is expected to produce maximal splitting of the 16 levels associated with the $J = 15/2$ ground state multiplet, so up to 7 excited crystal field doublets may be visible in the low-temperature INS data.

Fig 3.10 (a) and (b) present color contour plots of the $E_i = 25$ meV and 80 meV datasets respectively at 5 K. The phonon spectra from a non-magnetic reference sample of $Lu_2Be_2SiO_7$ were subtracted off from these data. There are three strong, flat modes in the lower incident energy dataset centered about energy transfers of 1.75 meV, 5.22 meV, and 13.73 meV, with two additional strong modes visible in the other dataset centered about energy transfers of 22.54 meV and 27.87 meV.

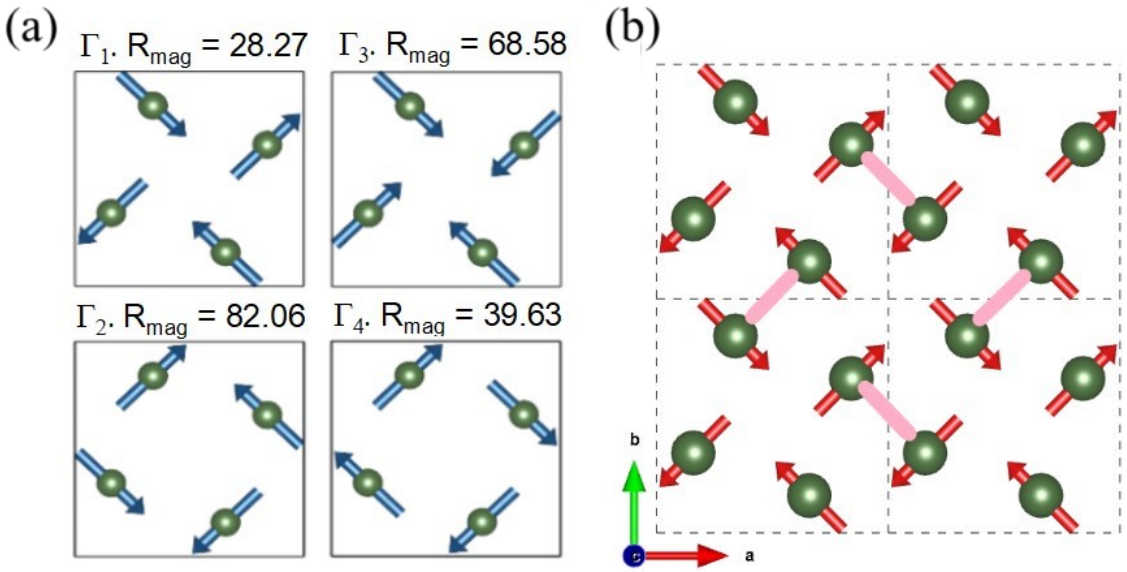

Figure 3.9: (a) Schematics of the in-plane spin-structures for the Γ_1 to Γ_4 models. The R_{mag} values for the best refinements (which include out-of-plane components when allowed by symmetry) using each of these models are also shown. (b) The spin configuration of the Γ_1 magnetic structure realized by $Er_2Be_2SiO_7$ below T_N, with the dimer bonds shown in pink. The moments have a magnitude of 2.47(3) μ_B and each square plaquette consists of two moments pointing into it and two pointing out.

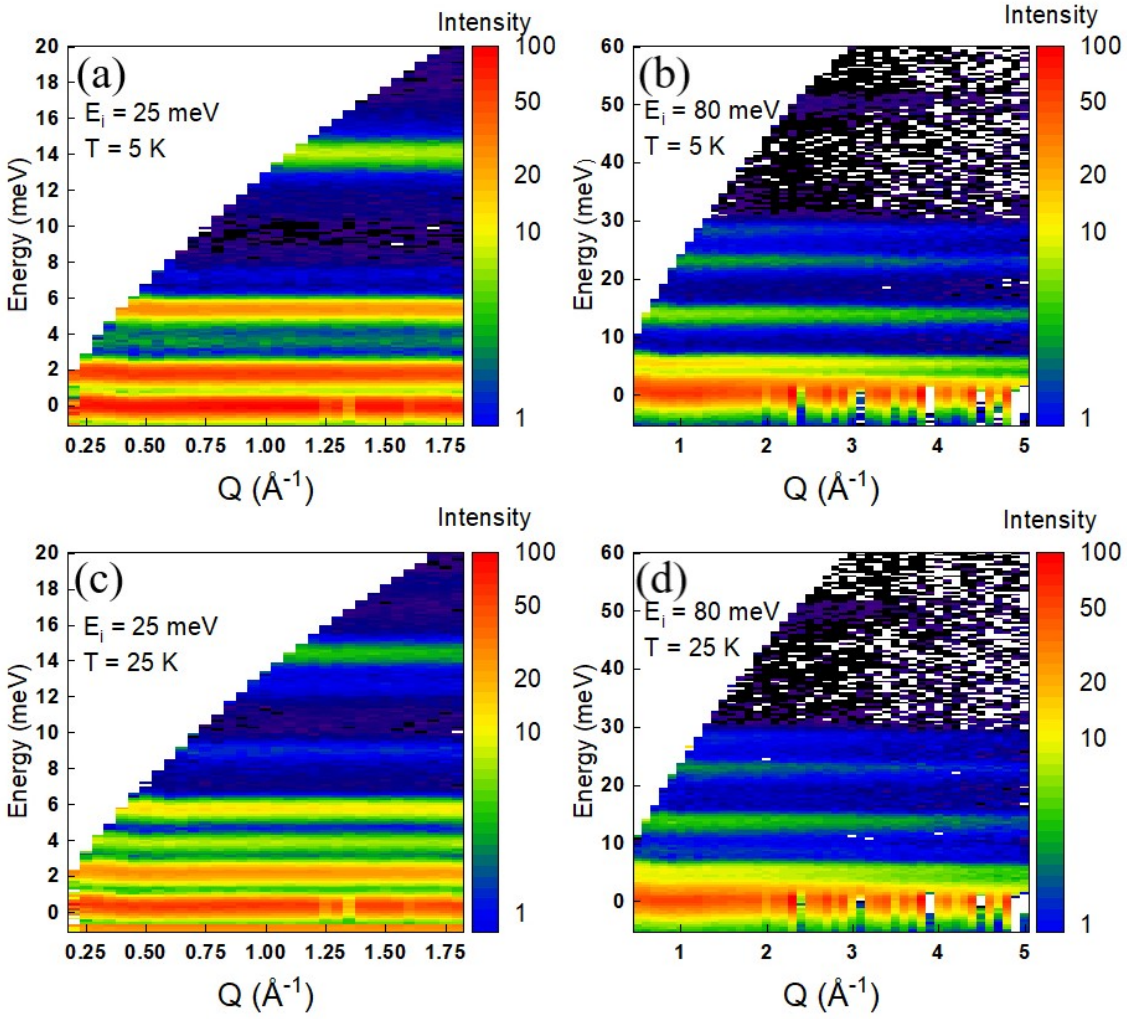

Figure 3.10: Color contour plots of the scattering intensity (in arb. units) as a function of momentum transfer Q and energy transfer E for the following datasets: (a) $E_i = 25$ meV, $T = 5$ K, (b) $E_i = 80$ meV, $T = 5$ K, (c) $E_i = 25$ meV, $T = 25$ K, (d) $E_i = 80$ meV, $T = 25$ K. Several crystal field excitations from Er^{3+} are visible in this data.

Three weaker modes are also present at energy transfers of 3.47 meV, 7.12 meV, and 49.46 meV. All eight modes have a magnetic origin, as their intensities decrease monotonically with increasing Q. The higher temperature data collected at 25 K is shown in Fig 3.10 (c) and (d) and proved invaluable for elucidating the crystal field scheme. While seven of the eight modes previously observed had reduced intensity at 25 K, the intensity of the 3.47 meV mode was enhanced. This finding suggests that this mode corresponds to a virtual crystal field transition. Indeed, the energy of this mode corresponds to the difference between the first and second excited doublets.

Therefore, the other seven levels observed at 5 K are the expected transitions associated with the ground state doublet. There are several other virtual crystal field transitions observed in the 25 K datasets as well, with the most prominent features centered at 8.51 meV and 11.98 meV. The energy levels and integrated intensities of these CEF excitations have been extracted by fitting constant Q-cuts (integration range of 1.5 to 2 Å^{-1} and 3 to 3.5 Å^{-1} for the $E_i = 25$ meV and 80 meV datasets respectively) to a sum of Lorentzian functions with a linear background. The integrated intensities of the crystal field modes above 20 meV were normalized by a scale factor obtained by comparing the integrated intensities of the 13.73 meV mode in both the low and high-incident energy datasets. A list of all observed CEF transitions is provided in Table 3.2.

To ensure that all the crystal field parameters are real, we choose the local y-axis to be perpendicular to the mirror plane associated with the C_s point group. As mentioned above, this corresponds to the [110] crystallographic direction for one of the dimer sublattices and it is guaranteed to be one of the principal g-tensor directions by symmetry. On the other hand, the two principal g-tensor directions in the xz-plane are strongly dependent on the details of the surrounding ligands and they are not known a priori. Our choice of y-axis generates the following CEF Hamiltonian with 15 terms:

$$\begin{aligned}\mathcal{H} =& B_2^0\hat{O}_2^0 + B_2^1\hat{O}_2^1 + B_2^2\hat{O}_2^2 + B_4^0\hat{O}_4^0 + B_4^1\hat{O}_4^1 + B_4^2\hat{O}_4^2 \\ &+ B_4^3\hat{O}_4^3 + B_4^4\hat{O}_4^4 + B_6^0\hat{O}_6^0 + B_6^1\hat{O}_6^1 + B_6^2\hat{O}_6^2 + B_6^3\hat{O}_6^3 \\ &+ B_6^4\hat{O}_6^4 + B_6^5\hat{O}_6^5 + B_6^6\hat{O}_6^6.\end{aligned}$$

where B_n^m and $\hat{O}_n^m$ represent the crystal field parameters and the corresponding operators in Stevens notation. Note that $B_n^m = \lambda_n^m \theta_n A_n^m$, where λ_n^m are normalization constants, θ_n are constants associated with the electron orbitals of Er^{3+}, and A_n^m are the crystal field parameters in Wybourne notation.

The standard approach for determining crystal field parameters from INS data for higher point-symmetry systems is to perform a point charge calculation to obtain reasonable starting values and then refine the parameters through a least-squares fitting process with the data using the typical χ^2 minimization function. For an under-constrained problem with a low point symmetry such as the present case, there is a strong likelihood that this procedure will not result in a meaningful solution since the fitting routine may get stuck in the same local minimum each time. To mitigate this issue and facilitate quick comparisons between INS data and crystal field models, the software package CrysFieldExplorer was developed recently. One key advantage of CrysFieldExplorer is the use of a revised cost/loss function for comparing the experimental and calculated CEF energy levels, which significantly reduces the likelihood of getting stuck in local minima. CrysFieldExplorer also takes advantage of high-performance parallel computing so rapid searches through complex parameter spaces can be conducted. This allows one to bypass the crystal field point charge calculation step in the determination of crystal field parameters from INS data and set up a random parameter initialization instead so that the parameter space search is not biased towards particular local minima. Note that CrysFieldExplorer reports crystal field parameters as B_n^m/θ_n. The best two solution are compared to data in Fig 3.11 and the corresponding Stevens parameters for the best five solutions are provided in Table 3.3.

Table 3.2: Measured CEF energy levels and the integrated intensities for all the transitions measured with INS. When the initial state corresponds to the CEF ground state doublet (i.e. 0), the data was collected at 5 K. Otherwise, the data was collected at 25 K. All the measured integrated intensities were normalized to the value for the 1.75 meV mode. The calculated integrated intensities for the two most probable CEF parameter sets discussed in the main text are also presented.

Transition	E_{obs}(meV)	I_{obs}	I_{calc1}	I_{calc2}
0 - 1	1.75(3)	1.0	1.0	1.0
0 - 2	5.22(3)	0.43(6)	0.408	0.357
0 - 3	7.12(5)	0.007(3)	0.020	0.029
0 - 4	13.73(1)	0.160(6)	0.152	0.156
0 - 5	22.54(5)	0.073(7)	0.047	0.078
0 - 6	27.87(8)	0.025(4)	0.016	0.021
0 - 7	49.46(11)	0.0064(9)	0.013	0.006
1 - 2	3.47	0.20(3)	0.192	0.227
2 - 4	8.51	0.040(3)	0.048	0.044
1 - 4	11.98	0.022(5)	0.005	0.006

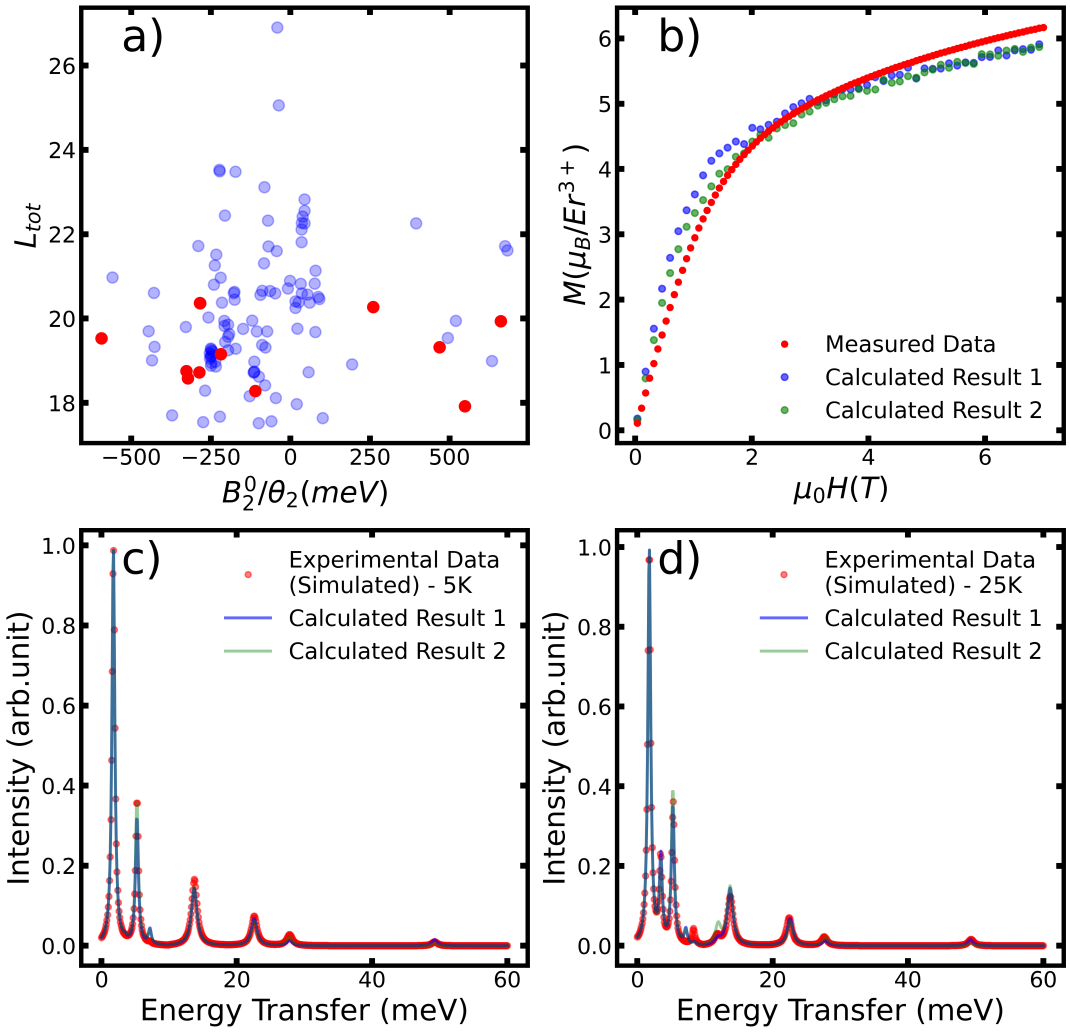

Figure 3.11: (a) The loss function value vs B_2^0/θ_2 for all 129 crystal field parameter solutions determined by CrysFieldExplorer. The solid red circles represent the six unique solutions that are consistent with the known magnetic anisotropy of the system and satisfy the hard g-tensor constraints as discussed in the main text. (b) A comparison of the calculated (blue and green circles) vs measured (red circles) powder-averaged magnetization. The calculated magnetization curves for the two most probable crystal field solutions (as discussed in the main text) are shown. (c),(d) A comparison of the calculated (blue and green curves) vs simulated experimental INS spectra (red circles) at 5 K and 25 K respectively. The calculated spectra for the two most probable crystal field solutions are superimposed on the simulated data.

Table 3.3: The crystal field parameters (in Stevens notation), the diagonal g-tensor components, and the L_{tot} values for the six unique solutions identified with CrysFieldExplorer that are consistent with the known magnetic anisotropy of the system and satisfy the hard g-tensor constraints discussed in the main text. The crystal field parameters are provided in units of meV.

B_n^m	1	2	3	4	5
B_2^0	-9.32×10^{-2}	-1.95×10^{-2}	-6.86×10^{-2}	-6.55×10^{-2}	-1.28×10^{-1}
B_2^1	0	0	0	0	0
B_2^2	1.88×10^{-1}	2.97×10^{-1}	2.53×10^{-1}	2.49×10^{-1}	2.64×10^{-1}
B_4^0	4.93×10^{-5}	2.31×10^{-4}	5.33×10^{-4}	3.18×10^{-4}	1.35×10^{-4}
B_4^1	-1.75×10^{-3}	-8.48×10^{-4}	4.13×10^{-3}	-3.44×10^{-3}	-3.34×10^{-5}
B_4^2	-2.20×10^{-3}	-2.66×10^{-3}	-5.46×10^{-4}	-1.03×10^{-3}	-1.82×10^{-3}
B_4^3	1.08×10^{-2}	4.20×10^{-3}	-7.33×10^{-3}	9.59×10^{-3}	1.04×10^{-2}
B_4^4	3.21×10^{-3}	3.27×10^{-3}	3.17×10^{-4}	-6.70×10^{-5}	6.70×10^{-4}
B_6^0	5.44×10^{-7}	-2.57×10^{-6}	-3.17×10^{-6}	-6.71×10^{-6}	1.72×10^{-6}
B_6^1	-5.84×10^{-6}	-6.56×10^{-5}	-1.24×10^{-5}	2.86×10^{-5}	1.10×10^{-5}
B_6^2	2.09×10^{-5}	9.36×10^{-6}	1.43×10^{-5}	1.99×10^{-5}	2.24×10^{-6}
B_6^3	-3.87×10^{-5}	6.25×10^{-6}	7.82×10^{-5}	-4.78×10^{-5}	-6.85×10^{-5}
B_6^4	-2.96×10^{-5}	-2.17×10^{-5}	-7.60×10^{-5}	8.13×10^{-7}	-4.24×10^{-5}
B_6^5	1.65×10^{-4}	4.70×10^{-5}	1.80×10^{-6}	1.50×10^{-5}	4.84×10^{-5}
B_6^6	-5.49×10^{-5}	-1.31×10^{-5}	-5.22×10^{-5}	-4.18×10^{-5}	1.78×10^{-5}
g_{xx}	2.57	2.33	1.72	0.03	0.57
g_{yy}	9.48	9.57	10.1	8.81	9.76
g_{zz}	6.62	7.02	6.96	8.12	7.80
L_{tot}	18.64	19.28	19.56	19.73	20.01

3.4 Field Induced Spin Structure

Fig 3.12 shows DC magnetization vs applied field at 2 K. Interestingly, the saturation magnetization ratio between the [110] and [100] directions, $M_{sat}^{110}/M_{sat}^{100}$, is almost exactly $\sin(45°) = 1/\sqrt{2}$. This observation can be used to draw some general conclusions about the Er^{3+} single ion anisotropy in this system. Since the SSL can be described as two interpenetrating square networks of orthogonal dimers, the measured anisotropy in the *ab*-plane magnetization can arise from a combination of a [110] easy axis and a [1-10] hard axis for one dimer sublattice and vice versa for the second dimer sublattice. A [110] applied field would then only polarize one sublattice while the other would not respond to it at all. For a [100] applied field, both sublattices would contribute to the field-polarized state in an equivalent manner, as all moments would have a component along the field direction but they would remain parallel to their [110] easy-axis direction. Schematics of the expected field-polarized states for the [100] and [110] applied field directions that are consistent with the anisotropic saturation magnetization values are shown in Fig 3.12 (b) and (c). Similar in-plane anisotropy has been observed in other magnetic systems with a SSL geometry, including Yb_2Pt_2Pb and $BaNd_2ZnS_5$.

The saturation magnetization ratio of $M_{\text{sat}}^{110}/M_{\text{sat}}^{001} \approx 1/2$ provides additional insight into the Er^{3+} single ion anisotropy. Based on the established *ab*-plane anisotropy, the [001] saturation magnetization can be explained by a simple field-polarized state with the moments from both sublattices aligned with the field. Since the low-field magnetization slopes are nearly equivalent for the [110] and [001] field directions when scaling the former dataset to account for the decreased number of moments contributing to the response, $Er_2Be_2SiO_7$ appears to be an XY (or quasi-XY) magnet. This behavior differs strongly from observations for Yb_2Pt_2Pb and $BaNd_2ZnS_5$, where the *c*-axis turned out to be a hard direction for the magnetization.

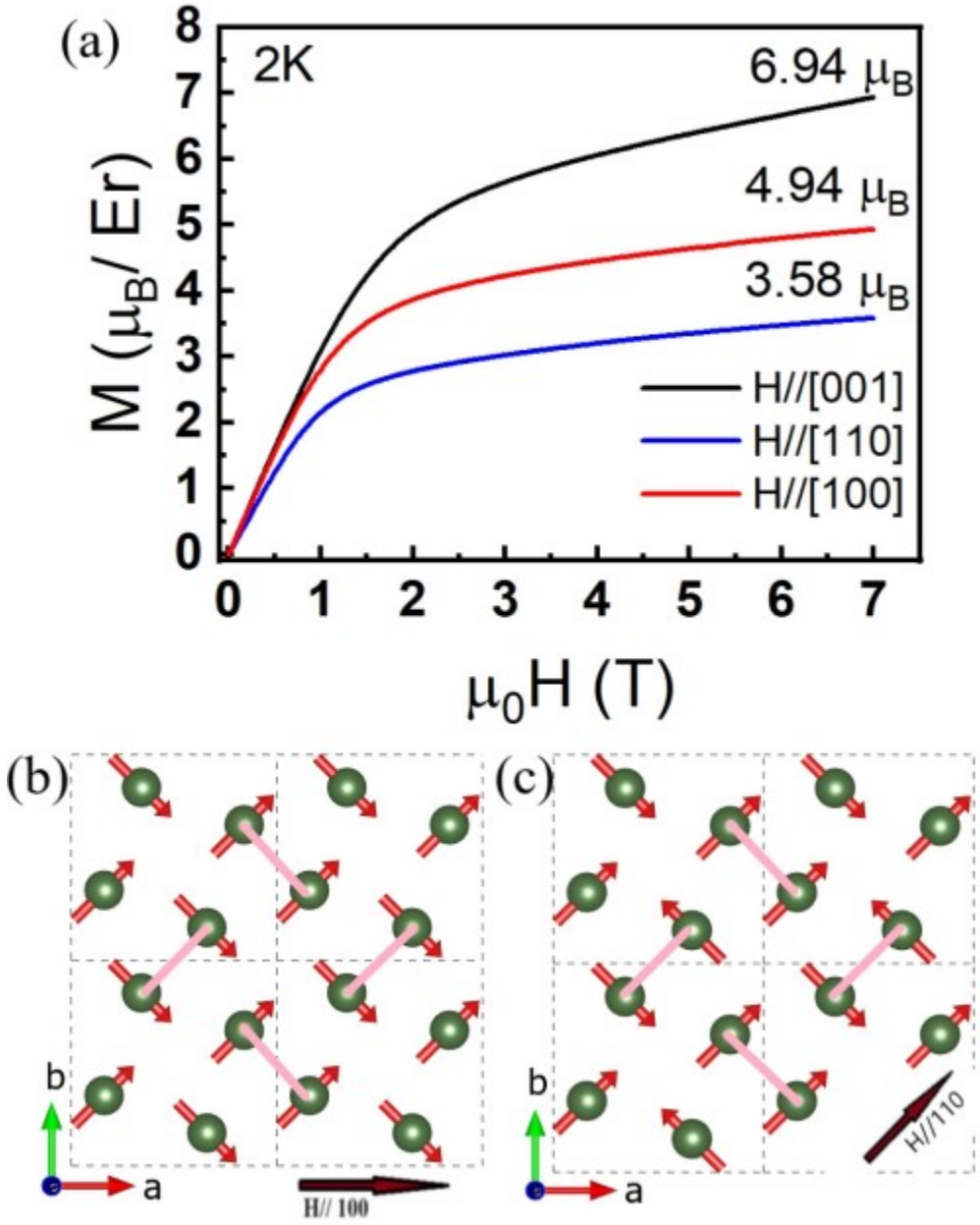

Figure 3.12: (a) DC magnetization (M) vs field (H) for the three high-symmetry directions $H \parallel [001]$, $H \parallel [100]$, and $H \parallel [110]$. The magnetization values at 7 T are provided in the panel. (b) Predicted field-polarized spin structure for $H \parallel [100]$. The moments are confined to the ab-plane and make a 45° angle with the local [100] axis. (c) Predicted field-polarized spin structure for $H \parallel [110]$. Due to in-plane anisotropy with a strong tendency for the moments to point along local [110] directions, only one sublattice is polarized while the other one is essentially unresponsive.

The main results of the neutron diffraction experiment are shown in Fig 3.13. While we identified $\vec{k} = 0$ and $\vec{k} = (0,0,0.5)$ Bragg peaks in these measurements, no peaks indicative of additional magnetic propagation vectors were found at any applied field. Here, we present the field-evolution of the (3,1,0) and (3,1,0.5) Bragg peak integrated intensities at a fixed temperature of 0.28 K. There are three different field regimes. For the lowest fields, both the (3,1,0) and (3,1,0.5) integrated intensities are roughly constant. For intermediate fields, the (3,1,0.5) peak and the (3,1,0) peak intensities show a large decrease and increase respectively. For the highest fields, the (3,1,0.5) peak intensity is completely suppressed while the (3,1,0) peak shows another modest intensity increase. The field-evolution of the (3,1,0) peak tracks the 0.4 K magnetization data well, which shows that it is an effective probe of the net moment along the c-axis.

These results indicate that one of the intermediate phases corresponds to a $2\vec{k}$-structure, with the in-plane and out-of-plane moment components giving rise to the $\vec{k} = (0,0,0.5)$ and $\vec{k} = 0$ magnetic propagation vectors respectively. The onset of the polarized phase corresponds to the disappearance of the (3,1,0.5) peak and hence the complete suppression of the in-plane moment component. There appears to be a weak energy barrier that must be overcome by the magnetic field to reach the $2\vec{k}$-state since the (3,1,0.5) peak intensity does not decrease immediately after the field is applied. This behavior provides further evidence that the Er moments in this system have quasi-XY rather than true XY magnetic anisotropy. Finally, we note that there is no evidence for the second intermediate-field phase in this data, which may be due to the elevated base temperature as compared to the AC susceptibility measurement.

3.5 Summary

We investigated the structural and magnetic properties of both polycrystalline and single crystal samples of the Shastry-Sutherland lattice system $Er_2Be_2SiO_7$ using a variety of bulk characterization and scattering techniques.

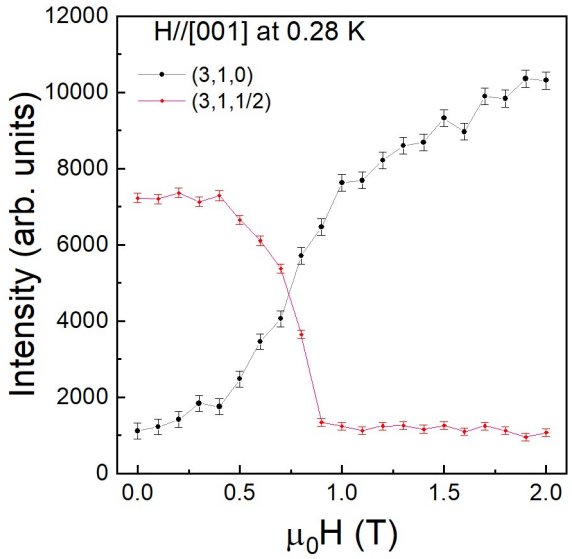

Figure 3.13: Field-dependence of the integrated intensity for the (3,1,0) and (3,1,0.5) Bragg peaks. While the (3,1,0.5) integrated intensity drops sharply between 0.4 and 1 T, the (3,1,0) integrated intensity tracks the field-dependence of the DC magnetization at comparable temperatures quite well.

This material crystallizes in the tetragonal P-42_1m space group (113) over a wide temperature range from 0.28 K to 300 K. The Er moments have a quasi-XY magnetic anisotropy with a small preference to lie along the normal to their local mirror plane, which corresponds to the crystallographic [110] or [1-10] direction for the two orthogonal dimer sublattices. Inelastic neutron scattering data shows that the $J_{\text{eff}} = 1/2$ model is not appropriate for this system due to a low-lying crystal field level and it was also used to establish some probable crystal field parameters for this material.

Fig 3.14 summarizes the bulk characterization results for the three high-symmetry directions. These H-T phase diagrams were constructed from a combination of the heat capacity data (λ anomaly temperature), the real part of the AC susceptibility (peak fields), and dM/dH (peak fields). As described above, the phase diagrams for the two in-plane field directions are nearly indistinguishable and consist of a single metamagnetic transition from the low-field Γ_1 antiferromagnetic ground state to a field-polarized phase. The phase diagram for $H \parallel [001]$ is more complex, as we have identified two intermediate field-induced states.

$Er_2Be_2SiO_7$ exhibits long-range non-collinear magnetic order below $T_N = 0.841$ K. The Shastry-Sutherland planes of the Γ_1 structure consist of antiferromagnetic dimers with in-plane moments perpendicular to the dimer bonds and square plaquettes with two moments pointing in and two moments pointing out of them. A modest in-plane magnetic field ~ 0.4 T induces a magnetic transition from the Γ_1 magnetic structure to a field-polarized phase. An $H \parallel [001]$ field generates a more complicated H-T phase diagram with at least two intermediate field states between the Γ_1 and field-polarized phases. One intermediate phase has a $2\vec{k}$ magnetic structure corresponding to a gradual canting of the moments towards the c-axis with increasing field, while the nature of the second intermediate phase remains unknown. The microscopic origins of the field-induced phases elucidated here are consistent with expectations for the behavior of classical, anisotropic moments.

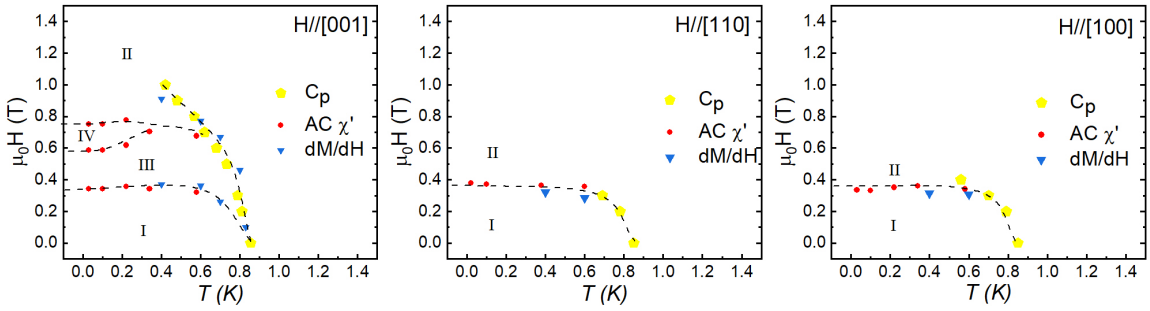

Figure 3.14: *H-T* phase diagrams for $Er_2Be_2SiO_7$ with $H \parallel [001]$, $H \parallel [110]$, and $H \parallel [100]$. Dashed lines are drawn as guides to the eye. The in-plane field behavior is quite simple and only consists of phase I and phase II, which correspond to the Γ_1 magnetic structure and the field-polarized state. There are two additional phases for $H \parallel [001]$ found at intermediate field ranges between phase I and II. Single crystal neutron diffraction suggests that phase III is a $2\vec{k}$ magnetic structure corresponding to a field-induced canting of the moments towards the *c*-axis, while the nature of phase IV remains unknown.

Chapter 4

Magnetic Properties of $Dy_2Be_2SiO_7$

This chapter is dedicated to the investigation of the magnetic properties of the Shastry-Sutherland lattice magnet $Dy_2Be_2SiO_7$. The strong spin-orbit coupling of the Dy^{3+} ions in this compound produces highly anisotropic magnetic moments. In this case the [001]-axis appears to be a quasi-hard axis. The integrated entropy extracted from temperature dependent heat capacity measurements approaches Rln(2) indicating that the moments are effective spin 1/2. For fields applied along the [001]-axis a striking series of four magnetization plateaus, including a zero-field plateau, are observed prior to saturation.

After confirming the atomic structure via powder and single crystal XRD, small single crystal samples are oriented using the laue back diffraction method. The oriented samples were first investigated with magnetization and heat capacity measurements. A sharp magnetic phase transition consistent with antiferromagnetic order is observed in heat capacity measurements at $T_N = 1.18$ K. The integrated entropy falls just short of Rln(2) and is consistent effective spin 1/2 moments.

For fields applied along the in-plane directions [100] and [110] only a single magnetic phase transition from the zero-field state to a field polarized state is observed. In both directions this phase transition occurs at approximately 0.25 T at 0.4 K. When field is applied along the [001]-axis several magnetization plateaus

are observed. Plateaus are observed 0,1/7,4/9,2/3, and 1/1 fractions of the saturation magnetization.

Analysis of powder neutron diffraction data collected on HB-2A at ORNL reveals a zero-field spin structure, with a propagation vector of k =[0,0,1/2],consisting of antiferromagnetically coupled layers of moments principally oriented in the ab-plane with only a small out of plane component. Neutron scattering experiments to investigate the crystal electric field Hamiltonian were conducted on polycrystalline sample at the ARCS beamline at ORNL. Although we were not able to identify all seven CEF excitations expected of the Kramer's, J = 15/2, Dy^{3+} ion, we are able to identify the first excited level at $\sim$ 8.4 meV.

4.1 Bulk Characterization

4.1.1 Heat Capacity

Fig 4.1 shows the heat capacity as a function of sample temperature in zero field. A broad lambda anomaly indicative of long range antiferromagnetic order is observed with a peak at T_N = $\sim$1.18 K. The lambda anomaly is very sharp and their is real possibility that true peak maximum is not captured by the relaxation heat capacity method. The integrated entropy approaches Rln(2) at 10 K indicating that an effective spin-half, S_{eff} = 1/2, model is appropriate at low temperatures.

4.1.2 DC-Magnetic Susceptibility

Figure 4.2 and 4.3 show the T-dependence of the inverse magnetic susceptibility $1/\chi$ along three high-symmetry crystallographic directions measured from 2 K to 300 K with an applied DC-field of 0.1 T and χ vs T(K) at He3 temperatures in an applied field of 0.05 T, respectively. For the [001] direction $1/\chi$ does not have a linear T-dependence throughout the measured range due to the presence of two CEF excitations at 8.4 meV and 19.6 meV.

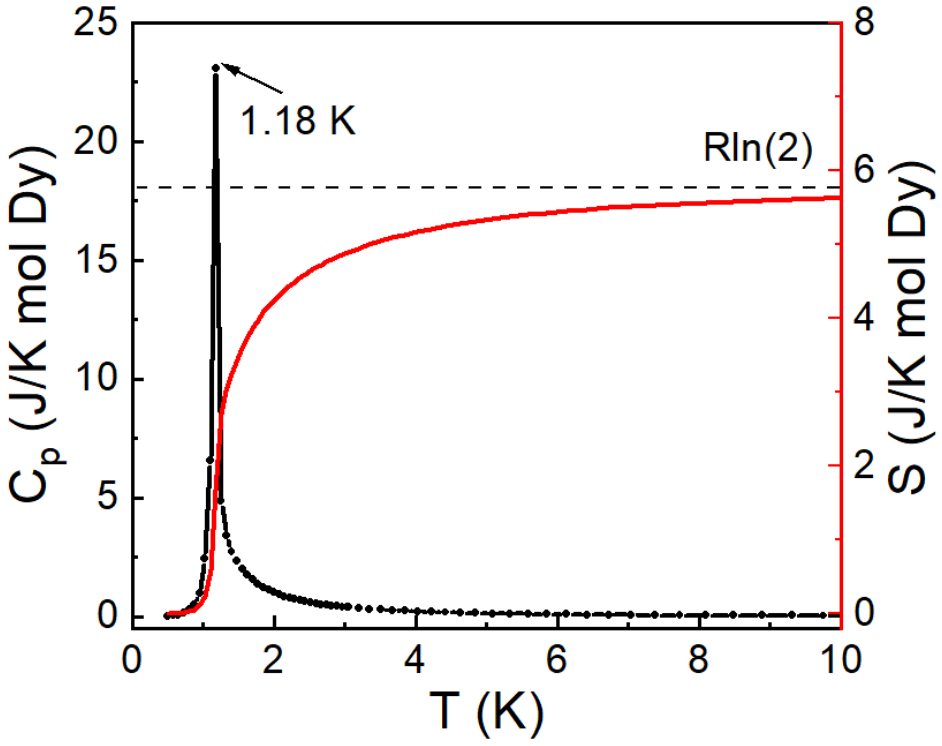

Figure 4.1: Zero-field heat capacity data reveals a sharp Lambda anomaly at 1.18 K. The corresponding magnetic entropy is shown over the same range in red. The entropy almost approaches Rln(2) at 10 K. A non-magnetic analog, $Lu_2Be_2SiO_7$, is used to subtract the phonon contribution to heat capacity above 2 K.

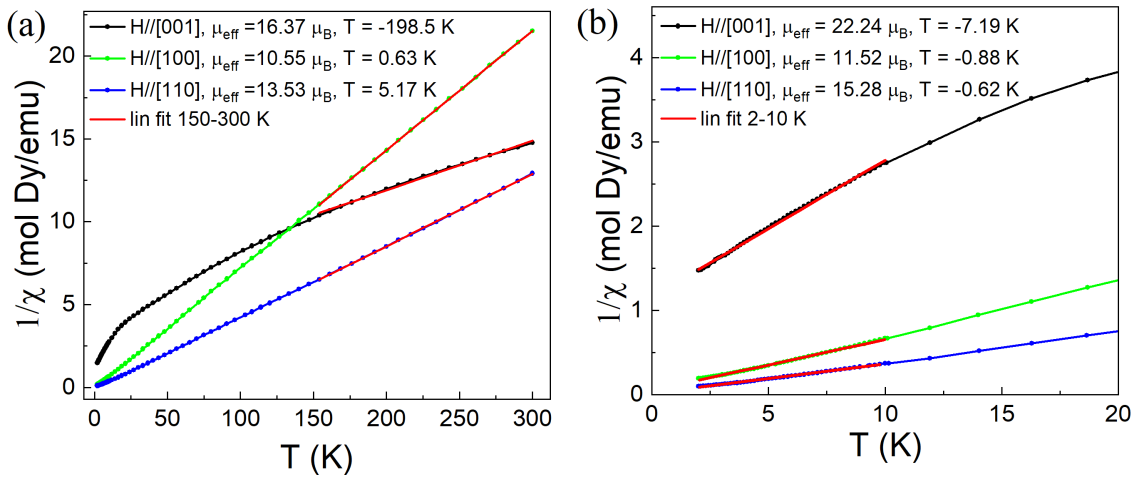

Figure 4.2: $1/\chi$ for $H \parallel [001]$, $H \parallel [110]$, and $H \parallel [100]$ collected at 0.1 T. Linear fits are performed between 150-300 K and 2-10 K. The obtained θ_{cw} and μ_{eff} values are noted in the text.

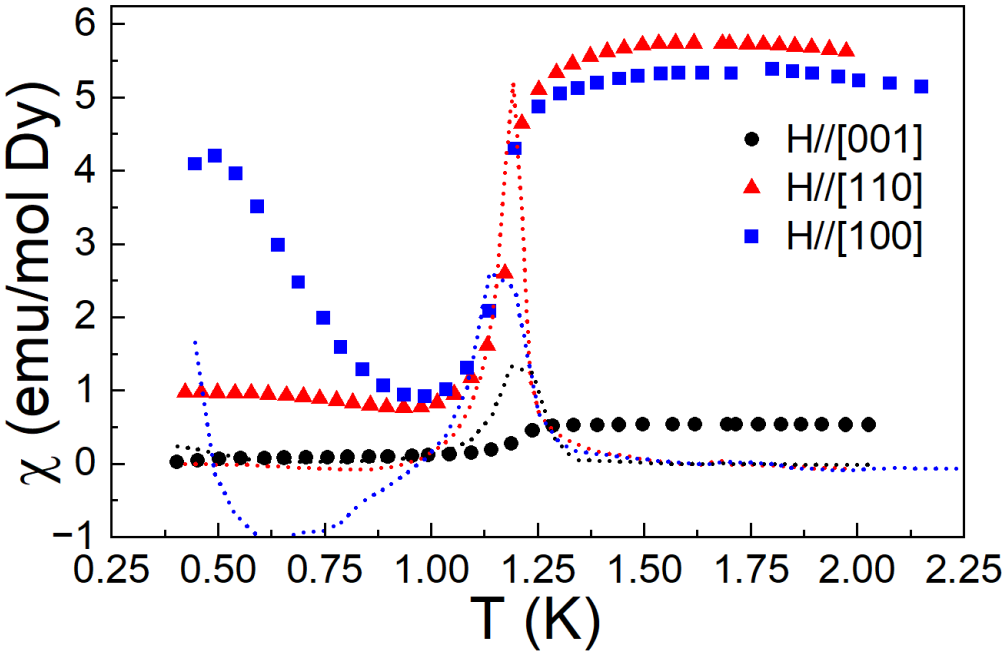

Figure 4.3: The DC susceptibility (χ) and its derivative ($d\chi/dT$) vs T measured at 0.05 T along three high-symmetry crystal-lographic directions. The peaks in ($d\chi/dT$), indicative of the magnetic transition temperature, are visible at 1.21, 1.19, and 1.16 K for applied fields along the [001], [110], and [100] directions respectively.

4.1.3 DC-Magnetization

DC magnetization M vs field H and its derivative is shown at selected temperatures for these three high-symmetry directions in Fig 4.4. The in-plane field dependence of both M and dM/dH appears to be quite simple, with only one abrupt slope change in magnetization data around 0.2-0.3 T corresponding to a large peak in dM/dH. This behavior is indicative of a single metamagnetic transition from the zero-field ground state established above to the field-polarized phase. The $H \parallel [001]$ data on the other hand shows several Magnetization Plateau at zero-field,$\sim$1/7 of M_{sat},$\sim$4/9 of M_{sat},and $\sim$2/3 of M_{sat}. Careful scrutiny of the corresponding susceptibility in Fig 4.4 (d) also show weak signs of an additional plateau like feature centered at $\sim$ 4 T.

4.2 Zero-Field Spin Structure via Neutron Diffraction

Neutron diffraction data was collected on polycrystalline sample at the HB-2A beamline at ORNL, as described in section 2.3.1. Due to the strong neutron absorption of Dy $\sim$3 g of sample was rolled into a cylindrical annulus of thickness 1-2 mm. This thickness is selected to optimize the total neutron transmission through the sample. Data collected at 3 K above T_N is refined with only the nuclear phase and an aluminum background phase. The resulting fit pattern is compared to the measured pattern in Fig 4.5 and agrees with previous powder-XRD and single crystal XRD refinements. No evidence of structural distortions was detected.

The diffraction pattern at 0.3 K is shown in Fig 4.5(b) and clearly shows additional peaks not present in the 3 K data. The position of these peaks was indexed using K-search, a Fulprof application. We find that these additional peaks are well indexed by a [0,0,1/2] propagation vector and that there are five symmetry allowed irreducible representations in Kovalev's notation. The Γ_1 - Γ_4 IRs correspond to spin states with AFM dimers, while the Γ_5 IR has ferromagnetic (FM) dimers.

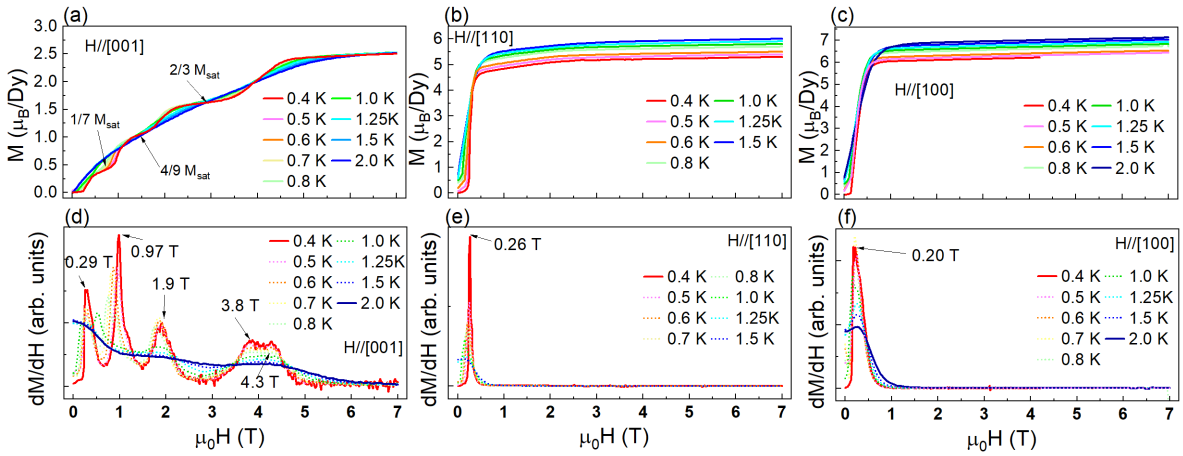

Figure 4.4: (a-c) Magnetization vs Field and its derivative along three high symmetry directions [001], [110], [100]. For fields along [001] three distinct magnetization plateau are visible.

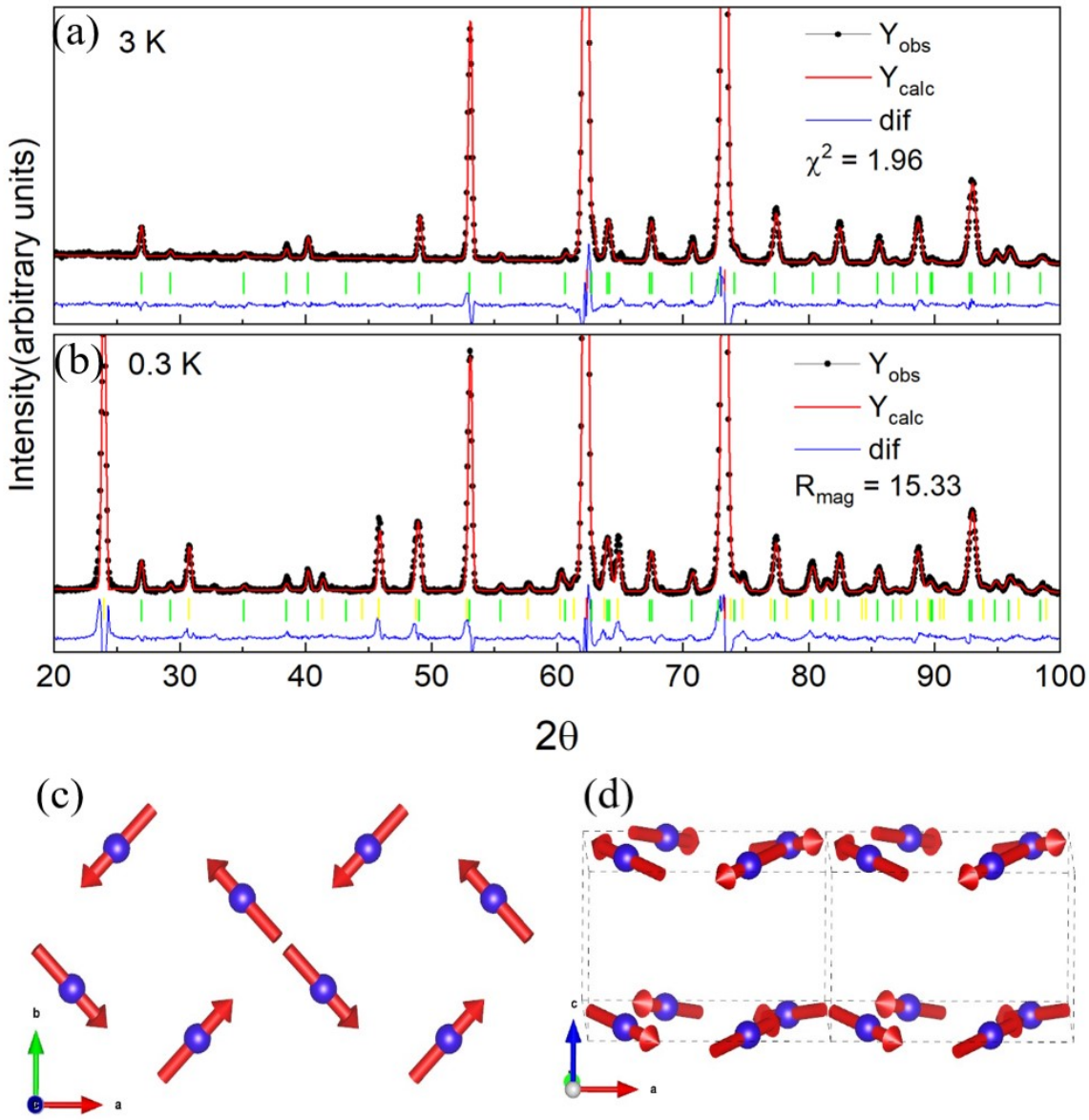

Figure 4.5: (a) The neutron powder diffraction pattern collected at 3 K (above TN). The best Rietveld refinement result is superimposed on the data. The nuclear Bragg peaks from the sample and the background are indicated by green and red ticks respectively and the difference curve is shown below the Bragg peaks. (b) The neutron powder diffraction pattern collected at 0.3 K (below TN). The best Rietveld refinement result, which now includes a magnetic phase, is again superimposed on the data. The magnetic Bragg peaks are denoted by the yellow ticks. (c) The Spin configuration of the best magnetic structure as seen along the [001] and (d) [010] directions. This phase corresponds to irreducable representation Γ_4 with a [0,0,1/2] propogation vector. All ions have the same moment of 8.38 μ_B.

The best matching spin structure corresponds to IR Γ_4 which consists of moments primarily in the ab-plane but with an allowed out of plane component. The in-plane component of the magnetic moments in a unit cell form a loop with a definite handedness while the out of plane component couples antiferromagnetically between planes as shown in fig 4.5 (c)(d) . All ions in this ordered spin structure have a moment of 8.45(3) μ_B.

4.3 Inelastic Neutron Scattering and the CEF spectrum

To investigate quantitative details of the magnetic anisotropy induced by crystal fields, inelastic neutron scattering (INS) measurements on a polycrystalline sample of $Dy_2Be_2SiO_7$ were conducted using the Wide Angular-Range Chopper Spectrometer ARCS. Datasets were collected with incident energies of 25 meV, 60 meV, and 200 meV at 10 K, Fig 4.6. The goal of this measurement is to determine the crystal field levels associated with the $J = 15/2$ ground state multiplet of Dy^{3+}. Dy^{3+} is a Kramers ion so time reversal symmetry requires that the crystal field ground state must be at least two-fold degenerate. The Dy ions are surrounded by eight oxygen ions that generate a low symmetry monoclinic C_s environment. The low-symmetry of this point group is expected to produce maximal splitting of the 16 levels associated with the $J = 15/2$ ground state multiplet, so up to 7 excited crystal field doublets may be visible in the low-temperature INS data. The separation of the lowest CEF doublet from the ground state is ~ 7.8 meV ensuring that the Dy moments have $S_{eff} = 1/2$ at temperatures near T_N. Although other possible CEF peaks are observed we were not able to identify all seven expected CEF peaks in the data. The analysis of the data is complicated by the presence of several phonon which combined with the low point symmetry of the system, producing a CEF Hamiltonian with 14 terms, makes determining the crystal field parameters infeasible.

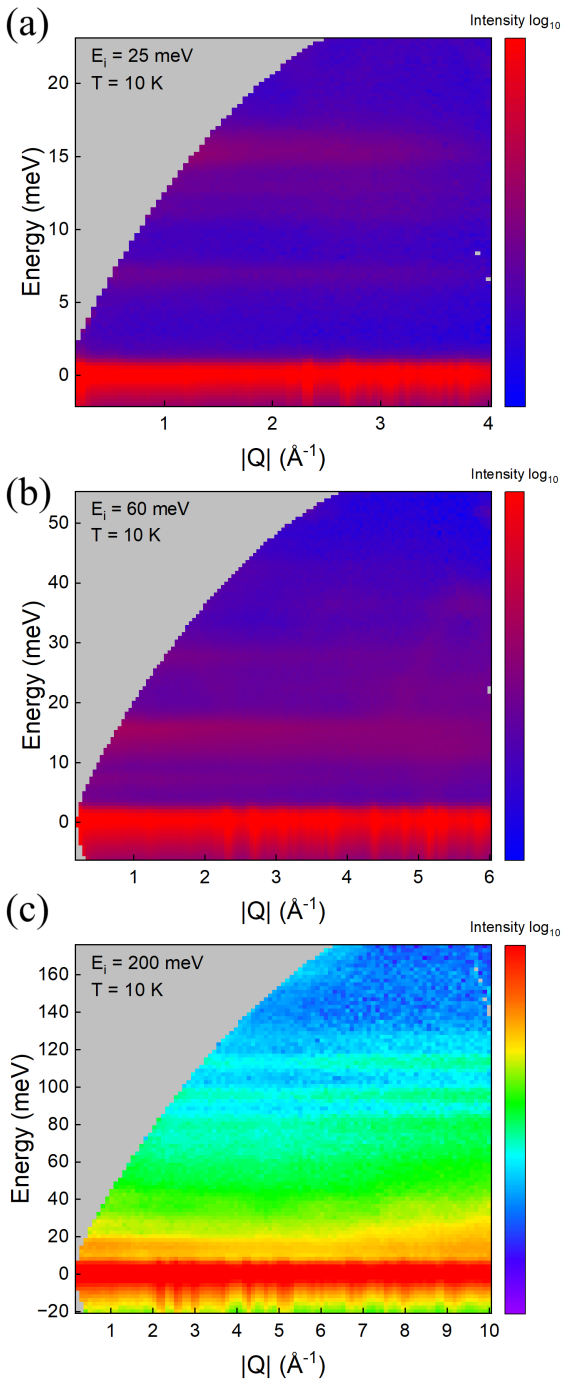

Figure 4.6: Color contour plots of the scattering intensity (in arb. units) as a function of momentum transfer Q and energy transfer E for the following datasets at 10 K: (a) $E_i = 25$ meV, (b) $E_i = 60$ meV, (c) $E_i = 200$ meV. Several crystal field excitations from Dy^{3+} are visible in this data with the lowest at ~ 7.9 meV.

4.4 Summary

We investigated the structural and magnetic properties of both polycrystalline and single crystal samples of the Shastry-Sutherland lattice system $Dy_2Be_2SiO_7$ using a variety of bulk characterization and scattering techniques. The single ion anisotropy is complicated and of the XYZ form with g_{110} (parallel to NN bond) $\geq$ g_{-110} (perpendicular to NN bond) $\geq$ g_{001}. This anisotropy results in a strong tendency for moments to lie in the ab-plane. Although it was not possible to determine all seven CEF levels expected for the J = 15/2 Dy ion the lowest CEF level is identified at 7.9 meV. This result alongside the integrated entropy from heat capacity measurements indicate that an $S_{eff} = 1/2$ model is appropriate. $Dy_2Be_2SiO_7$ exhibits long-range non-collinear antiferromagnetic order below $T_N = 1.18$ K. The magnetic propagation vector of this antiferromagnetic state is $\vec{k} = (0,0,0.5)$.

The spin structure in zero field, shown in fig 4.5 (c), corresponds to IR Γ_4 which has moments oriented in a loop with a definite handedness and only a small out of plane component. The nature and spin structure of the field induced phases remains unknown. However, it is worth noting that the (0,0,0.5) magnetic propagation vector persists only in the first field induced phase up to 1 T and is replaced by a (0,0,0) propagation vector in the two subsequent phases. Fig 4.7 summarizes the bulk characterization results as a phase diagram for field applied along the [001]-axis. The value of the magnetization is represented by color and the symbols correspond to peaks in dM/dH. Four phases corresponding to magnetization plateaus are observed before saturation, with weak evidence for a fifth plateau phase at temperatures below 0.5 K. Further neutron diffraction experiments on single crystal samples under field are needed to determine the spin structure of the field induced plateau phases.

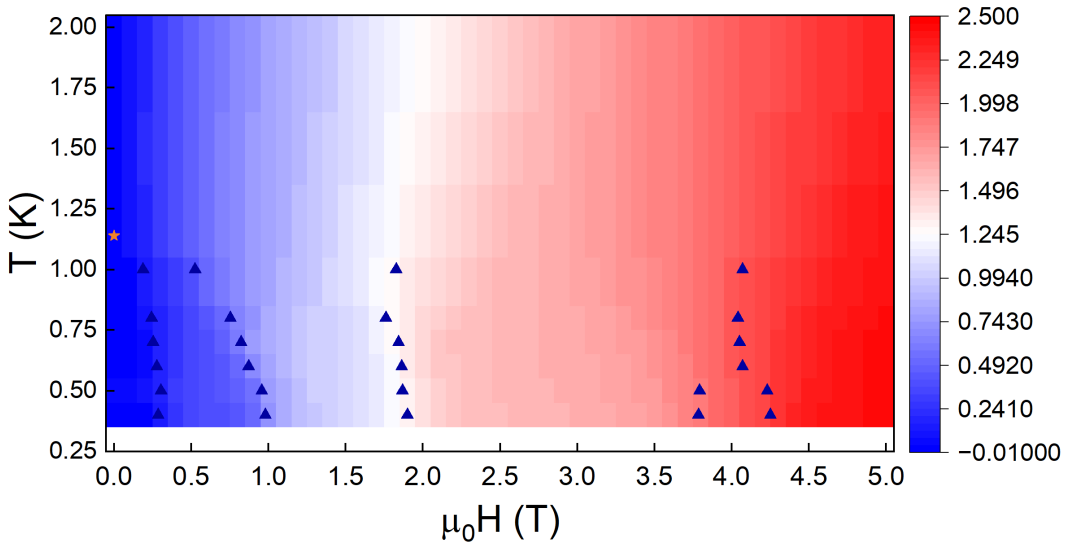

Figure 4.7: The phase diagram for field applied along [001] shows several field induced phases. Constructed from Magnetization data where symbols represent peaks in dM/dH. Color indicates value of Magnetization.

Chapter 5

Magnetic Properties of $Yb_2Be_2SiO_7$

This chapter is dedicated to the investigation of the magnetic properties of the Shastry-Sutherland magnet $Yb_2Be_2SiO_7$. We present bulk characterization, neutron diffraction, and neutron scattering measurements of the SSL material. We find that the Yb^{3+} ions are well described by an effective spin-1/2 model at low temperatures and the system shows no signs of long range magnetic order at temperatures above 50 mK. Neutron scattering and heat capacity measurements indicate that the magnetic ground state is composed of dimers with non-degenerate spin gaps at $\Delta \sim 0.11$ meV and $\Delta \sim 0.19$ meV. Additional neutron scattering experiments reveal the presence of three crystal electric field levels, at energy transfers greater than 10 meV, and investigate the possibility of structural disorder in this material.

SSL magnets with antiferromagnetic intradimer and interdimer Heisenberg exchange are predicted to host the antisymmetric singlet, $S = 0$ and $S_z = 0$, ground state when the intradimer exchange is dominant [43, 37]. Until recently there has only been one experimental realization of this ground state in the celebrated SSL compound $SrCu_2(BO_3)_2$ [35, 36]. Rare-earth-based SSL systems with strong spin-orbit coupling offer the possibility of introducing anisotropic intradimer and interdimer exchange interactions and realizing magnetic ground states not possible in the Heisenberg case. This appears to be the case for $Yb_2Be_2SiO_7$, analysis of magnetization, heat capacity,

and neutron spectroscopy data using a model of isolated dimers with anisotropic XYZ exchange interactions suggest a novel dimer ground state with the symmetric wavefunction $(\uparrow\uparrow - \downarrow\downarrow)/\sqrt{2}$.

Although not observed in heat capacity data two additional low energy excitations at $\Delta \sim 0.7$ meV and $\Delta \sim 1.2$ meV are observed in neutron scattering data. Intriguingly, these excitations have a very different Q-dependence from the excitations at 0.11 meV and 0.19 meV. The Q-dependence of the excitations at 0.7 meV and 1.2 meV match the expected Q-dependence for dimers with Heisenberg like exchange. The presence of two distinct sets of dimer like excitations with different characters indicates there may be a small degree of structural distortion or site mixing in the sample.

5.1 Bulk Characterization

The fractional atomic positions and lattice parameters determined via single crystal XRD are given in Table 5.1. The single crystal results agree well with previous XRD results collected on polycrystalline sample.

5.1.1 Heat Capacity

Fig 5.1 shows the heat capacity as a function of sample temperature in zero field. A broad Schottky anomaly consistent with energy transfers of 0.11 meV and 0.19 meV centered at a temperature of ∼0.5 K. The integrated entropy approaches Rln(2) at 4 K indicating that an effective spin-half, $S_{eff} = 1/2$, model is appropriate at low temperatures. The field dependent heat capacity with fields along [001] and [110] is shown in fig 5.2 as open symbols. The simulated results from our best model are also shown and will be discussed in greater detail in this chapter. The broad peak in heat capacity is pushed to higher temperatures with the application of magnetic field. The degree to which the peak shifts with field depends on the component of the

Table 5.1: Atomic coordinates and isotropic displacement parameters U_{eq} (Å^2) from single-crystal XRD

Space Group: Tetraganol, P-42_1m, No. 113					
Unit Cell: $a = b =$ 7.207(2) Å and $c =$ 4.719(2) Å					
Atom	Wyck.	x	y	z	U_{eq}
Yb	4e	0.1589(1)	0.6589(1)	0.50772(1)	0.0040(1)
Be	4e	0.637(1)	0.137(1)	0.960(2)	0.006(2)
Si	2a	0	0	0	0.0033(4)
O_1	2c	0	1/2	0.185(2)	0.005(1)
O_2	4e	0.6423(6)	0.1423(6)	0.295(1)	0.005(1)
O_3	8f	0.0824(7)	0.1624(6)	0.203(1)	0.0058(8)

anisotropic g-tensor for the crystallographic direction the field is applied in. The shift in temperature per unit of applied field is much greater along the [001]-axis than for the [110]-axis. This suggests that the component of the g-tensor for the lowest lying CEF doublet along [001] is significantly greater than the g-tensor component along [110].

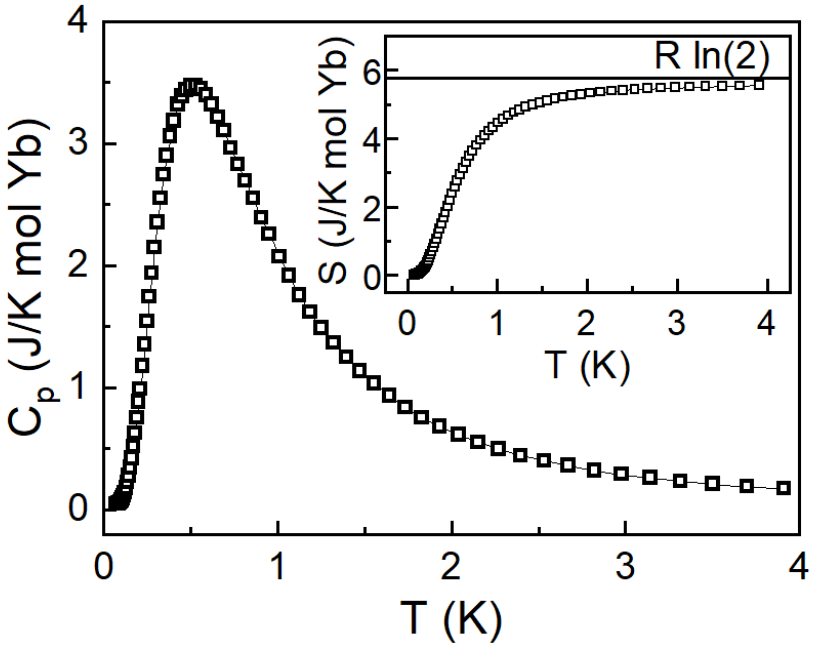

Figure 5.1: Zero-field heat capacity data reveals a broad Schottky anomaly centered near 0.5 K. The inset shows the magnetic entropy over the same temperature range, which approaches $Rln(2)$ at 4 K.

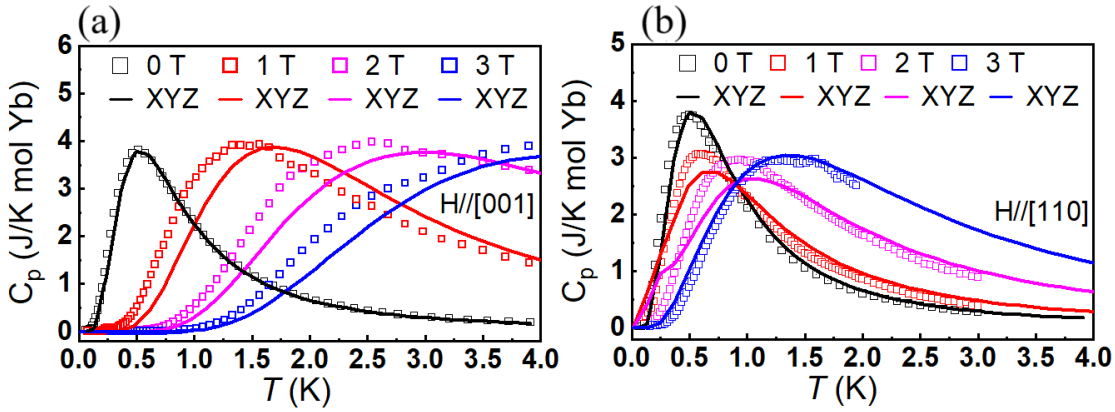

Figure 5.2: Heat capacity vs magnetic field applied along the [001] and [110] crystal directions. Experimental data are shown as open symbols while simulated data from our XYZ anisotropic intra-dimer exchange model are shown as solid curves.

5.1.2 Magnetization

Fig 5.3 shows the Magnetization as a function of applied field at both 2 K and 0.4 K. The components of the ground state g-tensor parallel to crystallographic [001] and [110] are estimated from the value of the Magnetization in the saturated state as $g^A_{-110} = 1.64\ \mu_B$, $g^A_{110} = 1.71\ \mu_B$, and $g^A_{001} = 4.6\ \mu_B$. These estimated g-tensor values serve as key inputs in our isolated dimer simulations where there values are fixed.

At 2 K for both the [001] and [110] directions the Magnetization is seen to increase smoothly until saturation with no evidence for transitions. At 0.4 K the Magnetization curve along [001] remains smooth and continuous but for fields along [110] a weak peak in susceptibility appears at ~ 1.4 T. The origin of this peak requires further investigation but may be explained by a level crossing between two dimer wavefunctions whose associated energy levels are influence by the applied field.

5.2 Neutron Diffraction in Zero-Field

Unpolarized neutron powder diffraction (NPD) patterns collected at 0.25 K and 2 K on the HB-2A beamline at ORNL are presented in Fig 5.4 (c) and (d) respectively. Both patterns are well-described by nuclear Bragg peaks associated with the $Yb_2Be_2SiO_7$ crystal structure and the Al sample can. The expected positions of these peaks are indicated by the green and red ticks respectively. While Rietveld refinements of the data using FULLPROF reveal no evidence for oxygen off-stoichiometry in this sample, they do identify $\sim$4.4% Be/Si site mixing. Most importantly, there are no additional Bragg peaks or enhanced peak intensities that can be attributed to long-range magnetic order in $Yb_2Be_2SiO_7$, even down to 0.25 K. The results of the 0.25 K refinement are given in Table 5.2. The arrangement of Yb ions forming an SSL lattice and the atomic structure of $Yb_2Be_2SiO_7$ are shown in Fig 5.4 (a) and (b) respectively.

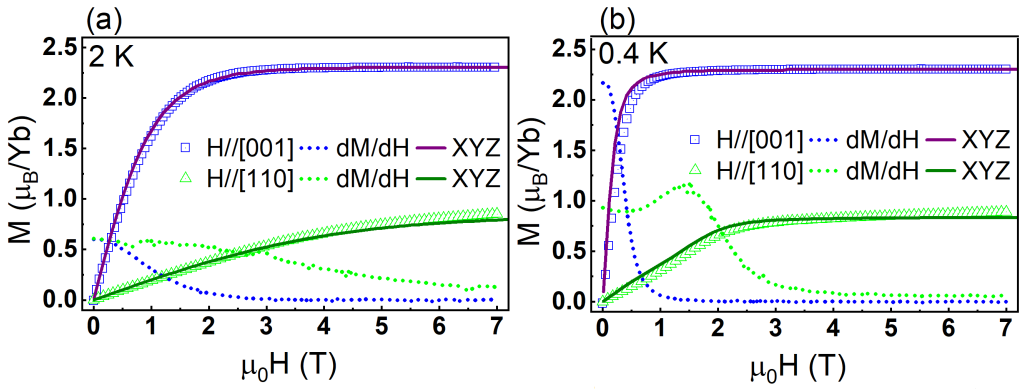

Figure 5.3: (a) Magnetization vs field along two high-symmetry crystallographic directions at 2 K. (b) Similar data collected at 0.4 K.

Table 5.2: Fractional coordinates for $Yb_2Be_2SiO_7$ from neutron powder diffraction at 0.25 K

Atom	Wyck.	x	y	z
Yb	4e	0.1590(3)	0.6590(3)	0.506(1)
Be	4e	0.6387(4)	0.1387(4)	0.955(1)
Si	2a	0	0	0
O_1	2c	0	1/2	0.181(2)
O_2	4e	0.6405(6)	0.1405(6)	0.303(1)
O_3	8f	0.0846(5)	0.1658(6)	0.201(1)

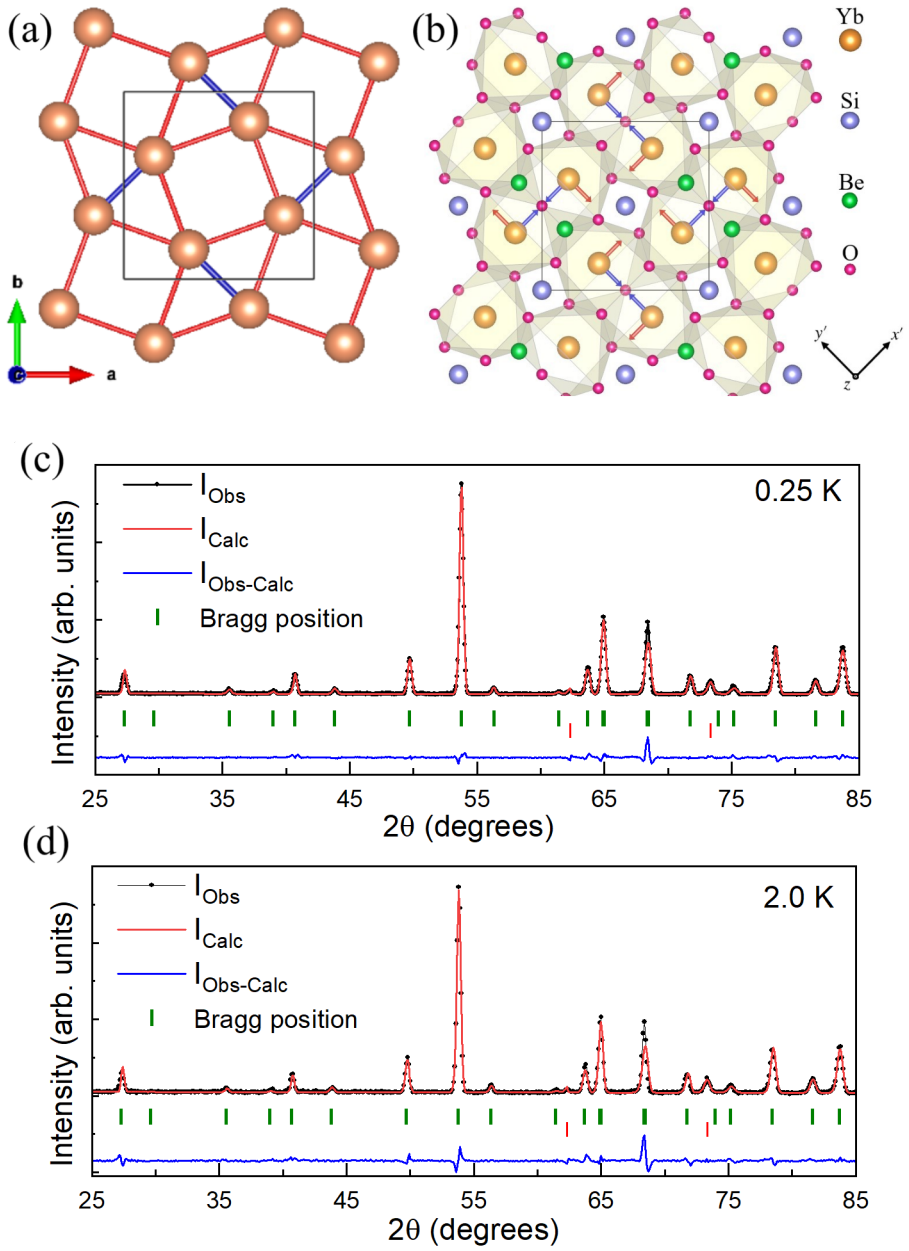

Figure 5.4: (a) The arrangement of Yb^{3+} ions in $Yb_2Be_2SiO_7$ forming a SSL as viewed along the crystallographic [001]-axis. The intradimer and interdimer bonds J_1 and J_2 are shown in blue and red respectively. (b) The full crystal structure of $Yb_2Be_2SiO_7$ viewed along the same axis. The four Yb^{3+} ions in the chemical unit cell have diagonal g-tensors with different local axes, as explained in the main text. (c-d) Neutron powder diffraction patterns collected at 0.25 K and 2 K, respectively. Multi-phase Rietveld refinements with the known $Yb_2Be_2SiO_7$ crystal structure (green ticks) and Al from the sample can (red ticks) explain the data well. No additional peaks associated with long-range order are observed.

5.3 Inelastic Neutron Scattering and low energy excitations

Neutron spectroscopy data collected at the SEQUOIA beamline at ORNL is used to analyze the crystal electric field spectrum in $Yb_2Be_2SiO_7$. The magnetic scattering contribution was isolated by subtracting the scattering from the non-magnetic analog $Lu_2Be_2SiO_7$ measured under the same experimental conditions and scaled appropriately to account for the scattering cross-section difference between Yb and Lu. There is no evidence for low-lying crystal field levels in this data. Instead, there are three excitations centered about 11, 23, and 36 meV as shown in Fig 5.5, whose intensities decrease with increasing Q, that likely correspond to the three excited crystal field doublets expected for $J = 7/2$ Kramer's Yb^{3+} ions in a low-symmetry ligand environment.

Interestingly, these three excitations are much broader than the instrument energy resolution, which is readily apparent when comparing this data to previous results from $Er_2Be_2SiO_7$. This broadening may be a consequence of the Be/Si site mixing that we identified in the Rietveld refinements of the HB-2A data. Interestingly, we confirmed that there is no evidence for Be/Si site mixing in the previously reported HB-2A data for $Er_2Be_2SiO_7$. We also collected Pair-Distribution-Function (PDF) data using the time-of-flight diffractometer NOMAD to investigate possible local structural distortions in $Yb_2Be_2SiO_7$ but the PDF data, shown in Fig 5.6 is explained well by the global structure. Due to the low point symmetry of the Yb^{3+} ions and the lack of sufficient crystal field observables in the neutron spectroscopy data, it is not feasible to obtain a unique set of crystal field parameters for $Yb_2Be_2SiO_7$.

Neutron spectroscopy data collected at SEQUOIA with an incident energy of 10 meV , not shown, revealed the existence of two low energy excitations at $\sim$0.7 meV and $\sim$1.2 meV.

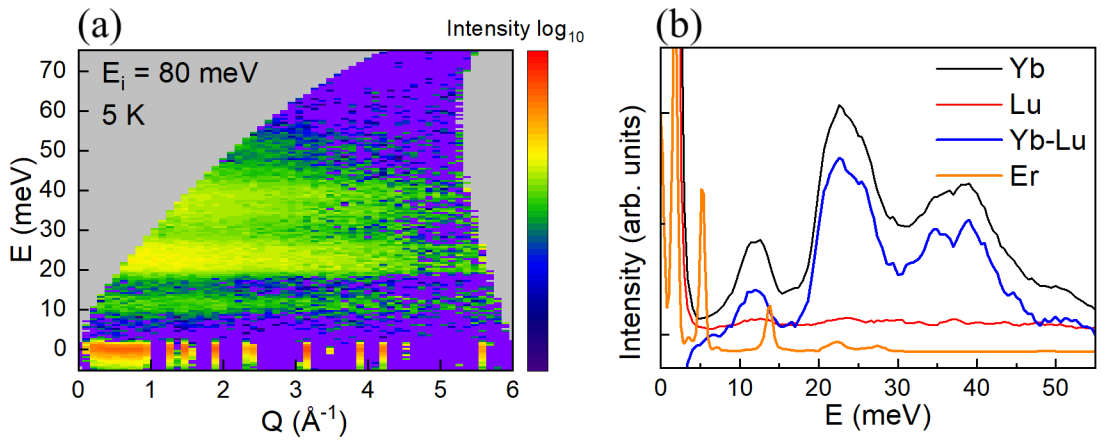

Figure 5.5: (a) Color contour plot of the scattering intensity as a function of momentum and energy transfer at 5 K from SEQUOIA with $E_i = 80$ meV. (c) Constant-Q cuts (Q integration range $[0.25, 2]$ Å^{-1}) of the same $Yb_2Be_2SiO_7$ data and the equivalent data for $Er_2Be_2SiO_7$ and the non-magnetic analog $Lu_2Be_2SiO_7$. The difference curve obtained by scaling the Lu data to account for the variation in the Yb and Lu neutron scattering cross-sections is also shown.

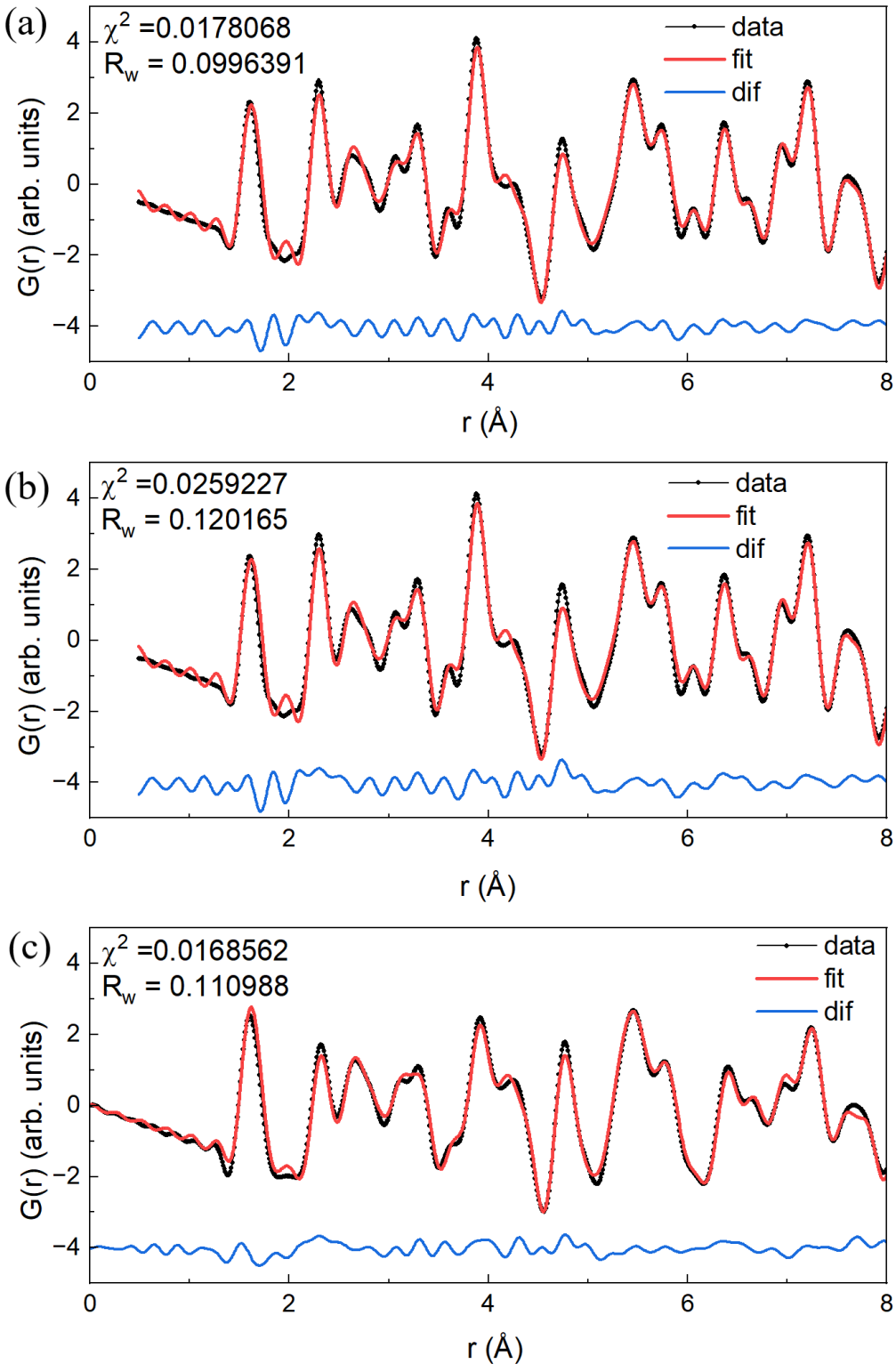

Figure 5.6: The pair distribution function $G(r)$ vs distance for (a) polycrystalline $Yb_2Be_2SiO_7$, (b) crushed single crystal $Yb_2Be_2SiO_7$, and (c) polycrystalline $Er_2Be_2SiO_7$. The data are described well by the known crystal structures for these materials, so there is no evidence for local structure distortions

To investigate the nature of these two low energy excitations neutron spectroscopy data were collected at the CNCS beamline at ONRL at several temperatures between 0.25 K and 100 K. A graph of intensity vs energy transfer (E_i) collected at 0.25 K and integrated between 0.3 and 1.8 Q is shown in Fig 5.7 (a). In this data three excitations centered at ∼0.11 meV, ∼0.19 meV, and ∼ 0.7 meV are identified. It is noted that both the excitation at ∼ 0.7 meV and at ∼ 1.2 meV (not shown) have intensities roughly fifty times weaker than that of the ∼ 0.11 meV excitation. This would be reasonable if they were due to a minority Yb ions hosting different local environments and Hamiltonians. The contribution of each identified peak and the background to the overall pattern is shown in Fig 5.7 (b) and the extracted peak parameters are given in Table 5.3.

Similar intensity vs energy transfer (E_i) data collected at several temperatures is shown in Fig 5.8. The three observed excitations begin to reduce in intensity with increasing temperature above 5 K. Remarkably, the excitations are present at temperatures up to 50 K. The reduction in intensity with increasing temperature provides further evidence that these excitations are magnetic in origin.

Time-of-flight neutron powder diffraction data collected at 100 K using the NOMAD beam line at ORNL on three samples: polycrystalline $Yb_2Be_2SiO_7$, finely ground single crystals of $Yb_2Be_2SiO_7$, and polycrystalline $Er_2Be_2SiO_7$. The goal of this experiment was to identify evidence for local structural distortions that could be responsible for the Yb^{3+} crystal field broadening observed in the SEQUOIA and HB2A data. The NOMAD data reduction was completed with the Advanced Diffraction Environment (ADDIE) suite .

Pair Distribution Function (PDF) refinements were completed using the software package PDFGUI with a maximum Q value of 30 $Å^{-1}$. The pair distribution function, $G(r)$, as a function of distance, r(Å), is shown for the three samples in Fig 5.6. In conflict with HB2A data, all three PDF patterns are well-explained by the known crystal structure of these materials with no clear evidence for significant deviations that would arise from local structure distortions.

Table 5.3: CNCS data fitting results at 0.25 K with E_i = 1.55 meV using a four Gaussian peak model

Peak center	Peak width(FWHM)	Peak Amplitude
-0.0019(2)	0.0390(3)	1
0.111(2)	0.088(4)	0.25(3)
0.19(4)	0.14(5)	0.04(3)
0.692(8)	0.10(2)	0.006(2)

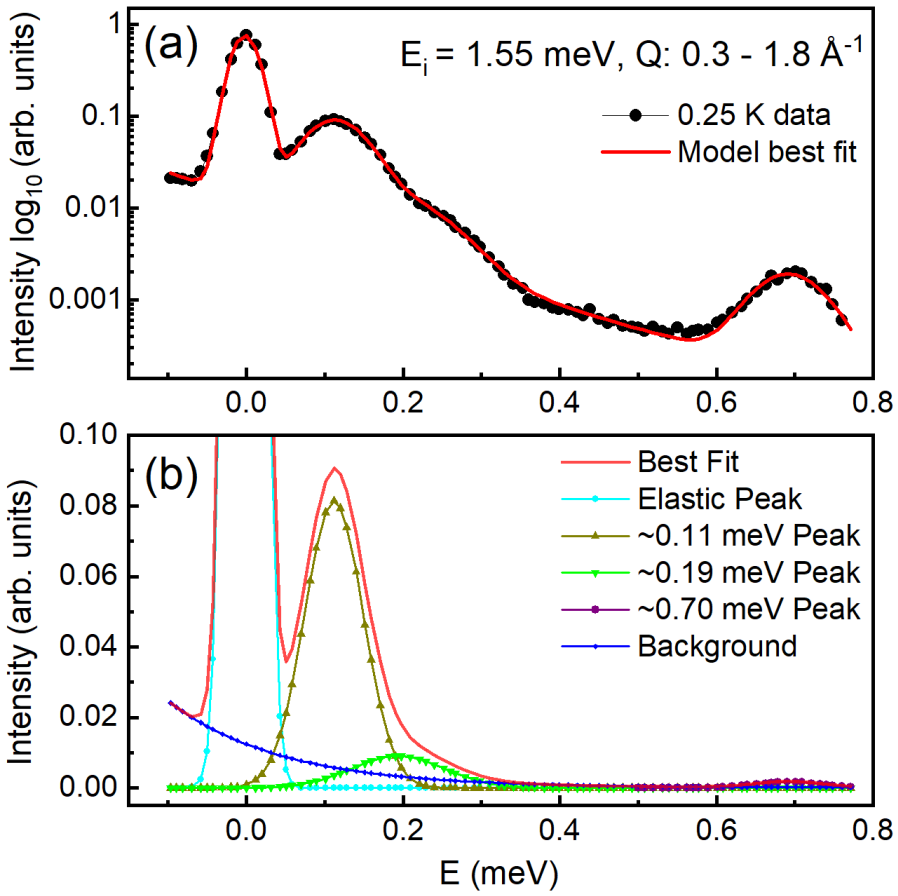

Figure 5.7: (a) Constant-Q cut of CNCS data (Q-integration range [0.3, 1.8] Å^{-1}) with $E_i = 1.55$ meV and $T = 0.25$ K. The best fitting result using a function with four Gaussian peaks, a decaying exponential term, and a constant is superimposed on the data. (b) The contribution of each Gaussian peak to the final fit result. The extracted peak parameters are given in table 6.3

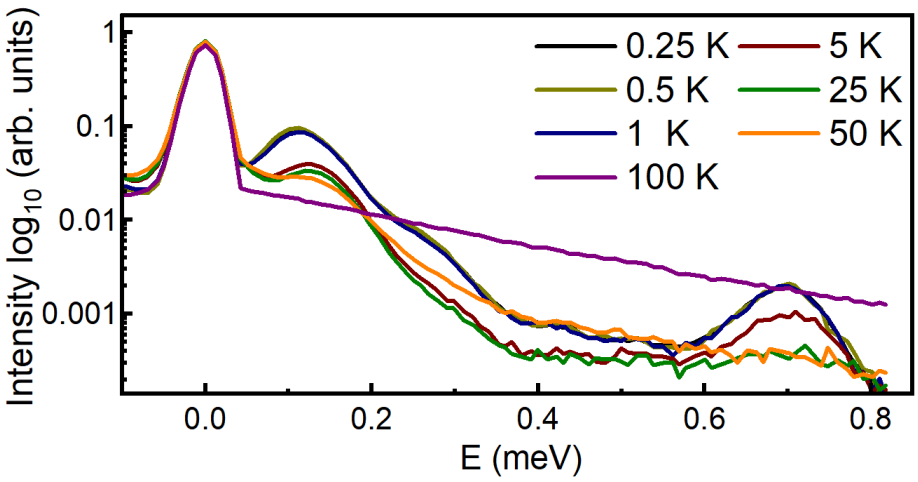

Figure 5.8: Constant-Q cut of CNCS data (Q-integration range [0.3, 1.8] Å^{-1}) with $E_i = 1.55$ meV at several temperatures between 0.25 K and 100 K.

It is also worth noting that the PDF patterns for polycrystalline and crushed single crystal $Yb_2Be_2SiO_7$ are nearly identical.

5.4 Neutron Diffraction with Polarized Neutrons

The magnetic susceptibility χ is a measure of the magnetization of a material in an applied magnetic field. In most crystalline materials, the influence of spin-orbit coupling induces anisotropy that results in χ taking the form of a second-rank tensor rather than a scalar quantity. The components of this tensor can be determined by the half-polarized neutron powder diffraction (pNPD) technique in the linear M/H regime and they provide insight into the local anisotropy of the magnetic ion. The atomic site symmetry is used to establish appropriate constraints for χ. Spin-up and spin-down neutron diffraction patterns with intensities of I^+ and I^- are measured separately, and then Rietveld refinements of the sum and difference patterns (given by $I^+ + I^-$ and I^+ - I^- respectively) are performed using the software CrysPy [92].

The results of these Rietveld refinements for the $Yb_2Be_2SiO_7$ HB-2A data collected at 5 K and 1.5 T are shown in Fig 5.9. The local site susceptibility tensor extracted from this analysis is given by:

$$\hat{\chi}_{ij} = \frac{\vec{M}_i}{\vec{H}_j} = \begin{pmatrix} -0.12(3) & -0.02(2) & 0.05(4) \\ -0.02(2) & -0.12(3) & 0.05(4) \\ 0.05(4) & 0.05(4) & 2.36(3) \end{pmatrix}$$

The magnetization ellipsoids' principal axis directions and magnitudes can be obtained from the local site susceptibility tensor. For $Yb_2Be_2SiO_7$, we find that the two principal g-tensor directions not constrained by symmetry are nearly aligned with the crystallographic [001]-axis and the dimer bond direction ([110] and $[1\bar{1}0]$ for the two dimer sublattices).

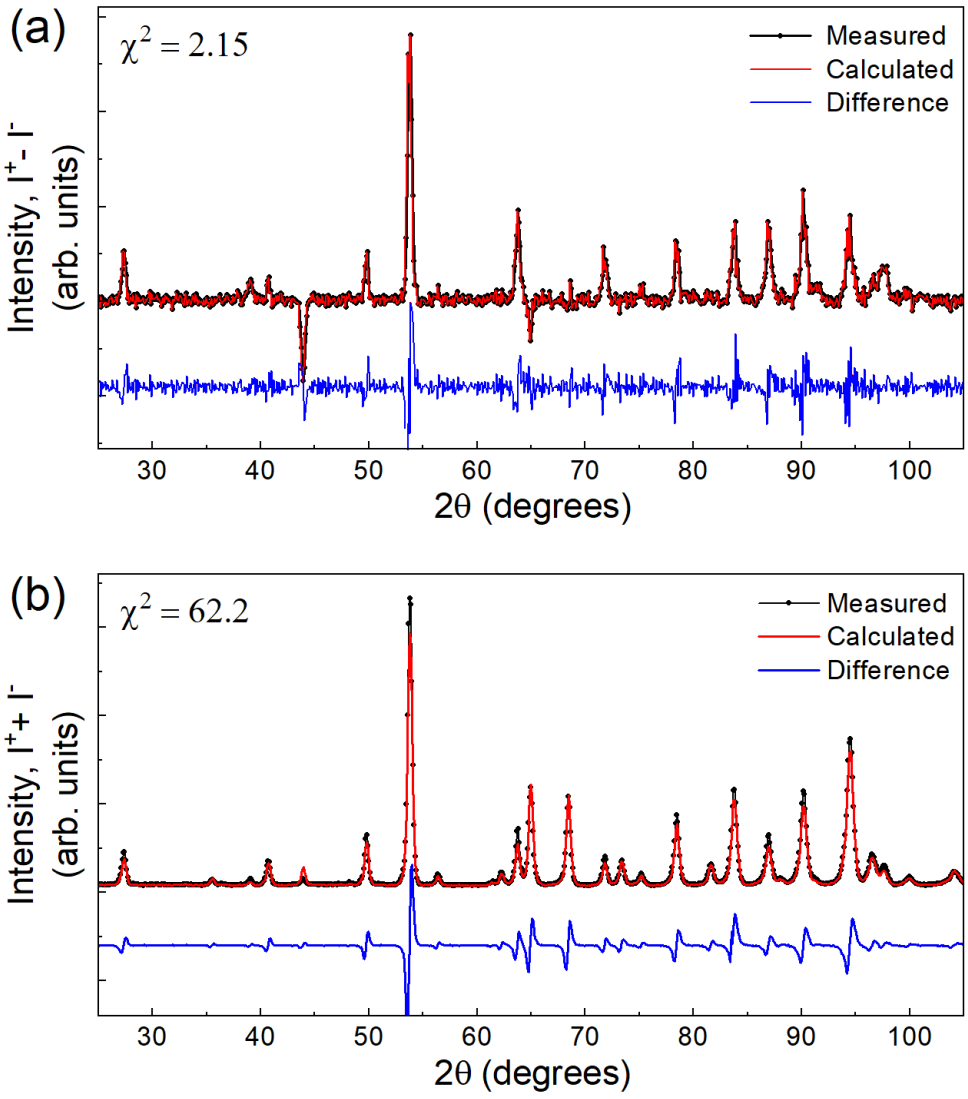

Figure 5.9: (a) The difference pattern, I^+ - I^-, and (b) the sum pattern, $I^+ + I^-$, obtained from the pNPD measurements at 5 K under an applied field of 1.5 T. For each case, the Rietveld refinement is superimposed on the data and the fit residual is shown below it.

The magnitudes of the principal axes are 2.32 μ_B/T, 0.14 μ_B/T, and 0.10 μ_B/T, with the largest value for the pseudo-[001]-axis direction. The magnetization ellipsoids are plotted in Fig 5.10.

5.5 Isolated Dimer Hamiltonian and Simulations

Since effective spin-1/2 dimer models with strong intradimer exchange anisotropy can have a maximum of three single-dimer excitations, it is clear that all four modes (at 0.11, 0.19, 0.7 and 1.2 meV) observed here do not have the same origin. Zero-field heat capacity only depends on the eigenvalues of these models, so we compared our data shown in Fig 5.11 to simulations assuming various energy-level schemes. The best simulation of the zero-field heat capacity data corresponds to an isolated dimer model with a doubly-degenerate mode at 0.11 meV and a non-degenerate mode at 0.19 meV [102, 72]. This implies that the two higher-energy modes have a different origin. In fact their Q-dependence is well-described by the Yb^{3+} magnetic form factor squared multiplied by the known structure factor of a singlet-triplet transition for an isolated Heisenberg dimer model with the square plaquette distance $d = 3.84$ Å. Since these higher-energy modes have a negligible contribution to the specific heat, this implies that only a small fraction of Yb^{3+} ions form longer-range dimers in $Yb_2Be_2SiO_7$, possibly due to the known Be/Si site mixing in this system.

With the energy level scheme for a possible isolated dimer model comprised of most Yb^{3+} ions in the system established, we performed a quantitative analysis of the low-energy neutron spectroscopy data and field-dependent heat capacity and magnetization data. We started by constructing a minimal model based on symmetry analysis [103]. The model Hamiltonian describes a collection of isolated dimers with anisotropic intradimer interactions and Zeeman coupling:

$$\mathcal{H} = \sum_{<i,j>l\alpha} S^{\alpha}_{il} J^{l}_{\alpha\alpha} S^{\alpha}_{jl} - \mu_0 \mu_B \sum_{il\alpha\beta} H^{\alpha} g^{l}_{\alpha\beta} S^{\beta}_{il} \tag{5.1}$$

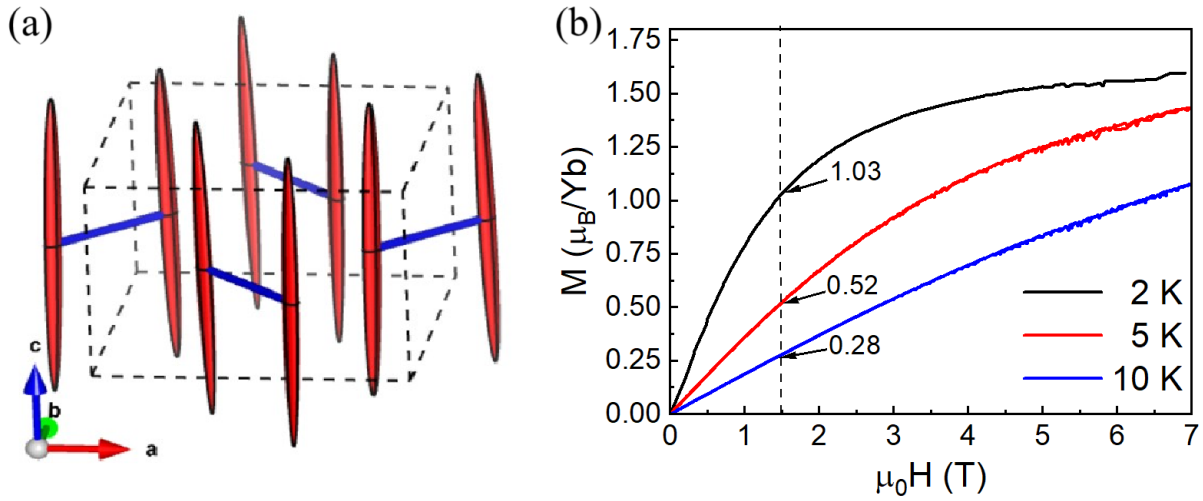

Figure 5.10: (a) The magnetization ellipsoids obtained from the pNPD analysis at 5 K. The Yb^{3+} anisotropy is nearly Ising with a strong tendency for the moments to align close to the crystallographic *c*-axis. (b) Magnetization vs applied magnetic field for polycrystalline $Yb_2Be_2SiO_7$ at 2 K, 5 K, and 10 K.

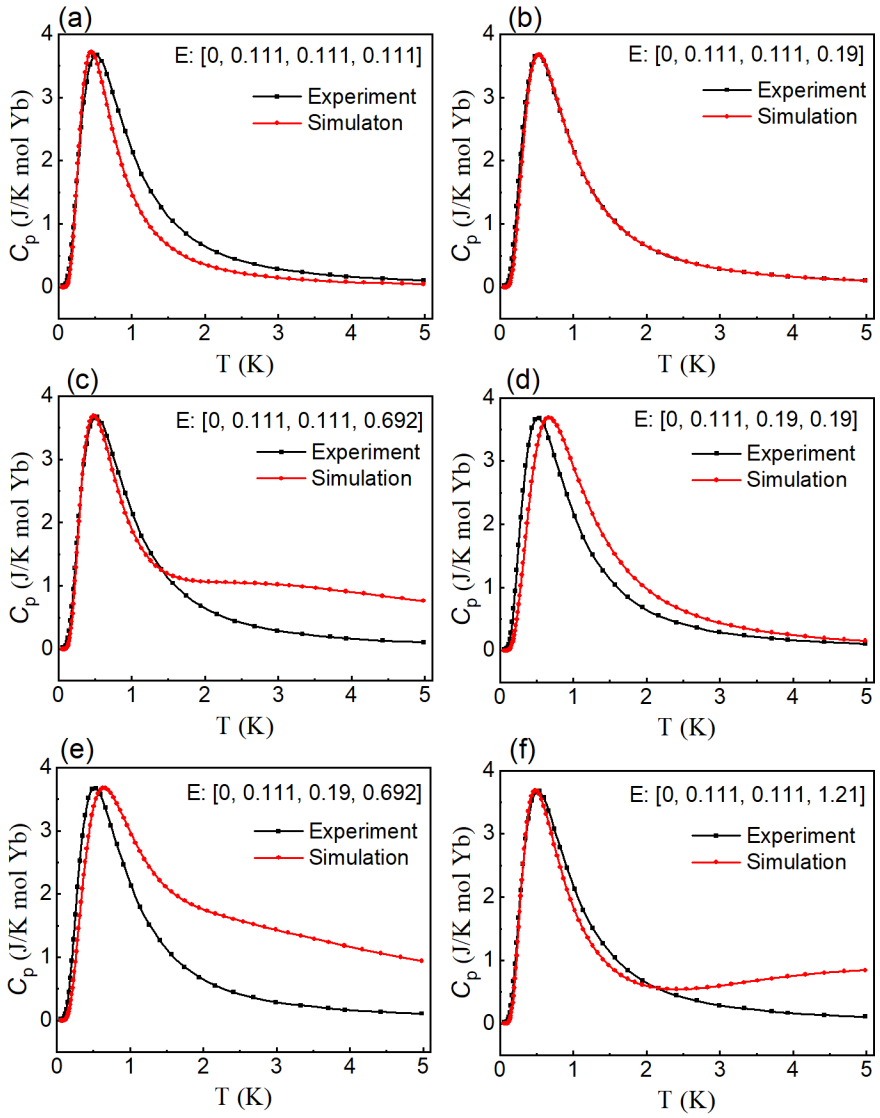

Figure 5.11: Simulations for different single-dimer models are superimposed on the data in panels (a-f). The simulation with a doubly-degenerate 0.11 meV excitation and a non-degenerate 0.19 meV excitation describes the data best.

Where the superscript l denotes dimers in sub-lattice A/B, S_i^α refers to the $\alpha(= x, y, z)$ component of the effective spin 1/2 operator with $x = [1, 1, 0]$ and $y = [-1, 1, 0]$ and $z = [0, 0, 1]$, $J_{\alpha\alpha}^l$ represents one component of the intradimer exchange tensor for dimers in each sub-lattice, H^α is the α component of the applied magnetic field, and $g_{\alpha\beta}^l$ represents one component of the g-tensor.

Our model is defined in global crystallographic coordinates and it is equivalent to the one defined within the local basis after proper rotations. Constrained by the time-reversal and mirror symmetries, this Hamiltonian takes a diagonal form with an XYZ type of spin anisotropy in the reference frame defined above, and the couplings on the two sub-lattices are related by a 90° rotation about the crystallographic [001]-axis so that $J_{xx/yy}^A = J_{yy/xx}^B$ and $J_{zz}^A = J_{zz}^B$. Although off-diagonal g-tensor components are allowed by symmetry, our pNPD results described above suggest they are much smaller than the diagonal ones. We hence take the approximation that the g-tensor follows the same symmetry as the exchange tensor. With the principal g-tensor directions now fixed along high-symmetry crystallographic directions, we estimated the g-tensor values by using the 2 K magnetization data presented in Fig 5.3 and obtain $g_{xx}^A = 1.64\ \mu_B$, $g_{yy}^A = 1.71\ \mu_B$, and $g_{zz}^A = 4.6\ \mu_B$.

Diagonalizing this Hamiltonian generates the following eigenvalues:

$$\begin{aligned} E_0 &= \frac{1}{4}(-J_{xx}^{A/B} + J_{yy}^{A/B} + J_{zz}^{A/B}) \\ E_1 &= \frac{1}{4}(J_{xx}^{A/B} + J_{yy}^{A/B} - J_{zz}^{A/B}) \\ E_2 &= \frac{1}{4}(J_{xx}^{A/B} - J_{yy}^{A/B} + J_{zz}^{A/B}) \\ E_3 &= \frac{1}{4}(-J_{xx}^{A/B} - J_{yy}^{A/B} - J_{zz}^{A/B}) \end{aligned} \tag{5.2}$$

The energy level scheme determined from the neutron spectroscopy and zero-field heat capacity data described above is consistent with 12 different intradimer exchange matrices. There are six solutions with $S_z = 0$ wavefunctions and six solutions with $S_z \neq 0$ wavefunctions. These two types of solutions are characterized by intense

dimer excitations with very different Q-dependences, as shown in Fig 5.12. The intense excitation for the $S_z = 0$ solutions is described by the structure factor,

$$S(Q) = A\left(1 - \frac{sin(Qd)}{Qd}\right) \tag{5.3}$$

where A is a constant and d is the intradimer distance. These solutions cannot explain the Q-dependence of the 0.11 meV mode so they can be discarded. The intense excitation for the $S_z \neq 0$ solutions is described by the structure factor,

$$S(Q) = A\frac{sin(Qd)}{Qd} \tag{5.4}$$

which accounts for the Q-dependence of the 0.11 meV mode well as shown in Fig 5.14. Two of the $S_z \neq 0$ solutions can be ruled out because their most intense mode is located at 0.19 meV, which is inconsistent with the neutron spectroscopy data. This leaves four models out of the 12 possibilities that were consistent with the Q-dependence and energy of the most intense mode measured by neutron spectroscopy. The eigenvectors for these four models are as follows:

$$\begin{aligned}
\psi_0 &= \frac{1}{\sqrt{2}}(\uparrow\uparrow - \downarrow\downarrow) \\
\psi_1 &= \frac{1}{\sqrt{2}}(\uparrow\downarrow + \downarrow\uparrow) \\
\psi_2 &= \frac{1}{\sqrt{2}}(\uparrow\uparrow + \downarrow\downarrow) \\
\psi_3 &= \frac{1}{\sqrt{2}}(\uparrow\downarrow - \downarrow\uparrow)
\end{aligned} \tag{5.5}$$

The simulation results of the four models are presented in Fig 5.13.

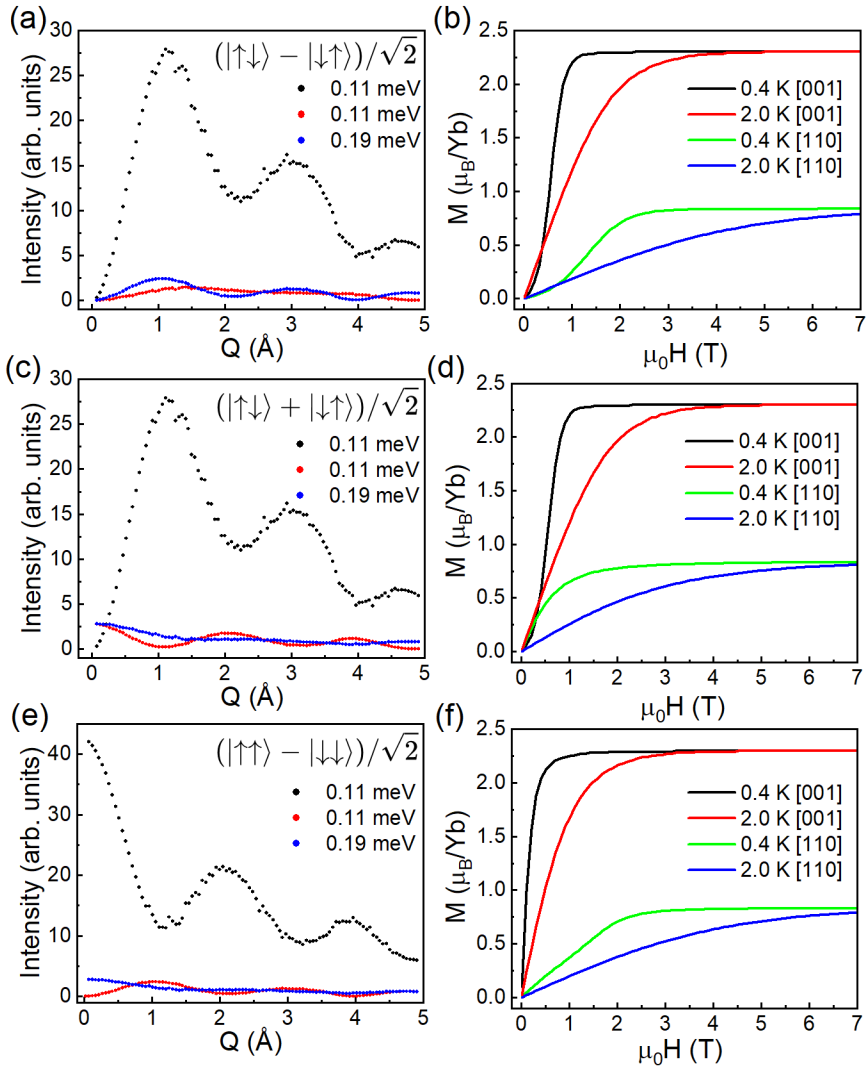

Figure 5.12: (a) Simulated powder dynamical structure factor $S(Q)$ for the three excitations and (b) simulated single crystal anisotropic magnetization at both 0.4 K and 2 K for an isolated dimer model with anisotropic exchange using the parameters $J_{xx} = 0.03$ meV, $J_{yy} = 0.19$ meV, and $J_{zz} = 0.19$ meV with the dimer ground state $\frac{1}{\sqrt{2}}(\uparrow\downarrow - \downarrow\uparrow)$. (c-d) Similar simulations for a second isolated dimer model using the parameters $J_{xx} = -0.19$ meV, $J_{yy} = -0.03$ meV, and $J_{zz} = 0.19$ meV with the dimer ground state $\frac{1}{\sqrt{2}}(\uparrow\downarrow + \downarrow\uparrow)$. (e-f) Similar simulations for a third isolated dimer model using the parameters $J_{xx} = 0.19$ meV, $J_{yy} = -0.03$ meV, and $J_{zz} = -0.19$ meV with the dimer ground state $\frac{1}{\sqrt{2}}(\uparrow\uparrow - \downarrow\downarrow)$.

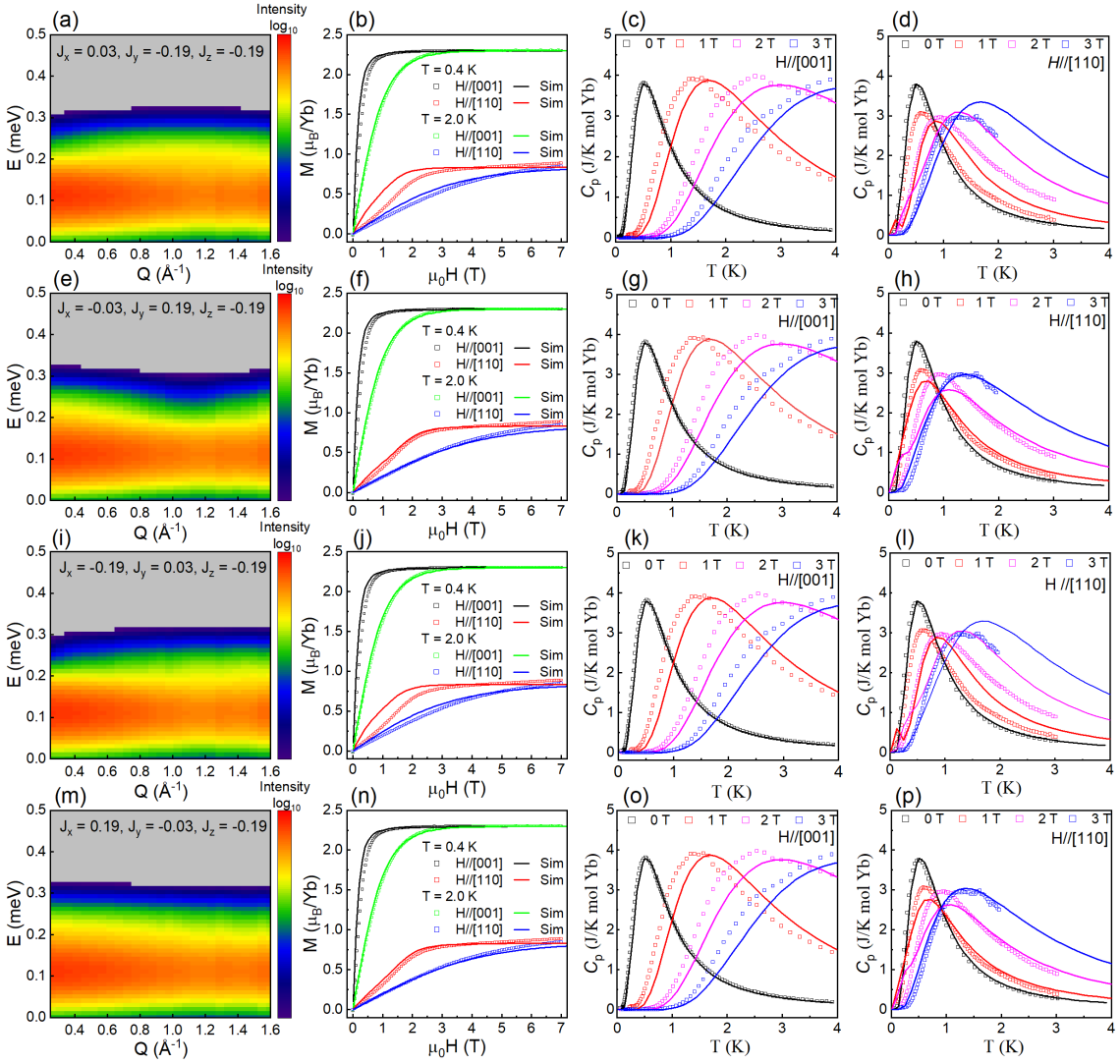

Figure 5.13: Simulated dynamical structure factor $S(Q, E)$ for the three excitations, (b) simulated and measured anisotropic magnetization at both 0.4 K and 2 K, (c) simulated and measured heat capacity data for $\vec{H} \parallel [001]$, and (d) simulated and measured heat capacity data for $\vec{H} \parallel [110]$. The simulations correspond to an isolated dimer model with anisotropic exchange using the parameters $J_{xx} = 0.03$ meV, $J_{yy} = -0.19$ meV, and $J_{zz} = -0.19$ meV. Similar dynamical structure factor simulations and the same bulk characterization data with similar simulations superimposed on it for (e-h) an isolated dimer model with $J_{xx} = -0.03$ meV, $J_{yy} = 0.19$ meV, and $J_{zz} = -0.19$ meV, (i-l) an isolated dimer model with $J_{xx} = -0.19$ meV, $J_{yy} = 0.03$ meV, and $J_{zz} = -0.19$ meV, and (m-p) an isolated dimer model with $J_{xx} = 0.19$ meV, $J_{yy} = -0.03$ meV, and $J_{zz} = -0.19$ meV. The fourth set of simulations show the best agreement with the experimental data.

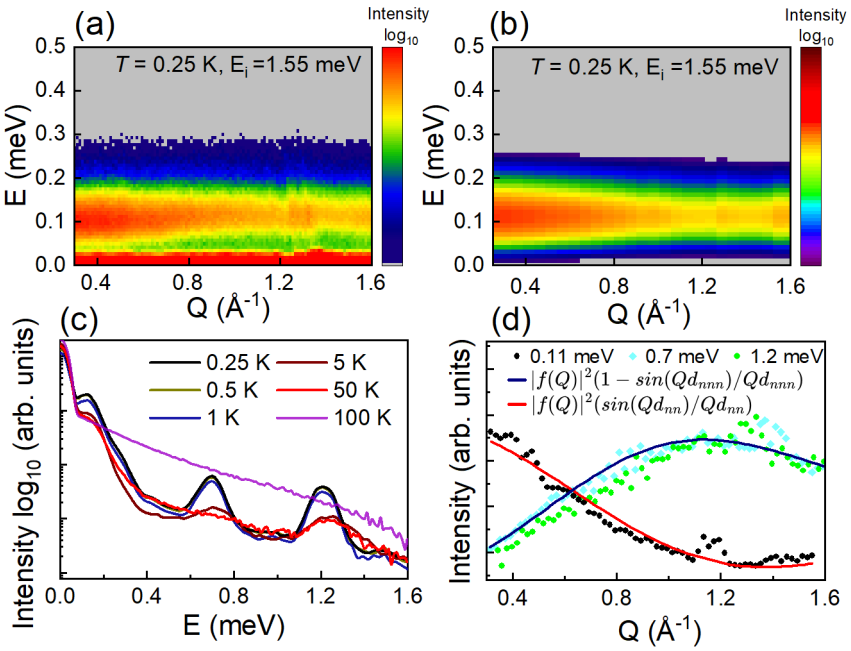

Figure 5.14: (a) Color contour plot of the scattering intensity as a function of momentum and energy transfer at 0.25 K from CNCS with $E_i = 1.55$ meV. A weakly-dispersive mode with a magnetic origin is centered at 0.11 meV. (b) Color contour plot of the simulated scattering intensity using an isolated dimer model with the anisotropic intradimer exchange parameters provided in the main text. (c) Constant-Q cuts of the scattering intensity (Q integration range $[0.5, 1.8]$ Å^{-1}) with $E_i = 2.49$ meV at selected temperatures. Aside from the main excitation band centered at 0.11 meV with a shoulder at 0.19 meV, there are two higher excitation bands centered at 0.7 meV and 1.2 meV respectively. (d) Constant-E cuts centered about three different mode positions, with an energy integration range $\pm$ 0.05 meV for the lowest mode ($E_i = 1.55$ meV data) and an integration range of $\pm$ 0.1 meV for the two higher modes ($E_i = 2.49$ meV data). The Q-dependence of the lower excitation band and the upper two excitation bands is strikingly different. Simulations based on two different types of single dimer ground states are superimposed on the data and describe it well.

It is interesting to note that all four models have single-dimer ground states of the form $(\uparrow\uparrow + \downarrow\downarrow)/\sqrt{2}$ or $(\uparrow\uparrow - \downarrow\downarrow)/\sqrt{2}$ with a dominant contribution from the other $S_z \neq 0$ wavefunction to the doubly-degenerate first excited state. Two of the solutions show superior agreement with the $\vec{H} \parallel [110]$ bulk characterization data. The only way to differentiate between these two solutions is via subtle intensity differences in the weaker dimer excitation at 0.19 meV. One solution is characterized by an oscillatory Q-dependence around this energy transfer range that is not observed in the data. Therefore, the intradimer exchange matrix that describes both the neutron spectroscopy and the bulk characterization data best is given by $J^A_{xx} = 0.19$ meV, $J^A_{yy} = -0.03$ meV, and $J^A_{zz} = -0.19$ meV.

Using the Hamiltonian parameters provided above, the neutron spectroscopy simulation is shown in Fig 5.14 (b) and the calculated magnetization and heat capacity data are superimposed on the corresponding experimental datasets in Fig 5.15. The agreement between experiment and theory is excellent, with the small differences between the $\vec{H} \parallel [001]$ heat capacity data and the simulation likely arising from modest sample misalignment. This simulation yields an effective $S = 1$ dimer state $(\uparrow\uparrow - \downarrow\downarrow)/\sqrt{2}$ in zero field, which is stabilized by the large ferromagnetic exchange interaction J_{zz} along the quantization axis. The excited states are doubly degenerate $(\uparrow\uparrow + \downarrow\downarrow)/\sqrt{2}$ and $(\uparrow\downarrow - \downarrow\uparrow)/\sqrt{2}$ at $E = 0.11$ meV and $(\uparrow\downarrow + \downarrow\uparrow)/\sqrt{2}$ at $E = 0.19$ meV, respectively. This isolated dimer model accounts for the major experimental features well, including the Q and E-dependence of the dynamical structure factor for the dimer excitations and the magnetic-field-dependence of the magnetization and specific heat. These results confirm that the interdimer interactions are significantly weaker than the intradimer interactions in $Yb_2Be_2SiO_7$.

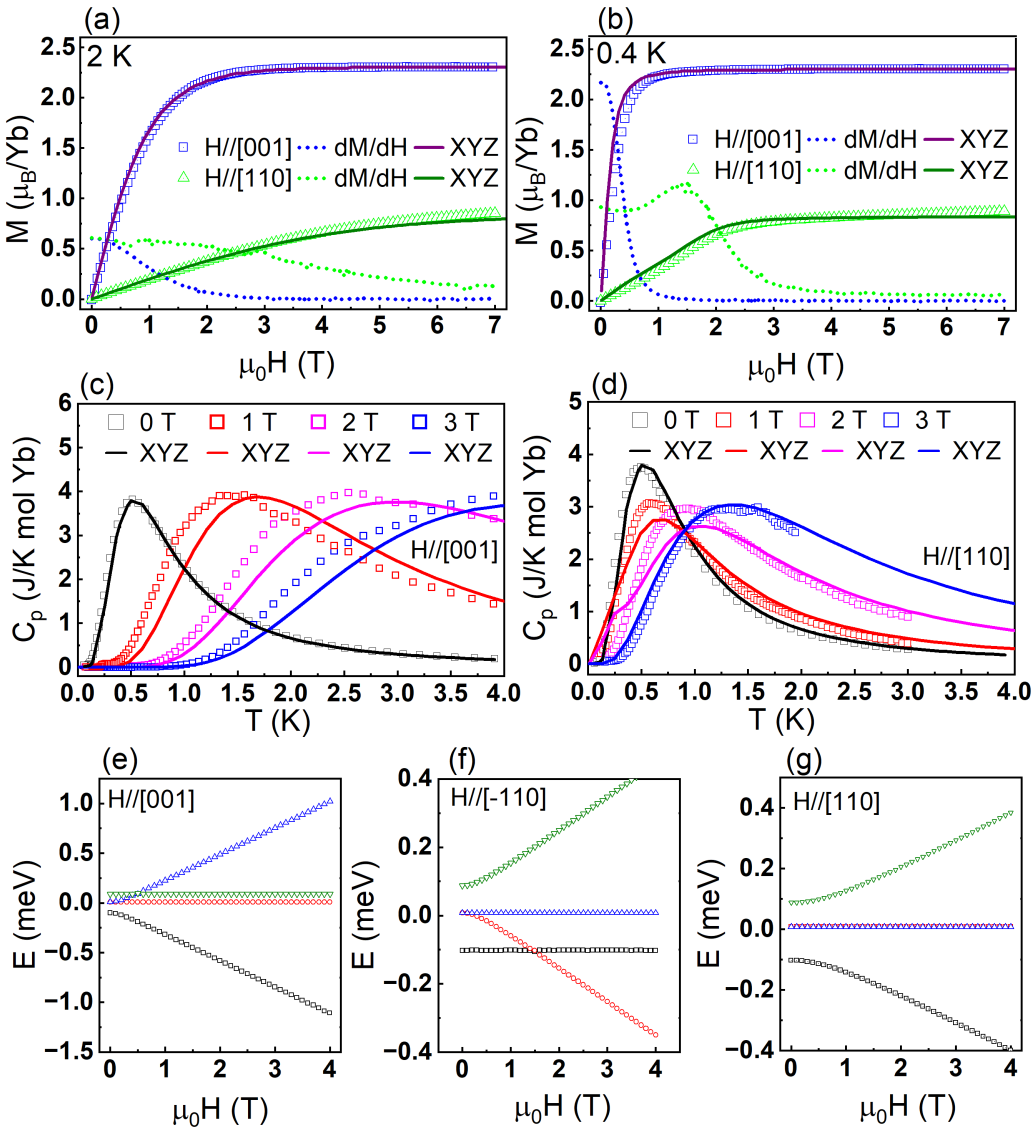

Figure 5.15: (a) Magnetization vs field along two high-symmetry crystallographic directions at 2 K. (b) Similar data collected at 0.4 K. (c) Heat capacity vs magnetic field applied along the [001] direction. Experimental data are shown as open symbols while simulated data from our XYZ anisotropic exchange model are shown as solid curves. (d) Heat capacity data vs magnetic field applied along the [110] direction with simulated data from the same model superimposed on it. (e-g) Simulated isolated dimer energy levels vs applied field along different crystallographic directions for one dimer sublattice based on the XYZ anisotropic exchange model. There is a level crossing between 1.5 T and 2 T for one dimer sublattice when $\vec{H} \parallel [-110]$ or for the other dimer sublattice when $\vec{H} \parallel [110]$.

The neutron spectroscopy simulations of the dynamical structure factor for transitions between the single dimer levels j and k were performed using the expression:

$$S(\vec{Q},E) = A\sum_{j,k} exp\left(-\frac{E_j}{k_BT}\right)\sum_{\alpha,\beta}\left(\delta_{\alpha,\beta}-\frac{Q_\alpha Q_\beta}{Q^2}\right)\times \sum_{m,n} f_n^*(\vec{Q})f_m(\vec{Q})\ exp(i\vec{Q}\cdot(\vec{R}_m-\vec{R}_n))\times \psi_j S_m^\alpha \psi_k \times \psi_k S_n^\beta \psi_j \delta(E+E_j-E_k) \quad (5.6)$$

where $\alpha,\beta = x,y,z$, S_m^α refers to the α component of the effective spin-1/2 operator for the mth spin, $\vec{R}_m$ and $f_m(Q)$ are the position vector and magnetic form factor of magnetic ion m, and the matrix element between two single-dimer states is $\psi_k S_n^\beta \psi_j$. The quantity A includes a constant and the Debye-Waller factor $exp(-2W)$. The neutron spectroscopy simulation was powder-averaged to facilitate direct comparison to the CNCS data using the equation:

$$S(Q,E) = \int \frac{d\Omega}{4\pi} S(\vec{Q},E) \quad (5.7)$$

To assess which excitations could be associated with single dimer physics, we simulated our low-T heat capacity data with the function [**?**]:

$$C_m(T) = \frac{1}{k_BT^2}\Big\{-\left(\frac{1}{Z}\sum_j E_j\ exp\left(-\frac{E_j}{k_bT}\right)\right)^2 + \frac{1}{Z}\sum_j E_j^2\ exp\left(-\frac{E_j}{k_bT}\right)\Big\} \quad (5.8)$$

where E_j is the eigenvalue of dimer state j, $Z = \sum_j exp(-\frac{E_j}{k_bT})$ is the partition function, and k_B is the Boltzmann factor. The XYZ Hamiltonian can yield up to three single-dimer excitations, so we tried different eigenvalue combinations in our simulations that were consistent with the four energy levels observed in neutron

spectroscopy. Several of these simulation results are presented in Fig. 5.13. We found that the two higher-energy excitations have negligible contributions to the measured heat capacity, so we do not consider them further in our single-dimer models. The best agreement between the data and the simulation is found for a single-dimer model with a doubly-degenerate 0.11 meV excitation and a non-degenerate 0.19 meV excitation.

The magnetization simulations were performed using the expression:

$$M(\vec{H},T) = \frac{1}{N}\sum_{m}\frac{1}{Z}\sum_{j}\psi_j(\vec{H})\mu_B\ \vec{g}_m\cdot\vec{S}_m\psi_j(\vec{H})\times exp\left(-\frac{E_j}{k_bT}\right) \quad (5.9)$$

where N is the number of magnetic ions in a unit cell, $\psi_j(\vec{H})$ is the eigenfunction of dimer state j in an applied magnetic field $\vec{H}$, g_m is the g-tensor of the mth spin, and $\vec{S}_m$ is the effective spin-1/2 operator of the mth spin. The field-dependent heat capacity simulations were performed using Eq. (2) with modified eigenvalues obtained by diagonalizing the XYZ Hamiltonian with the appropriate Zeeman term included.

5.6 Summary

$Yb_2Be_2SiO_7$ single crystals were similarly prepared using the floating zone melt method. Subsequent bulk measurements show no signs of long range order at temperatures as low as 0.05 K. In addition, neutron diffraction measurements at 2 K and 0.25 K show similar patterns matching the nuclear phase with no additional peaks or intensity.

The three CEF excitations expected from J = 7/2 Kramer's Yb ion are identified with the lowest doublet found at 11 meV. The CEF peaks are unusually broad which might indicate some source of structural disorder. Although a determination of the CEF Hamiltonian for this compound is likely impossible, we are able to obtain some infomation about the ground state g-tensor utilizing half-polarized neutron powder

diffraction (pNPD). The pNPD results suggest that the Yb^{3+} ions are nearly ising like with a much larger g-tensor component along [001] and much smaller in-plane components.

Neutron scattering experiments with cold neutrons having incident energies of 1.5 meV reveal the existence of several spin-gap excitations associated with transitions between singlet and triplet wave functions. Analysis of Q-dependent powder dispersion spectrum indicates that the excitations at 0.11 meV and 0.19 meV correspond to entangled units between NN with the S_{tot} and $S_z = 1$ wave function $(\uparrow\uparrow - \downarrow\downarrow)/\sqrt{2}$. While the same data indicates that the excitations at 0.7 meV and 1.2 meV correspond to entangled units between NNN with the more typical entangled unit wave function $(\uparrow\downarrow - \downarrow\uparrow)/\sqrt{2}$.

To simulate the observed bulk magnetic properties and cold neutron scattering data a simple model of isolated dimer units with anisotropic XYZ exchange is employed. The exchange parameters $J_x = 0.19$ meV, J_y =-0.03 meV, and J_z = -0.19 meV produce the closest match to the measured data and reproduces well the two observed low energy excitations, the zero-field and field dependent heat capacity, and magnetization data. However, small differences between the simulated and measured Magnetization and heat capacity indicate that NNN or inter-dimer interactions play a role and must be considered to explain these differences .

Chapter 6

Conclusions

The compound family $R_2Be_2SiO_7$ offers a rare opportunity to experimentally study the magnetic phases and properties of highly anisotropic moments arranged into a geometrically frustrated Shastry-Sutherland lattice. In this thesis the atomic structure of this iso-structural family is presented and the magnetic properties of $Er_2Be_2SiO_7$, $Dy_2Be_2SiO_7$, and $Yb_2Be_2SiO_7$ are investigated in detail. The sub-lattice formed by the R^{3+} ions in $R_2Be_2SiO_7$ is equivalent to an SSL lattice where each ion has one nearest or intra-dimer neighbor and four next-nearest or inter-dimer neighbors.

$Er_2Be_2SiO_7$ single crystals were grown from polycrystalline sample using the floating zone melt method. Subsequent bulk magnetization, ac magnetic susceptibility, and heat capacity measurements reveal a phase transition to an antiferromagnetic ordered state at $T_N = 0.85$ K. The 8-coordinated ligand environment surrounding each Er^{3+} ion can be described as an anti-prism with the four oxygen ions above the plane rotated relative to the four below the plane. The Er ions belong to one of two sub-lattices such that nearest neighbors or the two ions that form a dimer are always in the same sub-lattice and adjacent orthogonal dimers always belong to different sub-lattices. The ligand environments in the two sub-lattices are reflected relative to one another along the plane defined by the [001] axis.

The single ion anisotropy of each Er ion is quasi-XY like with a preference to lie along the normal to their local mirror plane which is defined either by the [110] or [1-10] vectors depending on the sub-lattice. Neutron scattering data allows for the determination of all seven CEF levels expected of the J = 15/2 Er ion. The lowest CEF level is at just 1.7 mev which suggests that an $S_{eff} = 1/2$ model is not appropriate. Although several candidate solutions to the CEF Hamiltonian are proposed, a robust determination is complicated by the low site symmetry and remains elusive at this time.

The zero-field ground state is described the Γ_1 IR vector and consists of antiferromagneticly coupled dimers with in-plane moments perpendicular to the dimer bond. The four ions in a unit cell form a square plaquette with two moments pointing in and two moments pointing out. The $\vec{k}$ = (0,0,0.5) magnetic propagation vector identified in neutron diffraction experiments also ensures that there is antiferromagnetic coupling between the Shastry-Sutherland planes. The field induced behavior of the spins is consistent with classical anisotropic moments. For field applied out of plane along the [001]-axis with two intermediate magnetic phases between the zero field Γ_1 IR phase and the fully polarized phase. One intermediate phase has a $2\vec{k}$ magnetic structure corresponding to a gradual canting of the moments towards the *c*-axis with increasing field, while the nature of the second intermediate phase remains unknown.

$Dy_2Be_2SiO_7$ single crystals were similarly prepared using the floating zone melt method. Subsequent bulk measurements reveal a transition to an antiferromagnetic ordered ground state below T_N = 1.1 K. Magnetization measurements show at least three field induced phases before saturation corresponding to plateaus at 1/7, 4/9, and 2/3 fractions of the saturation magnetization.

As was the case for $Er_2Be_2SiO_7$, the Dy^{3+} ions form two sub-lattices with differing ligand environments. The single ion anisotropy is complicated and of the XYZ form with g_{110} (parallel to NN bond) $\geq$ g_{-110} (perpendicular to NN bond) $\geq$ g_{001}. This anisotropy results in a strong tendency for moments to lie in the ab-plane. Although

it was not possible to determine all seven CEF levels expected for the J = 15/2 Dy ion the lowest CEF level is identified at 7.9 meV. This result alongside the integrated entropy from heat capacity measurements indicate that an $S_{eff} = 1/2$ model is appropriate.

The zero-field ground state is described the Γ_4 IR vector and consists of antiferromagneticly coupled dimers with in-plane moments parallel to the dimer bond. The four ions in a unit cell form a square plaquette with the moments forming a spiral or loop with a distinct handedness. The $\vec{k}$ = (0,0,0.5) magnetic propagation vector identified in neutron diffraction experiments ensures that antiferromagnetic coupling between the planes exists. The nature and spin structure of the field induced phases remains unknown. However, it is worth noting that the (0,0,0.5) magnetic propagation vector persists only in the first field induced phase and is replaced by a (0,0,0) propagation vector in the two subsequent phases.

$Yb_2Be_2SiO_7$ single crystals were similarly prepared using the floating zone melt method. Subsequent bulk measurements show no signs of long range order at temperatures as low as 0.05 K. In addition, neutron diffraction measurements at 2 K and 0.25 K show similar patterns matching the nuclear phase with no additional peaks or intensity.

The three CEF excitations expected from J = 7/2 Kramer's Yb ion are identified with the lowest doublet found at 11 meV. The CEF peaks are unusually broad which might indicate some source of structural disorder. Although a determination of the CEF Hamiltonian for this compound is likely impossible we are able to obtain some infomation about the ground state g-tensor utilizing half-polarized neutron powder diffraction (pNPD). The pNPD results suggest that the Yb^{3+} ions are nearly ising like with a much larger g-tensor component along [001] and much smaller in-plane components.

Neutron scattering experiments with cold neutrons having incident energies of 1.5 meV reveal the existence of several spin-gap excitations associated with transitions between singlet and triplet wave functions. Analysis of Q-dependent

powder dispersion spectrum indicates that the excitations at 0.11 meV and 0.19 meV correspond to entangled units between NN with the S_{tot} and $S_z = 1$ wave function $(\uparrow\uparrow - \downarrow\downarrow)/\sqrt{2}$. While the same data indicates that the excitations at 0.7 meV and 1.2 meV correspond to entangled units between NNN with the more typical entangled unit wave function $(\uparrow\downarrow - \downarrow\uparrow)/\sqrt{2}$.

To simulate the observed bulk magnetic properties and cold neutron scattering data a simple model of isolated dimer units with anisotropic XYZ exchange is employed. The exchange parameters $J_x = 0.19$ meV, J_y =-0.03 meV, and J_z = -0.19 meV produce the closest match to the measured data and reproduces well the two observed low energy excitations, the zero-field and field dependent heat capacity, and magnetization data. However, small differences between the simulated and measured Magnetization and heat capacity indicate that NNN or inter-dimer interactions play a role and must be considered to explain these differences.

While the work presented in this thesis represents a good start to the analysis of magnetism in $R_2Be_2SiO_7$ compounds it also highlights the need for further investigation. Although several magnetization plateaus have been observed in $Dy_2Be_2SiO_7$ the nature and spin structure of these phases remains unknown and additional single crystal neutron diffraction studies remain necessary to clarify this. Additional theoretical analysis to determine an accurate field induced Hamiltonian capable of explaining the plateau phases is also necessary. For $Yb_2Be_2SiO_7$ a ground state consisting of unique dimer units is identified and much of the observed data is explained by the simple model of isolated dimers presented in this work. However, this data also suggests that inter-dimer or NNN interactions though small are present and may influence both the ground state and field induced states. The nature of the four spin gap excitations observed in neutron scattering data also requires further investigation. Present work suggests that the excitations at lower energies of $\sim$0.11 meV and $\sim$0.19 meV correspond to excitations from a unique ground state consisting of anti-symmetric entangle units with $S_{tot} = 1$ and $S_z = 1$. On the other hand, the much weaker excitations at $\sim$0.7 meV and $\sim$1.2 meV appear to be due to a small

amount of structural disorder which causes some Yb ions to realize a different dimer ground state. To confirm the wavefunction of the identified ground state and the states associated with the two observed excitations additional cold neutron scattering experiments on single crystal of $Yb_2Be_2SiO_7$ both in zero field and under applied field are sorely needed. Additional studies on site diluted $Lu_xYb_{2-x}Be_2SiO_7$ could also be helpful in clarifying the nature of weak excitations at $\sim$0.7 meV and $\sim$1.2 meV and general interplay between NN interactions and NNN interactions in $Yb_2Be_2SiO_7$.

Bibliography

[1] C. G. Shull and J. Samuel Smart. Detection of antiferromagnetism by neutron diffraction. *Phys. Rev.*, 76:1256–1257, Oct 1949. 1

[2] A P Ramirez. Strongly geometrically frustrated magnets. *Annual Review of Materials Research*, 24(Volume 24,):453–480, 1994. 1

[3] John E. Greedan. Geometrically frustrated magnetic materials. *J. Mater. Chem.*, 11:37–53, 2001. 1, 3

[4] Roderich Moessner and Arthur P. Ramirez. Geometrical frustration. *Physics Today*, 59(2):24–29, 02 2006. 1

[5] B. Sriram Shastry and Bill Sutherland. Exact ground state of a quantum mechanical antiferromagnet. *Physica B+C*, 108(1):1069–1070, 1981. 2, 3, 7

[6] A. Brassington, Q. Huang, A. A. Aczel, and H. D. Zhou. Synthesis and magnetic properties of the Shastry-Sutherland family $R_2Be_2SiO_7$ (R = Nd,Sm,Gd-Yb). *Phys. Rev. Mater.*, 8:014005, Jan 2024. 2, 9, 16

[7] Oleg A Starykh. Unusual ordered phases of highly frustrated magnets: a review. *Reports on Progress in Physics*, 78(5):052502, apr 2015. 3

[8] Jia-Xin Yin, Biao Lian, and M. Zahid Hasan. Topological kagome magnets and superconductors. *Nature*, 612(7941):647–657, 2022. 3

[9] Jason S. Gardner, Michel J. P. Gingras, and John E. Greedan. Magnetic pyrochlore oxides. *Rev. Mod. Phys.*, 82:53–107, Jan 2010. 3

[10] Luca Capriotti, Federico Becca, Alberto Parola, and Sandro Sorella. Resonating valence bond wave functions for strongly frustrated spin systems. *Phys. Rev. Lett.*, 87, Aug 2001. 3

[11] R. Moessner and S. L. Sondhi. Resonating valence bond phase in the triangular lattice quantum dimer model. *Phys. Rev. Lett.*, 86:1881–1884, Feb 2001. 3

[12] Vivien Zapf, Marcelo Jaime, and C.D. Batista. Bose-einstein condensation in quantum magnets. *Reviews of Modern Physics*, 86(2):563–614, May 2014. 3

[13] Indrani Bose. Spin gap antiferromagnets: materials and phenomena. 2005. 3

[14] Steven T. Bramwell and Michel J. P. Gingras. Spin ice state in frustrated magnetic pyrochlore materials. *Science*, 294(5546):1495–1501, 2001. 3

[15] Steven T Bramwell and Mark J Harris. The history of spin ice. *Journal of Physics: Condensed Matter*, 32(37):374010, 2020. 3

[16] A.P Ramirez, C.L Broholm, R.J Cava, and G.R Kowach. Geometrical frustration, spin ice and negative thermal expansion – the physics of underconstraint. *Physica B: Condensed Matter*, 280(1):290–295, 2000. 3

[17] John E. Greedan. Frustrated rare earth magnetism: Spin glasses, spin liquids and spin ices in pyrochlore oxides. *Journal of Alloys and Compounds*, 408-412:444–455, 2006. 3

[18] L Balents. Spin liquids in frustrated magnets. *Nature*, 464:199, 2010. 3

[19] L Savary and L Balents. Quantum spin liquids: a review. *Rep. Prog. Phys.*, 80:016502, 2017. 3

[20] Y Zhou, K Kanoda, and T K Ng. Quantum spin liquid states. *Rev. Mod. Phys.*, 89:025003, 2017. 3

[21] M. R. Norman. Colloquium: Herbertsmithite and the search for the quantum spin liquid. *Rev. Mod. Phys.*, 88:041002, Dec 2016. 3

[22] J Knolle and R Moessner. A field guide to spin liquids. *Annu. Rev. Condens. Matter Phys.*, 10:451, 2019. 3

[23] H Takagi, T Takayama, G Jackeli, G Khaliullin, and S E Nagler. Concept and realization of Kitaev quantum spin liquids. *Nat. Rev. Phys.*, 1:264, 2019. 3

[24] J Wen, S L Yu, S Li, W Yu, and J X Li. Experimental identification of quantum spin liquids. *npj Quantum Mater.*, 4:12, 2019. 3

[25] C Broholm, R J Cava, S A Kivelson, D G Nocera, M R Norman, and T Senthil. Quantum spin liquids. *Science*, 367:263, 2020. 3

[26] J R Chamorro, T M McQueen, and T T Tran. Chemistry of quantum spin liquids. *Chem. Rev.*, 121:2898, 2021. 3

[27] M Moliner, D C Cabra, A Honecker, P Pujol, and F Stauffer. Magnetization plateaux in the classical shastry-sutherland lattice. *Journal of Physics: Conference Series*, 145(1):012053, jan 2009. 3, 7

[28] Taras Verkholyak, Jozef Strečka, Frédéric Mila, and Kai P. Schmidt. Exact ground states of a spin-$\frac{1}{2}$ ising-heisenberg model on the shastry-sutherland lattice in a magnetic field. *Phys. Rev. B*, 90:134413, Oct 2014. 7

[29] Alexei Grechnev. Exact ground state of the shastry-sutherland lattice with classical heisenberg spins. *Phys. Rev. B*, 87:144419, Apr 2013. 7

[30] Paul Kairys, Andrew D. King, Isil Ozfidan, Kelly Boothby, Jack Raymond, Arnab Banerjee, and Travis S. Humble. Simulating the shastry-sutherland ising model using quantum annealing. *PRX Quantum*, 1:020320, Dec 2020. 7

[31] W C Huang, L Huo, G Tian, H R Qian, X S Gao, M H Qin, and J-M Liu. Multi-step magnetization of the ising model on a shastry–sutherland lattice: a monte carlo simulation. *Journal of Physics: Condensed Matter*, 24(38):386003, aug 2012. 7

[32] Yu. I. Dublenych. Ground states of the ising model on the shastry-sutherland lattice and the origin of the fractional magnetization plateaus in rare-earth-metal tetraborides. *Phys. Rev. Lett.*, 109:167202, Oct 2012. 7

[33] Takahumi Suzuki, Yusuke Tomita, and Naoki Kawashima. Magnetic properties of the spin-$\frac{1}{2}$ xxz model on the shastry-sutherland lattice: Effect of long-range interactions. *Phys. Rev. B*, 80:180405, Nov 2009. 7

[34] Zi Yang Meng and Stefan Wessel. Phases and magnetization process of an anisotropic shastry-sutherland model. *Phys. Rev. B*, 78:224416, Dec 2008. 7

[35] H Kageyama, K Onizuka, T Yamauchi, and Y Ueda. Crystal growth of the two-dimensional spin gap system $SrCu_2(BO_3)_2$. *Journal of Crystal Growth*, 206(1):65–67, 1999. 7, 66

[36] H. Kageyama, K. Yoshimura, R. Stern, N. V. Mushnikov, K. Onizuka, M. Kato, K. Kosuge, C. P. Slichter, T. Goto, and Y. Ueda. Exact dimer ground state and quantized magnetization plateaus in the two-dimensional spin system $SrCu_2(BO_3)_2$. *Phys. Rev. Lett.*, 82:3168–3171, Apr 1999. 7, 66

[37] Shin Miyahara and Kazuo Ueda. Exact dimer ground state of the two dimensional Heisenberg spin system $SrCu_2(BO_3)_2$. *Phys. Rev. Lett.*, 82:3701–3704, May 1999. 7, 8, 66

[38] Hiroyuki Nojiri, Hiroshi Kageyama, Kenzo Onizuka, Yutaka Ueda, and Mitsuhiro Motokawa. Direct observation of the multiple spin gap excitations in two-dimensional dimer system srcu 2(bo 3) 2. *Journal of the Physical Society of Japan*, 68(9):2906–2909, 1999. 7

[39] M. E. Zayed, Ch. Rüegg, J. Larrea J., A. M. Läuchli, C. Panagopoulos, S. S. Saxena, M. Ellerby, D. F. McMorrow, Th. Strässle, S. Klotz, G. Hamel, R. A. Sadykov, V. Pomjakushin, M. Boehm, M. Jiménez–Ruiz, A. Schneidewind, E. Pomjakushina, M. Stingaciu, K. Conder, and H. M. Rønnow. 4-spin plaquette singlet state in the shastry–sutherland compound srcu2(bo3)2. *Nature Physics*, 13(10):962–966, July 2017. 7, 8

[40] Ellen Fogh, Mithilesh Nayak, Oleksandr Prokhnenko, Maciej Bartkowiak, Koji Munakata, Jian-Rui Soh, Alexandra A. Turrini, Mohamed E. Zayed, Ekaterina Pomjakushina, Hiroshi Kageyama, Hiroyuki Nojiri, Kazuhisa Kakurai, Bruce Normand, Frédéric Mila, and Henrik M. Rønnow. Field-induced bound-state condensation and spin-nematic phase in srcu2(bo3)2 revealed by neutron scattering up to 25.9 t. *Nature Communications*, 15(1), 2024. 7

[41] Zhenzhong Shi, Sachith Dissanayake, Philippe Corboz, William Steinhardt, David Graf, D. M. Silevitch, Hanna A. Dabkowska, T. F. Rosenbaum, Frédéric Mila, and Sara Haravifard. Discovery of quantum phases in the shastry-sutherland compound srcu2(bo3)2 under extreme conditions of field and pressure. *Nature Communications*, 13(1), April 2022. 8

[42] Jing Guo, Pengyu Wang, Cheng Huang, Bin-Bin Chen, Wenshan Hong, Shu Cai, Jinyu Zhao, Jinyu Han, Xintian Chen, Yazhou Zhou, Shiliang Li, Qi Wu, Zi Yang Meng, and Liling Sun. Deconfined quantum critical point lost in pressurized srcu2(bo3)2. *Communications Physics*, 8(1), February 2025. 8

[43] Zheng Weihong, C. J. Hamer, and J. Oitmaa. Series expansions for a heisenberg antiferromagnetic model forsrcu2(bo3)2. *Physical Review B*, 60(9):6608–6616, September 1999. 8, 66

[44] Philippe Corboz and Frédéric Mila. Crystals of bound states in the magnetization plateaus of the shastry-sutherland model. *Physical Review Letters*, 112(14), April 2014. 8

[45] P. A. McClarty, F. Krüger, T. Guidi, S. F. Parker, K. Refson, A. W. Parker, D. Prabhakaran, and R. Coldea. Topological triplon modes and bound states in a shastry–sutherland magnet. *Nature Physics*, 13(8):736–741, May 2017. 8

[46] S. Michimura, A. Shigekawa, F. Iga, M. Sera, T. Takabatake, K. Ohoyama, and Y. Okabe. Magnetic frustrations in the Shastry–Sutherland system ErB_4. *Physica B: Condensed Matter*, 378-380:596–597, 2006. 8

[47] D. Brunt, G. Balakrishnan, D. A. Mayoh, M. R. Lees, D. Gorbunov, N. Qureshi, and O. A. Petrenko. Magnetisation process in the rare earth tetraborides, NdB_4 and HoB_4. *Scientific Reports*, 8(1):232, Jan 2018. 8

[48] S. Yoshii, T. Yamamoto, M. Hagiwara, S. Michimura, A. Shigekawa, F. Iga, T. Takabatake, and K. Kindo. Multistep magnetization plateaus in the Shastry-Sutherland system TbB_4. *Phys. Rev. Lett.*, 101:087202, Aug 2008. 8

[49] Keola Wierschem, Sai Swaroop Sunku, Tai Kong, Toshimitsu Ito, Paul C. Canfield, Christos Panagopoulos, and Pinaki Sengupta. Origin of modulated phases and magnetic hysteresis in TmB_4. *Phys. Rev. B*, 92:214433, Dec 2015. 8

[50] H. C. Choi, Amel Laref, J. H. Shim, S. K. Kwon, and B. I. Min. Electronic structures and magnetic properties of rb4(r=yb, pr, gd, tb, dy). *Journal of Applied Physics*, 105(7), February 2009. 8

[51] S. Yoshii, T. Yamamoto, M. Hagiwara, T. Takeuchi, A. Shigekawa, S. Michimura, F. Iga, T. Takabatake, and K. Kindo. High-field magnetization of tbb4. *Journal of Magnetism and Magnetic Materials*, 310(2):1282–1284, March 2007. 8

[52] N. Qureshi, F. Bourdarot, E. Ressouche, W. Knafo, F. Iga, S. Michimura, L.-P. Regnault, and F. Duc. Possible stripe phases in the multiple magnetization plateaus in ¡mml:math

xmlns:mml="http://www.w3.org/1998/math/mathml"¿¡mml:msub¿¡mml:mtext¿tbb¡/mml:m from single-crystal neutron diffraction under pulsed high magnetic fields. *Physical Review B*, 106(9), September 2022. 8

[53] S Yoshii, T Yamamoto, M Hagiwara, A Shigekawa, S Michimura, F Iga, T Takabatake, and K Kindo. High-field magnetization of tmb4. *Journal of Physics: Conference Series*, 51:59–62, November 2006. 8

[54] Matúš Orendáč, Slavomír Gabáni, Pavol Farkašovský, Emil Gažo, Jozef Kačmarčík, Miroslav Marcin, Gabriel Pristáš, Konrad Siemensmeyer, Natalya Shitsevalova, and Karol Flachbart. Ground state and stability of the fractional plateau phase in metallic shastry–sutherland system tmb4. *Scientific Reports*, 11(1), 2021. 8

[55] G. Will, W. Schäfer, F. Pfeiffer, F. Elf, and J. Etourneau. Neutron diffraction studies of tbb4 and erb4. *Journal of the Less Common Metals*, 82:349–355, November 1981. 8

[56] F. Hulliger. On new mo2feb2-type representatives ln2rh2in. *Journal of Alloys and Compounds*, 221(1–2), 1995. 9

[57] M. Giovannini, H. Michor, E. Bauer, G. Hilscher, P. Rogl, and R. Ferro. Structural chemistry, magnetism and thermodynamic properties of r2pd2in. *Journal of Alloys and Compounds*, 280(1–2):26–38, October 1998. 9

[58] Rainer Kraft, Thomas Fickenscher, Gunter Kotzyba, Rolf-Dieter Hoffmann, and Rainer Pöttgen. Intermetallic rare earth (re) magnesium compounds repdmg and re2pd2mg. *Intermetallics*, 11(2):111–118, February 2003. 9

[59] Vasyl' I. Zaremba, Dariusz Kaczorowski, Galyna P. Nychyporuk, Ute Ch. Rodewald, and Rainer Pöttgen. Structure and physical properties of re2ge2in (re = la, ce, pr, nd). *Solid State Sciences*, 6(11):1301–1306, November 2004. 9

[60] Ahmet Doğan, Sudhindra Rayaprol, and Rainer Pöttgen. New mo2feb2type intermetallic cadmium compounds re2pd2cd (re = pr, sm, gd–lu)—synthesis, structure, and magnetic properties. *Journal of Physics: Condensed Matter*, 19(2):026209, December 2006. 9

[61] Falko M. Schappacher, Wilfried Hermes, and Rainer Pöttgen. Structure and magnetic properties of re2cu2cd. *Journal of Solid State Chemistry*, 182(2):265–272, February 2009. 9

[62] W. J. Gannon, K. Chen, M. Sundermann, F. Strigari, Y. Utsumi, K.-D. Tsuei, J.-P. Rueff, P. Bencok, A. Tanaka, A. Severing, and M. C. Aronson. Intermediate valence in single crystalline yb2si2al. *Physical Review B*, 98(7), August 2018. 9

[63] W. Miiller, L. S. Wu, M. S. Kim, T. Orvis, J. W. Simonson, M. Gamża, D. M. McNally, C. S. Nelson, G. Ehlers, A. Podlesnyak, J. S. Helton, Y. Zhao, Y. Qiu, J. R. D. Copley, J. W. Lynn, I. Zaliznyak, and M. C. Aronson. Magnetic structure of yb2pt2pb: Ising moments on the shastry-sutherland lattice. *Physical Review B*, 93(10), March 2016. 9

[64] W. J. Gannon, I. A. Zaliznyak, L. S. Wu, A. E. Feiguin, A. M. Tsvelik, F. Demmel, Y. Qiu, J. R. D. Copley, M. S. Kim, and M. C. Aronson. Spinon confinement and a sharp longitudinal mode in yb2pt2pb in magnetic fields. *Nature Communications*, 10(1), March 2019. 9

[65] T Herrmannsdörfer, P Fischer, G Böttger, L Keller, M Giovannini, and E Bauer. Magnetic ordering in the rare-earth intermetallic compounds tb2pd2in and ho2pd2in. *Physica B: Condensed Matter*, 276–278:702–703, March 2000. 9

[66] Makoto Wakeshima, Nobuyuki Taira, Yukio Hinatsu, Aya Tobo, Kenji Ohoyama, and Yasuo Yamaguchi. Specific heat and neutron diffraction study on

quaternary sulfides band2cos5 and band2zns5. *Journal of Solid State Chemistry*, 174(1):159–164, August 2003. 9

[67] T.C. Ozawa, T. Taniguchi, Y. Kawaji, S. Mizusaki, Y. Nagata, Y. Noro, H. Samata, H. Mitamura, and S. Takayanagi. Magnetization and specific heat measurement of the shastry–sutherland lattice compounds: Ln2bapdo5 (ln = la, pr, nd, sm, eu, gd, dy, ho). *Journal of Alloys and Compounds*, 448(1–2):96–103, January 2008. 9

[68] Yuto Ishii, Jie Chen, Hiroyuki K. Yoshida, Migaku Oda, Andrew D. Christianson, and Kazunari Yamaura. High-pressure synthesis, crystal structure, and magnetic properties of the shastry-sutherland-lattice oxides baln2zno5 (ln = pr, sm, eu). *Journal of Solid State Chemistry*, 289:121489, September 2020. 9

[69] Yuto Ishii, G. Sala, M. B. Stone, V. O. Garlea, S. Calder, Jie Chen, Hiroyuki K. Yoshida, Shuhei Fukuoka, Jiaqiang Yan, Clarina dela Cruz, Mao-Hua Du, David S. Parker, Hao Zhang, Cristian D. Batista, Kazunari Yamaura, and A. D. Christianson. Magnetic properties of the shastry-sutherland lattice material band2zno5. *Physical Review Materials*, 5(6), June 2021. 9

[70] Brianna R. Billingsley, Madalynn Marshall, Zhixue Shu, Huibo Cao, and Tai Kong. Single crystal synthesis and magnetic properties of a shastry-sutherland lattice compound band2zns5. *Physical Review Materials*, 6(10), October 2022. 9

[71] Madalynn Marshall, Brianna R. Billingsley, Xiaojian Bai, Qianli Ma, Tai Kong, and Huibo Cao. Field-induced partial disorder in a shastry-sutherland lattice. *Nature Communications*, 14(1), 2023. 9

[72] Qianli Ma, Brianna R. Billingsley, Madalynn Marshall, David A. Dahlbom, Yiqing Hao, Daniel M. Pajerowski, Alexander I. Kolesnikov, Xiaojian Bai,

Cristian D. Batista, Tai Kong, and Huibo Cao. Quantum entanglement of xy-type spin dimers in shastry-sutherland lattice, 2024. 9, 84

[73] Malik Ashtar, Yuming Bai, Longmeng Xu, Zongtang Wan, Zijun Wei, Yong Liu, Mohsin Ali Marwat, and Zhaoming Tian. Structure and magnetic properties of melilite-type compounds re2be2geo7 (re = pr, nd, gd–yb) with rare-earth ions on shastry–sutherland lattice. *Inorganic Chemistry*, 60(6):3626–3634, February 2021. 9, 11

[74] C. Müller and Hk. Müller-Buschbaum. Zwei oxometallate mit melilith-struktur: Nd2sibe2o7 und ho2sibe2o7. *Journal of Alloys and Compounds*, 199(1–2):151–154, September 1993. 11

[75] G. Müller and J. Friedrich. *Crystal Growth, Bulk: Methods*, page 262–274. Elsevier, 2005. 17

[76] Marcello Lappa. *Growth of semiconductors: the floating zone technique*, page 195–344. Elsevier, 2004. 17

[77] Francisco Rey-García, Rafael Ibáñez, Luis Alberto Angurel, Florinda M. Costa, and Germán F. de la Fuente. Laser floating zone growth: Overview, singular materials, broad applications, and future perspectives. *Crystals*, 11(1):38, December 2020. 17

[78] Juan Rodríguez-Carvajal. Recent advances in magnetic structure determination by neutron powder diffraction. *Physica B: Condensed Matter*, 192(1–2):55–69, October 1993. 19

[79] G. M. Kuz'micheva, V. B. Rybakov, S. A. Kutovoi, V. L. Panyutin, A. Yu. Oleinik, and O. G. Plashkarev. Preparation, structure, and properties of new laser crystals y2sibe2o7and y2al(beb)o7. *Inorganic Materials*, 38(1):60–65, January 2002. 19

[80] H. M. Rietveld. A profile refinement method for nuclear and magnetic structures. *Journal of Applied Crystallography*, 2(2):65–71, June 1969. 19

[81] L. B. McCusker, R. B. Von Dreele, D. E. Cox, D. Louër, and P. Scardi. Rietveld refinement guidelines. *Journal of Applied Crystallography*, 32(1):36–50, February 1999. 19

[82] Alden B. Greilinger. A back-reflection laue method for determining crystal orientation. *Zeitschrift für Kristallographie - Crystalline Materials*, 91(1–6):424–432, November 1935. 19

[83] B. Ouladdiaf, J. Archer, G.J. McIntyre, A.W. Hewat, D. Brau, and S. York. Orientexpress: A new system for laue neutron diffraction. *Physica B: Condensed Matter*, 385–386:1052–1054, November 2006. 20

[84] M. Buchner, K. Höfler, B. Henne, V. Ney, and A. Ney. Tutorial: Basic principles, limits of detection, and pitfalls of highly sensitive squid magnetometry for nanomagnetism and spintronics. *Journal of Applied Physics*, 124(16), October 2018. 20

[85] Sam Mugiraneza and Alannah M. Hallas. Tutorial: a beginner's guide to interpreting magnetic susceptibility data with the curie-weiss law. *Communications Physics*, 5(1), April 2022. 20

[86] Martin Nikolo. Superconductivity: A guide to alternating current susceptibility measurements and alternating current susceptometer design. *American Journal of Physics*, 63(1):57–65, January 1995. 21

[87] Jih Shang Hwang, Kai Jan Lin, and Cheng Tien. Measurement of heat capacity by fitting the whole temperature response of a heat-pulse calorimeter. *Review of Scientific Instruments*, 68(1):94–101, January 1997. 22

[88] V. O. Garlea, B. C. Chakoumakos, S. A. Moore, G. B. Taylor, T. Chae, R. G. Maples, R. A. Riedel, G. W. Lynn, and D. L. Selby. The high-resolution powder

diffractometer at the High Flux Isotope Reactor. *Applied Physics A*, 99(3):531–535, Jun 2010. 22

[89] S. Calder, K. An, R. Boehler, C. R. Dela Cruz, M. D. Frontzek, M. Guthrie, B. Haberl, A. Huq, S. A. J. Kimber, J. Liu, J. J. Molaison, J. Neuefeind, K. Page, A. M. dos Santos, K. M. Taddei, C. Tulk, and M. G. Tucker. A suite-level review of the neutron powder diffraction instruments at Oak Ridge National Laboratory. *Review of Scientific Instruments*, 89(9):092701, 09 2018. 22

[90] A.S Wills. A new protocol for the determination of magnetic structures using simulated annealing and representational analysis (sarah). *Physica B: Condensed Matter*, 276–278:680–681, March 2000. 22

[91] Raju Baral, Danielle R. Yahne, Malcolm J. Cochran, Matthew Powell, Joseph W. Kolis, Haidong Zhou, and Stuart Calder. Magnetic pair distribution function and half polarized neutron powder diffraction at the hb-2a powder diffractometer, 2025. 23

[92] I. A. Kibalin and A. Gukasov. Local magnetic anisotropy by polarized neutron powder diffraction: Application of magnetically induced preferred crystallite orientation. *Physical Review Research*, 1(3), November 2019. 23, 82

[93] M. T. McDonnell, D. P. Olds, K. L. Page, J. C. Neufeind, M. G. Tucker, J. C. Bilheux, W. Zhou, and P. F. Peterson. Addie: Advanced diffraction environment – a software environment for analyzing neutron diffraction data. *Acta Crystallographica Section A Foundations and Advances*, 73(a1):a377–a377, May 2017. 24

[94] Maxwell W. Terban and Simon J. L. Billinge. Structural analysis of molecular materials using the pair distribution function. *Chemical Reviews*, 122(1):1208–1272, November 2021. 24

[95] T. Proffen. Analysis of disordered materials using total scattering and the atomic pair distribution function. *Reviews in Mineralogy and Geochemistry*, 63(1):255–274, January 2006. 24

[96] G E Granroth, A I Kolesnikov, T E Sherline, J P Clancy, K A Ross, J P C Ruff, B D Gaulin, and S E Nagler. Sequoia: A newly operating chopper spectrometer at the sns. *Journal of Physics: Conference Series*, 251:012058, November 2010. 24

[97] D. L. Abernathy, M. B. Stone, M. J. Loguillo, M. S. Lucas, O. Delaire, X. Tang, J. Y. Y. Lin, and B. Fultz. Design and operation of the wide angular-range chopper spectrometer arcs at the spallation neutron source. *Review of Scientific Instruments*, 83(1), January 2012. 25

[98] G. Ehlers, A. A. Podlesnyak, J. L. Niedziela, E. B. Iverson, and P. E. Sokol. The new cold neutron chopper spectrometer at the spallation neutron source: Design and performance. *Review of Scientific Instruments*, 82(8), August 2011. 25

[99] G. Ehlers, A. A. Podlesnyak, and A. I. Kolesnikov. The cold neutron chopper spectrometer at the spallation neutron source—a review of the first 8 years of operation. *Review of Scientific Instruments*, 87(9), September 2016. 25

[100] A. Brassington, Q. Ma, G. Sala, A. I. Kolesnikov, K. M. Taddei, Y. Wu, E. S. Choi, H. Wang, W. Xie, J. Ma, H. D. Zhou, and A. A. Aczel. Magnetic properties of the quasi-xy shastry-sutherland magnet $Er_2Be_2SiO_7$. *Physical Review Materials*, 8(9), September 2024. 26

[101] Qianli Ma, Xiaojian Bai, Erxi Feng, Guannan Zhang, and Huibo Cao. Crysfieldexplorer: rapid optimization of the crystal field hamiltonian. *Journal of Applied Crystallography*, 56(4):1229–1241, July 2023. 27

[102] Matt Probert. Thermodynamic properties of solids: Experiment and modeling, edited by samrath l. chaplot, ranjan mittal and narayani choudhury: Scope: review. level: postgraduate, early career researcher, researcher. *Contemporary Physics*, 53(1):62–63, January 2012. 84

[103] J. T. Haraldsen, T. Barnes, and J. L. Musfeldt. Neutron scattering and magnetic observables for spin clusters and molecular magnets. *Physical Review B*, 71(6), February 2005. 84

Vita

Alexander Brassington was born in Georgetown, Guyana. After graduating from high school in Guyana he attended Troy University in Alabama where he received his undergraduate degree in Physics and Mathematics. After graduating from Troy University he joined the doctoral physics program at the University of Tennessee, Knoxville. Here he was exposed to the world of solid state or condensed matter physics and basic techniques in crystallography. Under the direction of Dr. Haidong Zhou he conducted research into the magnetic properties of novel rare-earth crystalline compounds.